TOWARDS AN NMR OSCILLATOR

by

Anna Korver

A dissertation submitted in partial fulfillment of
the requirements for the degree of

Doctor of Philosophy
(Physics)

at the
UNIVERSITY OF WISCONSIN–MADISON
2015

Date of final oral examination: 12/11/2015

The dissertation is approved by the following members of the Final Oral Committee:

Thad G. Walker, Professor, Physics
Deniz Yavuz, Professor, Physics
James Lawler, Professor, Physics
Mark Saffman, Professor, Physics
Sean Fain, Professor, Medical Physics

ACKNOWLEDGMENTS

I would like to thank, first of all, my advisor Thad Walker, who, with his infinite patience and unquenchable enthusiasm, has guided and taught me these past years.

I would like to thank the other members of the lab, past and present, who have helped me in many ways: Bob Wyllie, Ibrahim Sulai, Zack DeLand, Matt Ebert, Dan Thrasher, Mike Larsen, Mike Bulatowicz.

I also thank my family: my parents for encouraging me past the rough patches; for my son James Athanasius for making me smile everytime I walk in the door; finally, and most importantly, my husband David, I cannot thank him enough for all the loving support he has given me.

Lastly, I would like to thank the funding sources for this project: the NSF and Northrup Grumman. I would also like to thank the physics department here at UW-Madison for generously supporting me during my maternity leave and accomodating me as a new mother.

DISCARD THIS PAGE

TABLE OF CONTENTS

Page

Appendix

Page

DISCARD THIS PAGE

LIST OF FIGURES

Appendix
Figure Page

Appendix
Figure Page

Appendix
Figure Page

Appendix
Figure Page

Appendix
Figure Page

Appendix
Figure Page

Figure Page

Figure Page

ABSTRACT

NMR as a means of precision measurement promises fundamental frequency uncertainties reaching the 10s of pico-Hz level. This level of precision opens the to door to a rich variety of applications for NMR oscillators, from fundamental physics to inertial navigation. However, longitudinal NMR with hyper-polarized noble gas and embedded ultra-sensitive atomic magnetometer detection suffers from systematic errors, such as the alkali field shift of the NMR frequency, which degrade the stability of the device. The novel method of NMR with hyper-polarized gases as presented in this thesis, suppresses the alkali field shift by over a factor of 2500 and projects photon shot noise limited NMR frequency sensitivities below $10\text{nHz}/\sqrt{\text{Hz}}$. The suppression is accomplished by first applying the NMR bias field as a sequence of alkali 2π pulses, which allows us to polarize the alkali atoms perpendicular to the bias field. The alkali polarization is then modulated at the NMR frequency, which polarizes the noble gas via spin exchange collisions. On resonance, the noble gas and alkali spins co-precess, despite a 1000 fold difference in their gyromagnetic ratios, which means that the time average torque on the noble gas due to the alkali is zero, thus eliminating the NMR frequency shift due to the alkali field. The successful implementation of static transverse optical pumping in Earth-scale bias fields and synchronous spin exchange optical pumping are presented in this thesis.

Chapter 1

Introduction

The usefulness of atomic sensors as precision measurement devices has been under development for many years. From atomic clocks [Kasevich, Riis, Chu, and Devoe, 1989] to atomic magnetometers [Allred, Lyman, Kornack, and Romalis, 2002] to atom interferometers [Kasevich and Chu 1991] the methodologies are rich and varied. The sensitivities and stabilities promised with these devices drive applications in many areas from inertial navigation to fundamental tests of physics. Although I will compare to other methods, the main focus in this thesis will be on nuclear magnetic resonance as a method for ultra-sensitive and ultra-stable measurements of both inertial rotations and fundamental physics. The new NMR approach developed here should greatly suppress systematic errors that plague other implementations of NMR oscillators and our first results promise for sensitivity levels that are on par with more developed methods with plenty of room for improvement.

1.1 The NMR Oscillator: Benefits and Drawbacks

The basic principle of the NMR oscillator is a precision measurement of the resonance frequency associated with the nuclei of a particular noble gas species. In terms of measurements, this frequency has two important contributions. The first is from the bias field B_0 and the second, X, is the rotation or anomalous spin coupling to be measured:

$$f = \gamma_K B_0 + X \tag{1.1}$$

where γ_K is the gyromagnetic ratio of the noble gas.

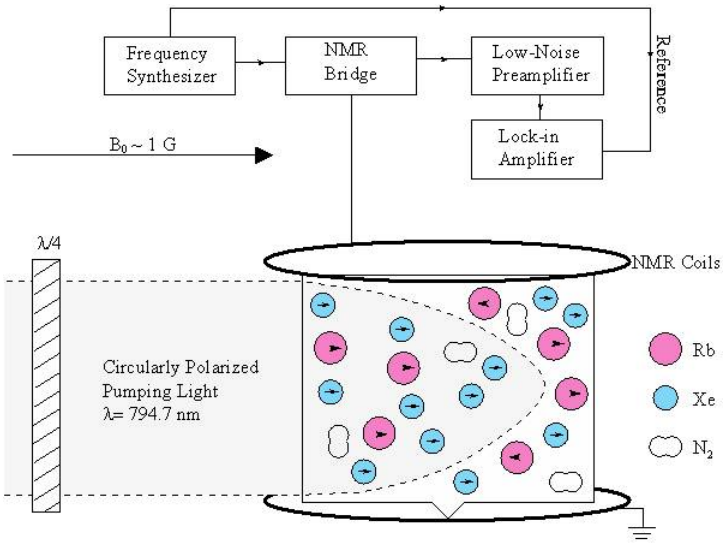

Figure 1.1: The basic setup for longitudinal NMR has the pump light aligned along the same axis as the bias field, thus polarizing the alkali through direct optical pumping and the noble gas by spin exchange optical pumping. The transverse polarization of the noble gas is then excited by resonant modulation along the transverse direction. The nuclear polarization is detected by either the NMR drive coils or by the embedded magnetometer. Figure from Ref [Walker and Happer, 1997]

The basic setup for longitudinally pumped NMR is shown in Fig. 1.1. In order to observe the noble gas precession, angular momentum must be transferred to the nuclei. This is done by optically pumping alkali atoms with circularly polarized pump light parallel to $\bar{B}_0$; then through spin-exchange collisions, the alkali atoms transfer angular momentum to the nuclei of the noble gas. Once the noble gas is polarized along $\bar{B}_0$, it is resonantly driven by a transverse AC magnetic field, which creates a maximum transverse noble gas polarization when $f = \gamma B_0$. The nuclei then precess about $\bar{B}_0$ at their characteristic frequency. This precession can subsequently be detected by one of two methods. The first is to use the driving coils to pick up the oscillating field produced by the noble gas. The second is to use the ultra-sensitive embedded alkali magnetometer, which benefits from the Fermi contact interaction that enhances the noble gas field by up to a factor of 1000.

For many applications the frequency shifts X are very small. For example, a gyroscope that is to be used for commercial airline navigation needs a bias stability of $0.01°$/hr [Groves, 2008], [Budker and Kimball, 2013] which for ^{131}Xe is a field stability of about 5fT. The best magnetometers that are able to operate in large bias fields have a stability of around $10\mathrm{fT}/\sqrt{\mathrm{Hz}}$. To mitigate the stringent requirements on field stability, two isotopes can be used. In this case we have:

$$f_1 = \gamma_1 B_0 + X_1 \tag{1.2}$$

$$f_2 = \gamma_2 B_0 + X_2 \tag{1.3}$$

The magnetic field dependence of the two isotopes differ due to their gyromagnetic ratios, so the field can be stabilized by locking one isotope to a submultiple of a clock. When this is done, the second isotope resonance frequency is independent of magnetic field:

$$f_2 = \frac{\gamma_2}{\gamma_1} f_C + X_2 - \frac{\gamma_2}{\gamma_1} X_1 \tag{1.4}$$

With techniques such as these NMR oscillators are able to reach the required sensitivity levels. With this technique, which will be explained in more detail in this thesis, and with other techniques NMR gyroscopes have shown bias stabilities of near $0.02°$/hr and angle random walk numbers of $2 \times 10^{-3\circ}/\sqrt{\mathrm{hr}}$ [Kornack, Ghosh, and Romalis, 2005].

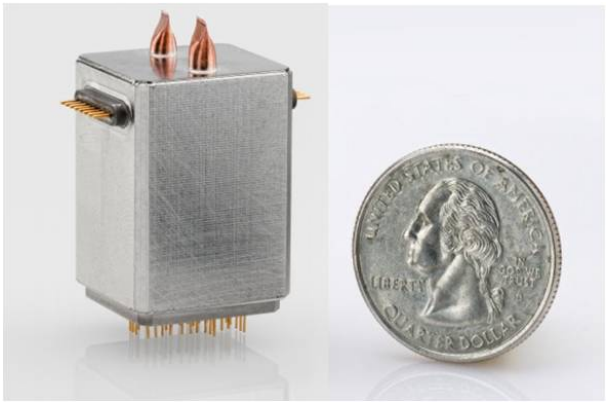

Figure 1.2: The size of the gyro under development at Northrop Grumman. The scalability of NMR gyros is one of the many benefits of this technology.

Other gyroscope technologies that are being developed such as atom interferometers are capable of an angle random walk of $3 \times 10^{-6\circ}/\sqrt{\mathrm{hr}}$ with a bias instability of $7 \times 10^{-5}\ ^\circ/\mathrm{hr}$ [Durfee, Shaham, and Kasevich, 2006], [Kitching, Knappe, and Donley, 2011]. Much more common are ring laser gyroscopes, which have an angle random walk in commercial units that is equivalent to NMR gyroscopes of around $3 \times 10^{-3\circ}/\sqrt{\mathrm{hr}}$ and a bias instability that is $5 \times 10^{-4}\ ^\circ/\mathrm{hr}$ [Chow, Gea-Banachioche, Pedrottie, Schleich, and Scully, 1984]. So why do we bother with a new technology when something well developed already exists and, in the case of atom interferometers, is much better? The problem with both of these devices is that their sensitivity scales with size; the larger they are, the better they are. For example, the atom interferometer numbers quoted above are for a 2m device; while the ring laser gyro is smaller, it is still at 4.5×8.8cm. The NMR gyroscope benefits from being scalable to smaller sizes and much progress has been made in the way of miniturizing and microfabricating magnetometers and NMR gyroscopes [Jimenes-Martinez et al., 2014], [Mhaskar, Knappe, and Kitching, 2012]. Figure 1.2 shows a gyroscope developed at Northrop Grumman that demonstrates the attainable compact size. Also, there are many potential advances in NMR gyroscopes that will close the gap in sensitivity. Our approach aims to accomplish this.

Along with the benefits of NMR come some drawbacks. Equation 1.1 is oversimplified; there are two other contributions to f that introduce systematic errors and degrade bias stability:

$$f = \gamma_K(B_0 + B_A) + Q + X \tag{1.5}$$

The two parameters introduced are the quadrupole interaction Q and the alkali field B_A. The shift from the quadrupole interaction arises from the large electric field gradients interacting with $I > 1/2$ nuclei at the cell walls [Cohen-Tannoudji, 1963], [Kwon, Mark, and Volk, 1981]. In longitudinally pumped NMR described above, the alkali is polarized along the bias field direction and the magnetic field generated by the alkali is sensed by the noble gas, and therefore contributes to the NMR frequency. Because the alkali field is dependent on the alkali density and polarization, any fluctuation in these two parameters will degrade the sensitivity of the oscillator. There is a tradeoff between the quadrupole and the alkali shifts. The quadrupole shift can be eliminated by using spin-1/2 nuclei such as ^{129}Xe and ^{3}He, but then there is a large differential alkali field that cannot be taken away by dual species operation as described above.

Methods have been developed that deal with these two systematic errors. In Ref [Bulatowicz et al., 2013], two Xe isotopes are used to essentially cancel out the effect of the alkali frequency shift. Assuming that there is no isotopic difference in the alkali field seen by the noble gas, the frequency shift will be proportional to the respective Xe gyromagnetic ratio and cancel in the deduced frequency ratio. However, as this experiment discovered, there is a differential frequency shift, which adds a term proportional to B_A to the frequency ratio:

$$f_2 = \frac{\gamma_2}{\gamma_1} f_1 - \frac{\gamma_2}{\gamma_1} X_1 + X_2 + \gamma_2(B_{A2} - B_{A1}) \tag{1.6}$$

The third term is the physics factor of interest. The differential shift set a limit of $\delta B_A/B_A = 0.2\%$ on how well this experiment could eliminate the effect of the alkali field shift. This experiment will be discussed in more detail below.

Another method is presented in Ref [Kornack et al., 2005]. It uses spin-1/2 nuclei ^{3}He to eliminate Q. The magnetometer is then configured so that the alkali atoms operate in zero field by cancelling the magnetic field produced by the noble gas with an applied bias field. The noble gas then adiabatically follows and cancels drifts in the external magnetic field.

The method outlined in this thesis plans to eventually use only spin-1/2 nuclei and eliminates the effect of the alkali field by polarizing the alkali atoms perpendicular to the bias field and parallel to the noble gas.

1.2 Applications: Tests for Fundamental Physics

We have talked a little about using NMR for gyroscopy. Another application is in the search for exotic physics. Of particular interest for this thesis is the experiment done by Ref [Bulatowicz et al., 2013] in which a search for axions was carried out. The axion is a dark matter candidate that would have a scalar-pseudoscalar coupling to the polarized nucleus of a noble gas. This coupling causes a shift in the NMR frequency corresponding to the product $g_s g_p^n$ for which this experiment improved the upper bound by two orders of magnitude at sub-mm length scales.

The experiment is done by using ^{129}Xe to measure, as a function of time, the magnetic field fluctuations due to alkali polarization drifts and real magnetic field noise. The ^{131}Xe is then used to isolate any frequency shifts that would arise from an exotic spin coupling. The difference in the ratio of the noble gas frequencies with the rod close to and far from the cell is used to measure the relevant frequency shift. An anomalous spin coupling would show up as a field dependent change in the ratio of gyromagnetic ratios, which is a well known constant [Brinkmann, 1963]. The following description of this experiment illustrates how the quadrupole interaction and the alkali field shift affect a precision measurement using NMR.

The quadrupole shift in ^{131}Xe is accounted for by fitting the free induction decay signals to the averaged quadrupole interaction arising from the individual faces of the cell. As can be seen in Fig 1.3 the quadrupole interaction makes for a very complicated waveform that, even so, is well accounted for with the fitting function. To the extent that the field experienced by the noble gas is the same for the two isotopes, the alkali frequency shift is cancelled in the ratio of the frequencies being measured. However, as mentioned above, there is an isotope dependence.

As can be seen in Fig 1.4, there is a slight change in the ratio of gyromagnetic ratios that is correlated to the product of alkali polarization direction and magnetic field direction. This effect can be accounted for by a 0.2% difference in the alkali field sensed by the two isotopes. An actual

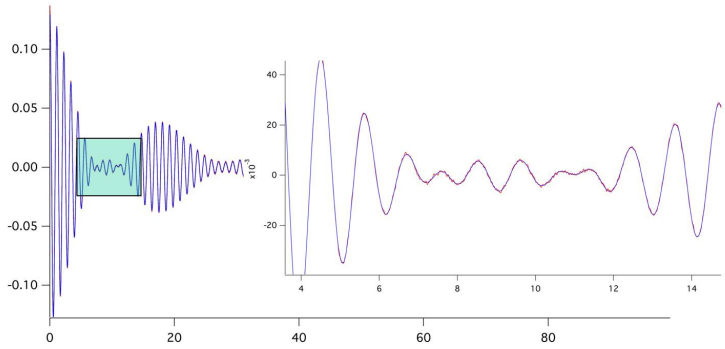

Figure 1.3: In the axion experiment, the ^{131}Xe free induction decay signal is complicated by the quadrupole interaction. This figure shows a fit to this interaction and the data; as can be seen, the quadrupole is well described.

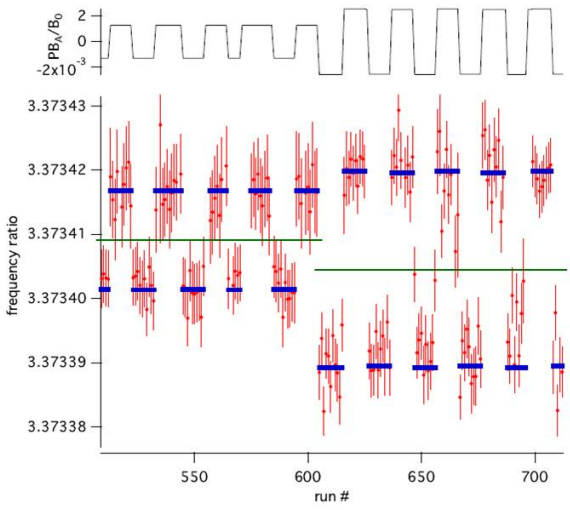

Figure 1.4: This figure shows a sample of the data for the axion experiment. There is a correlation between the ratio of gyromagnetic ratios and the product of the polarization and magnetic field. This is consistent with a differential alkali field shift of $\delta B_A/B_A = 0.2\%$.

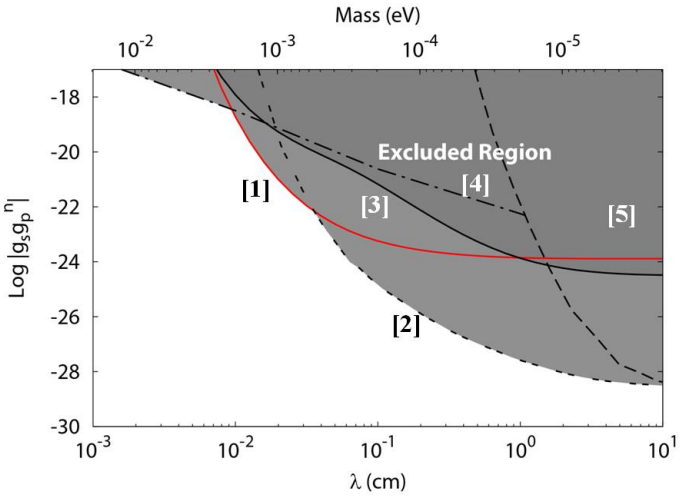

Figure 1.5: The results of the axion experiment are shown in red. The results in 2: [Tullney et al., 2013] were published at nearly the same time. The methodology outlined in this thesis hopes to improve on the red curve by three orders of magnitude. The other limits were set by 3:[Chu et al., 2013], 4: [Petukhov, Pignol, Jullien, and Andersen, 2010], and 5: [Youdin, Krause, Jagannathan, Hunter, and Lamoreaux, 1996]

axion signal, as Eqn 1.6 describes, would exhibit a change in the ratio of gyromagnetic ratios that only depends on magnetic field, not polarization. The new bound on the scalar-pseudoscalar coupling is shown in Fig 1.5. The goal of the method described in this thesis is to improve on the upper limit of the axion interaction by three orders of magnitude by completely eliminating the effects of both the quadrupole and alkali field frequency shifts.

Other searches for fundamental physics include the comagnetometer search for Lorentz invariance in Refs [Smiciklas, Brown, Cheuk, Smullin, and Romalis, 2011], [Allmendinger et al., 2014], searches for permanent electric dipole moment Refs [Vold, Raab, Heckel, and Fortson, 1984],[Rosenberry and Chupp, 2001], and anomalous spin couplings Ref [Glenday, Cramer, Phillips, and Walsworth, 2008]

1.3 This Work

This thesis describes the work done towards implementing a novel form of NMR that promises to eliminate the systematic errors that plague the conventional methods. The NMR frequency shift

experienced from the alkali field is suppressed by optically pumping the alkali atoms perpendicular to the bias field and parallel to the Xe. The way we do this is by applying the bias field, not as a DC field, but as a sequence of alkali 2π pulses that are transverse to the optical pumping direction and whose repetition rate sets the size of the bias field: $f_{\mathrm{pulse}} = \gamma_{\mathrm{Rb}} B_{\mathrm{bias}}$ where the gyromagnetic ratio is $\gamma_{\mathrm{Rb}} = \frac{2\mu_B}{2I+1}$, μ_B is the Bohr magneton, and I is the alkali nuclear spin. Since a 2π pulse is the same as a 0π pulse, the alkali can be polarized up to 100% perpendicular to the large effective bias field without significant magnetometer response loss. By subsequently flipping the alkali spin polarization at the NMR frequency, $f_{\mathrm{Xe}} = \gamma_{\mathrm{Xe}} B_{\mathrm{bias}}$ where B_{bias} is defined by the pulse repetition rate, the Xe is spin exchange optically pumped synchronously with the Rb. The two species then co-precess even though their magnetic moments differ by a factor of 1000. This means that the time average torque on the noble gas due to the Rb is zero, and the NMR frequency shift from the alkali is eliminated.

Two publications have resulted from this work: [Korver, Wyllie, Lancor, and Walker, 2013] and [Korver, Wyllie, Lancor, and Walker, 2015]. The first introduces the transverse optical pumping procedure and studies the additional relaxation mechanism that results from the application of the 2π pulses. This paper, as discussed in Chapter 2 of this thesis, shows that despite the additional relaxation, the magnetometer is only a factor of three less sensitive than a SERF magnetometer, and it is a factor of 30 better than the light narrowed magnetometer described in [Smullin, Savukov, Vasilakis, Ghosh, and Romalis, 2009] that operates in equivalently high magnetic fields. The second paper, Chapter 3 of this thesis, utilizes the transverse optical pumping results to implement synchronous spin exchange optical pumping of ^{131}Xe and ^{129}Xe. It points out that though the alkali field does not shift the NMR frequency, it broadens the linewidth. This effect can be compensated by applying a magnetic field 180° out of phase with the alkali polarization modulation, thus narrowing the line to the T_1 limit.

In addition to the methodology that enables us to execute synchronous spin exchange optical pumping, I also include the first results for dual species operation, a summary of noise measurements and figure of merit projections, magnetometer and NMR characterization measurements, and a detailed description of the apparatus and the procedures undertaken to optimize it.

The thesis will progress as follows. In chapter 2 I will talk about the method we use to apply the bias field that allows us to obtain up to 100% transverse polarization. In chapter 3 I will proceed with a discussion about how we synchronously pump the noble gas nuclei, so that the time averaged alkali and the noble gas spins are parallel. Chapter 4 will go into more detail about the characteristics of the NMR when using the synchronous spin exchange optical pumping technique; it will cover the essential measurements we took to characterize the cell as well as the measurement of a density dependent wall relaxation mechanism in ^{131}Xe. The next chapter will cover details concerning the figures of merit for the NMR oscillator with dual species implementation and the accompanying noise measurements. Also included are techniques we tried to reduce the noise in the system. Chapters 6 and 7 will explain more about the technical details of the apparatus itself including the circuitry, optics, detection schemes, and magnetometer characteristic measurements. Chapter 8 will cover preliminary experiments on dual noble gas species operation. The final chapter summarizes the accomplishments of the past several years and speaks to future work.

Chapter 2

Transverse Optical Pumping with Pulsed Parametric Modulation

Zero field atomic magnetometers are a well developed technology, but operation in high magnetic fields without significant loss of atomic spin polarization and response is an outstanding problem. The technique developed here is a new method for operating atomic magnetometers in Earth scale magnetic fields. It employs an extension of the spin dressing technique first done by Haroche and Cohen-Tannoudji [Haroche and Cohen-Tannoudji 1970] in the 70s. Instead of their sinusoidal field dressing, we use a sequence of short pulses that each produce an alkali 2π rotation. With this method, we are able to operate in fields on the order of 0.1G without significant loss in spin polarization or magnetometer gain. This chapter will describe the successful implementation of the method as well its limitations. Compared to a zero field SERF magnetometer, our Pulsed Parametric Resonance (PPR) magnetometer loses only a factor of 3 in gain when operating at high fields. Also, in comparison to a standard high field magnetometer, the PPR is a factor of 30 more sensitive. The success of this magnetometer as published in [Korver et al., 2013] opens the door to polarizing the alkali atoms up to 100% transverse to a large magnetic field that, in subsequent experiments, is the bias field for NMR; these experiments are discussed in Chapter 3 of this thesis.

Before introducing the details of the PPR magnetometer, I will describe zero field magnetometer operation since it is vital for an understanding of all else that follows. I will then detail the PPR magnetometer and how it supresses the rate of angular momentum loss due to spin-exchange collisions that enables us to operate in high fields. The success of this method is then shown by a comparison to a zero field SERF magnetometer and a light narrowed, high field magnetometer.

2.1 Optical Pumping and Magnetometry

The simple picture of an atomic magnetometer can be seen in Fig. 2.1. Circularly polarized optical pumping light aligns the atomic spins along the pump light axis. A simplified illustration is shown in Fig 2.2. Because of angular momentum selection rules, we can exclusively excite the atoms in one sublevel of the ground state, leaving the other level unaffected. Once in the excited state, the atoms undergo collisions with the buffer gas that randomize the electron spin and eventually de-excite the atoms equally into both ground states; therefore, in steady state, all the atoms will be pumped into the dark state, aligned along the pumping direction. A magnetic field that is perpendicular to the alignment of the atoms will cause the spins to tilt into the probe direction. This tilt is detected by Faraday rotation of the probe polarization with an angle that corresponds to the magnitude of the magnetic field.

What is not included in the simplified version outlined above is the interaction with the alkali nuclear spin. The behavior of an atomic magnetometer is generally complicated by nuclear spin effects, but is simplified in the regime where the spin exchange collision rate $\Gamma_{\mathrm{SE}} = n\sigma_{\mathrm{SE}}\bar{v}$ is much higher than any other rate. In particular, it must be much higher than the Larmor precession rate associated with a magnetic field B, $\Gamma_{\mathrm{SE}} >> g_s\mu_B B/(2I+1)$ where σ_{SE} is the spin exchange cross section; g_s is the electron g-factor; μ_B is the Bohr magneton, and I is the nuclear spin. At any given polarization in this regime, the electron angular momentum is distributed amongst the hyperfine sublevels of the ground state. It is important to note that the two total angular momentum levels F of the ground state have equal and opposite magnetic moments, where $F = I+S = I\pm 1/2$ and I is the nuclear spin of the alkali isotope: $3/2$ for ^{87}Rb and $5/2$ for ^{85}Rb. When the alkali atoms undergo spin-exchange collisions, the population of the energy levels is redistributed amongst the sublevels, so there is a probability that any particular atom will switch hyperfine levels, thus changing the sign of its magnetic moment. In the presence of a magnetic field, the electron is precessing at the Larmor rate between collisions, so when it undergoes an F level changing collision, it will subsequently precess in the opposite direction. Therefore, although total angular momentum is preserved in a spin exchange collision, the electron spin orientation is not. Thus spin exchange collisions, when

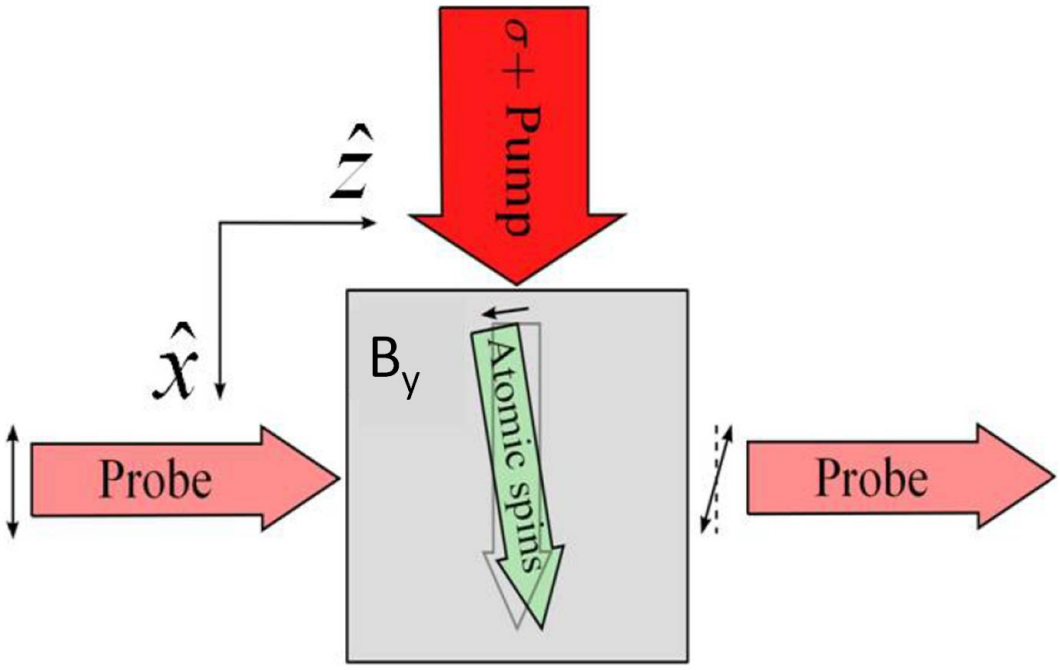

Figure 2.1: In this simplified simplified magnetometer setup the pump is directed along $\hat{x}$ and the probe along $\hat{y}$, so that the atoms are sensitive to B_z. The rotation is detected by Faraday rotation of the probe.

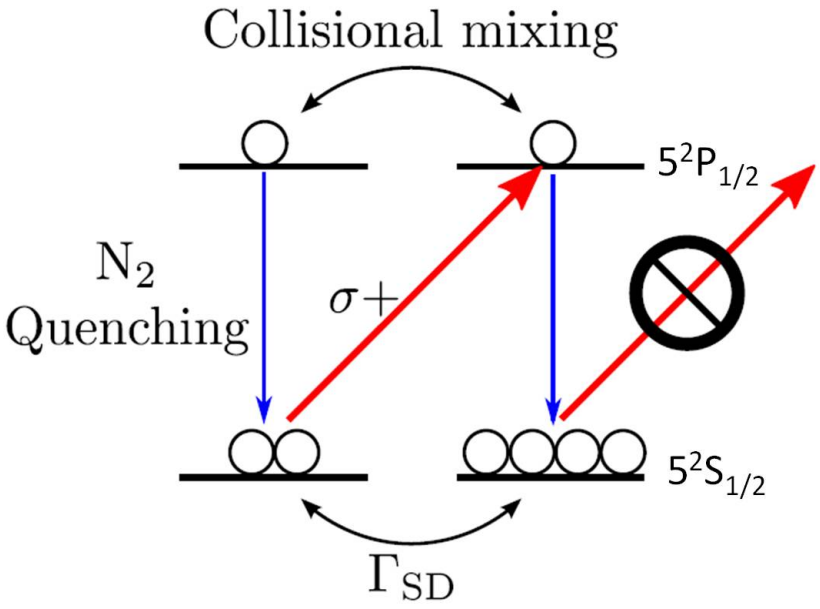

Figure 2.2: This is a simplified picture of D1 line optical pumping where σ^+ pump light excites only the atoms in $m = -1/2$ thus pumping the atoms into the $m = 1/2$ dark state. The figure is adapted from [Walker and Happer, 1997]

they happen at a rate much slower than the Larmor rate, cause the precession to quickly decohere. However, if the spin exchange rate is much faster than the Larmor precession, the electron does not rotate very far before undergoing another spin exchange collision. In this regime where the sign of the magnetic moment is changing rapidly with respect to the Larmor precession rate, the magnetic moment averages to a smaller value and the spin precesses at a slowed rate. This is called the the spin-temperature regime where the density matrix is well described by the statistical distribution $\rho \propto e^{-\beta m_F}$ [Happer and Tam, 1977] [Happer, 1972] [Anderson, Pipkin, and Baird, 1960] where β is the spin temperature parameter:

$$\beta = 2 \arctan(P) \tag{2.1}$$

where P is the electron polarization. This formalism is used to relate the average angular momentum of the electron to the average total angular momentum of the atoms via the slowing down factor:

$$\frac{\langle F_z \rangle}{\langle S_z \rangle} = q = 1 + (2I+1) * \coth\left[\frac{\beta}{2}\right] * \coth\left[\beta(I+\frac{1}{2})\right] - \coth\left[\frac{\beta}{2}\right] \tag{2.2}$$

The slowing down factor q is vital for a full understanding of the relaxation processes we observe in transverse optical pumping; its value varies smoothly from zero polarization to 100% polarization as shown in Fig. 2.3. It's effects will be described in more detail in this chapter.

For the purposes of the discussion about relaxation in transverse optical pumping, it is helpful to know what a spin temperature distribution looks like and how it relates to alkali polarization. Figure 2.4 illustrates the population distribution amongst the m_F levels that corresponds to different initial Rb polarizations. Fig. 2.5 illustrates the redistribution of the sublevels as a result of a particular spin-exchange collision. It is important to note that as the polarization increases, the electron occupies higher $|F, m\rangle$ states until, at 100% polarization, the electron is in the state $|F, m\rangle = |2, 2\rangle$. In this state, a spin exchange collision results in very little population redistribution. This is the light-narrowed regime, where the increased polarization suppresses the decoherence due to spin-exchange relaxation; later in this chapter I will compare the results of the PPR magnetometer to a purely light narrowed magnetometer.

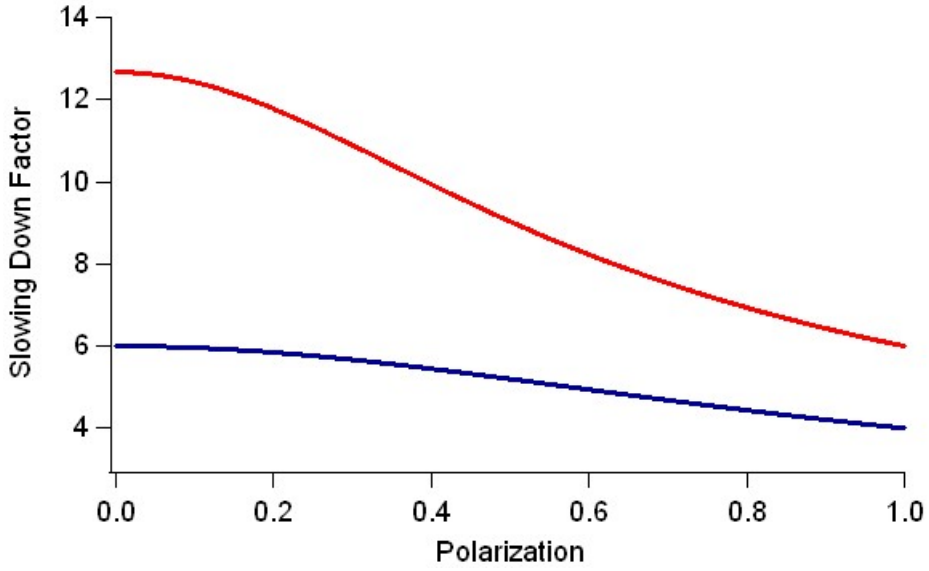

Figure 2.3: The slowing down factor polarization dependence for ^{87}Rb in blue and ^{85}Rb in red. The slowing down factor describes the fraction of the total angular momentum stored in the electron: $\mathbf{F} = \mathbf{qS}$. For the measurements and calculations done for the 2π pulse spin exchange relaxation model, it is vital that the slowing down factor is properly taken into account.

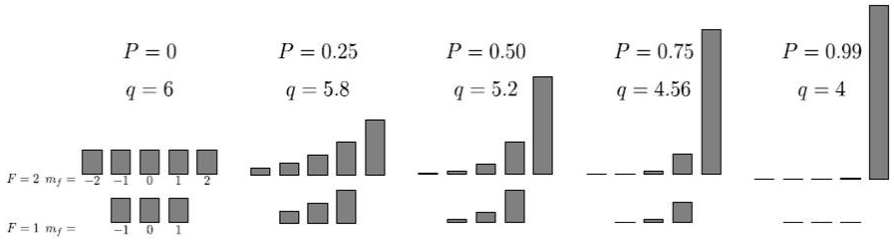

Figure 2.4: The figure illustrates the spin temperature distrbution that corresponds to various initial Rb polarizations. Important for our discussion is the fact that as the polarization gets higher, the population in the $|2, 2\rangle$ state increases.

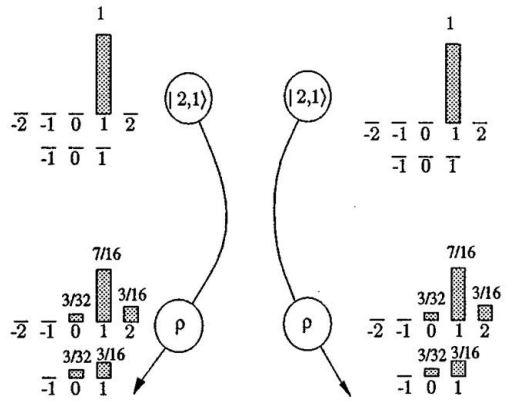

Figure 2.5: The figure, taken from [Walker and Happer, 1997], shows the m level distribution associated with a spin exchange collision. Total angular momentum is preserved, while the m level populations are redistributed. Atoms in different F levels precess in opposite directions.

When operating in the spin-temperature regime, the time evolution of the spins is well described by the Bloch equations [Allred et al., 2002], [Ledbetter, Savukov, Aosta, Budker, and Romalis, 2008]:

$$q(P)\frac{\mathrm{dP}}{\mathrm{dt}} = \boldsymbol{P} \times \boldsymbol{\Omega} + \mathrm{R}\hat{s} - \Gamma'\boldsymbol{P} \tag{2.3}$$

where $\bar{P} = 2\langle\bar{S}\rangle$ is the electron polarization, S is the electron spin, R is the pumping rate, $\hat{s}$ is optical pumping vector, Γ' is the relaxation rate, and Ω is the Larmor angular rotation rate defined as $2\pi\gamma\bar{B}$. Solving the system of equations for the steady state solution, we obtain

$$\mathbf{P} = \frac{\boldsymbol{R}\Gamma' + \boldsymbol{R} \times \boldsymbol{\Omega} + \boldsymbol{\Omega}(\boldsymbol{\Omega} \cdot \boldsymbol{R})/\Gamma'}{\Gamma'^2 + \boldsymbol{\Omega}^2} \tag{2.4}$$

Depending on probe direction, the magnetometer is sensitive to a magnetic field perpendicular to the optical pumping direction. For example, if the probe is directed along $\hat{y}$, then there is $\hat{z}$ field sensitivity:

$$P_y = \frac{R\Omega_z + \Omega_x\Omega_y R/\Gamma'}{\Gamma'^2 + \Omega^2} \tag{2.5}$$

For a well nulled magnetometer this reduces to:

$$P_y = \frac{R\Omega_z}{\Gamma'^2 + \Omega_z^2} \tag{2.6}$$

which is dispersive in form. The magnetometer gain or response is defined by the slope of the above equation at $\Omega_z = 0$, and is affected by the width of the response curve as defined by $\Gamma' = R + \Gamma_0$. A narrower linewidth typically means a larger response; additional relaxation broadens the linewidth thus degrading the magnetometer performance.

SERF magnetometry is only valid in small magnetic fields where the condition $\Gamma_{\mathrm{SE}} >> g_s\mu_B B/(2I+1)$ holds true, and since the spin-exchange relaxation rate increases quadratically with field [Happer and Tam, 1977],[Allred et al., 2002]:

$$\Gamma_2^{\mathrm{SE}} = \Omega^2 T_{\mathrm{SE}}\Big(\frac{1}{2} - \frac{(2I+1)^2}{2q^2}\Big) \tag{2.7}$$

the maximum measured fields for SERF magnetometry are on the order of 10nT. When the field is much greater than this, means must be taken to restore the response.

One such method for high field operation is parametric modulation where an oscillating field is applied perpendicular [Haroche and Cohen-Tannoudji 1970] [Smullin et al., 2009] to the bias field such that

$$f_{\mathrm{PM}} = \gamma_{Rb} B_{bias} \tag{2.8}$$

In this way the magnetometer sensitivity in higher fields is restored, but not fully. The linewidth of the transverse spin component is also broadened due to the contribution of the spin-exchange collisions to the transverse relaxation rate:

$$\Gamma_2 = \frac{R}{4} + \frac{\Gamma_{\mathrm{SE}}}{5}(1 - P) \tag{2.9}$$

for the light narrowed magnetometer of [Smullin et al., 2009] where $\Gamma_{\mathrm{SE}}$is the spin exchange rate, R is the optical pumping rate, and P is the longitudinal alkali polarization.

The sinusoidally modulated parametric fields can achieve a maximum transverse spin polarization of only 30% due to the Bessel function associated with the rotating components. However, there is nothing that limits us to a sinusoidally modulating field. It turns out, as will be described in detail below, that the optimal parametric modulation field shape is a sequence of alkali 2π pulses. In the limit of delta function pulses, transverse spin polarization reaches 100% and the magnetometer response is restored to the zero field response.

2.2 Pulsed Parametric Resonance (PPR) Essentials

The operation and derivation of the transverse pulsed parametric modulation (PPR) magnetometer is similar to sinusoidal parametric modulation. The essential components of operation are shown in Fig. 2.6 and further details are described in Chapter 6. The pump is directed along $\hat{x}$, the probe along $\hat{y}$, and the bias field $B_0 + B_1(t)$ is along $\hat{z}$. In the original experiment as described in [Korver et al., 2013], we applied a large DC magnetic field $B_0 = \Omega_0/(2\pi\gamma)\hat{z}$ and super-imposed an AC coupled 2π pulsing field $B_1(t) = \Omega_1(t)/(2\pi\gamma)\hat{z}$ at repetition rate $f_1 = \Omega_0/2\pi$. Because $B_1(t)$ is AC coupled the time average magnetic field is zero; between the pulses the magnetometer

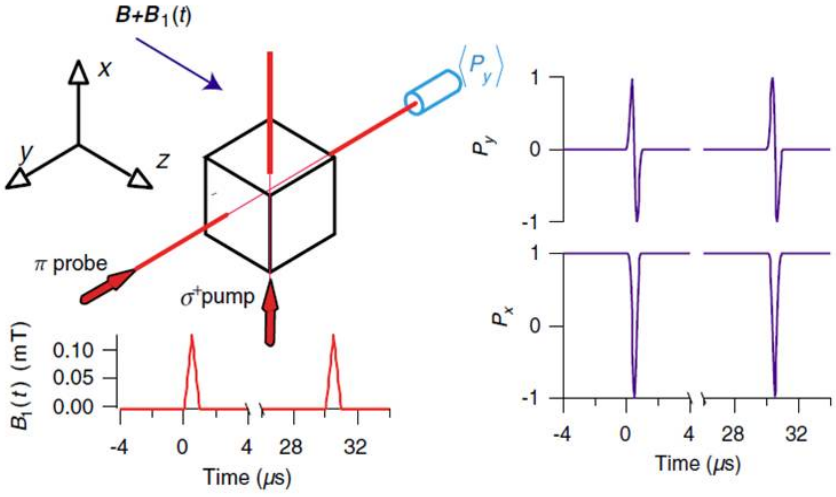

Figure 2.6: The essential optical components for the pulsed parametric modulation magnetometer consist of the pump directed along $\hat{x}$ and the probe along $\hat{y}$. The DC field and the pulsed field are applied along $\hat{z}$. The insets show models of the applied $B_1(t)$ and the resulting atomic precession as would be seen on P_y and P_x.

is in the SERF regime because $B_1 = -|B_0|$, cancelling the applied DC magnetic field. In later chapters, the AC coupling is removed for simplicity's sake and for NMR, we came to realize that the same purpose is accomplished with and without it. For this experiment, however, we simulate operation in a large magnetic field that is not purposefully applied, such as Earth's magnetic fields.

The Bloch equation formalism governing the spin polarization **P** transverse to the bias field is given by:

$$\frac{dP_+}{dt} = i[\Omega_z + \Omega_1(t)]P_+ - \Gamma_2 P_+ + R \tag{2.10}$$

where $P_+ = P_x + iP_y$. Setting $P_+ = A_+ e^{i\phi_1}$ where $\phi_1 = \int \Omega_1 dt$ we get

$$\frac{dA_+}{dt} = i\Omega_z A_+ - \Gamma_2 A_+ + Re^{-i\phi} \tag{2.11}$$

Fourier expanding with $A_+ = \sum_p A_{+p} e^{ip\omega_1 t}$ and $e^{i\phi_1} = \sum_p j_p e^{ip\omega_1 t}$ we arrive at:

$$\frac{dA_{+p}}{dt} = A_{+p}[i(\Omega_z - p\omega_1) - \Gamma_2] + Rj_p \tag{2.12}$$

The resonantly enhanced Fourier component is $p = 1$ and the steady state solution becomes

$$P_+ \approx \frac{Rj_1}{\Gamma_2 - i(\Omega_z - \omega_1)} e^{i\omega_1 t} \tag{2.13}$$

The time average then gives the DC spin polarization:

$$P_+ = \frac{R|j_1|^2}{\Gamma_2 - i(\Omega_z - \omega_1)} \tag{2.14}$$

If $\Omega_1(t)$ is sinusoidal, as in Ref. [Smullin et al., 2009], then $j_p = J_p(|\Omega_1|/\omega_1)$ are Bessel functions that give the maximum attainable transverse polarization $P_+ = J_1^2(1.84) \approx 0.34$. However, there is no reason we must restrict ourselves to sinusoidal modulation. It turns out that the function that gives the highest polarization, the largest value of j, is a sequence of δ functions.

Given the parametric field as a Dirac delta function comb:

$$B_1 = b_1[-1 + \mathrm{comb}(f_1 t)] \tag{2.15}$$

where we have defined it in such a way that the integral of Eqn. 2.15 over one period is 0, meaning B_1 is AC coupled. We can then define as we have previously $\phi_1 = \gamma \int B_1(t)dt$ so the Fourier coefficient is given by:

$$e^{i\phi_1} = \sum_p j_p e^{ip2\pi f_1 t} \rightarrow j_p = f_1 \int_{-1/2f_1}^{1/2f_1} e^{i\phi_1} e^{-ip2\pi f_1 t} dt \tag{2.16}$$

Integrating the above equation and reducing gives the Fourier coefficient for a δ function as:

$$j_{-1} = -\mathrm{sinc}\Big[\pi\Big(1 - \frac{\gamma b_1}{f_1}\Big)\Big] \tag{2.17}$$

which maximizes at 1, thus theoretically giving a transverse polarization of 1 when optimized at $\gamma b_1 = f_1$, i.e. the pulse repetition rate is the Larmor frequency corresponding to the bias field. As will be shown below, when the pulses are not δ functions, their finite duration allows relaxation which reduces the polarization.

2.3 2π Pulse Area

We discuss the 2π pulse optimization in chapter 7, so we will here only point out the important features for the current experiments. The first feature of interest in Fig. 2.7a is the shape and timing of the pulse width. The actual width of the pulse is longer than the "nominal" pulse width applied to the pulsing circuit for reasons explained in Sec. 7.1. For the purposes of the experiments below, it is the actual width of the pulse that matters; this is measured from the beginning of the pulse trigger to the point where the pulse tail reaches zero. Although not well defined, this crossing can be determined with error bars of $< 10\%$ of the full pulse width for the shortest pulses. The second important feature shown in Fig 2.7b shows no atom rotation between the pulses, demonstrating the all-important point that the field between the 2π pulses is zero.

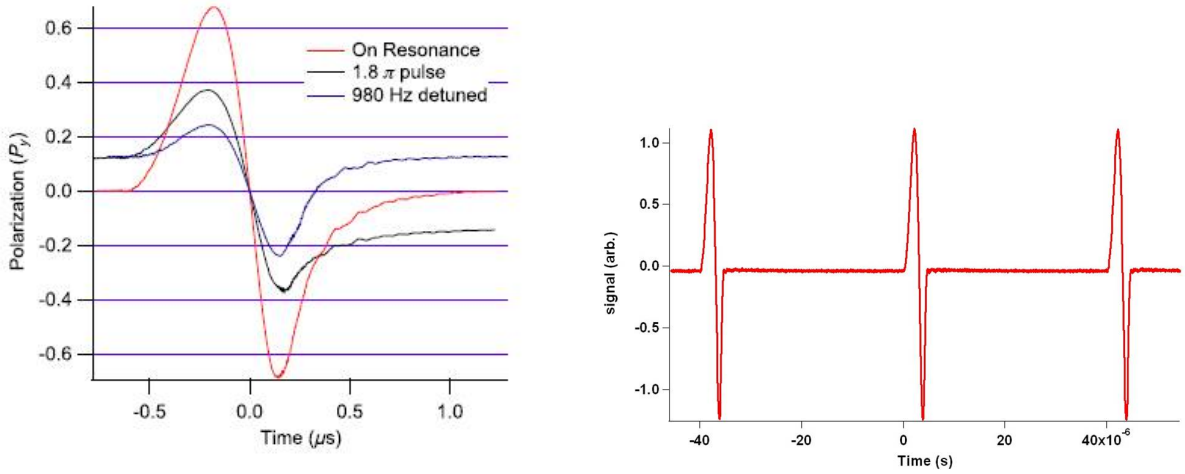

(a) 2π pulse signal

(b) 2π pulse train

Figure 2.7: The figure on the left shows the 2π pulse signal for which it is important to note that although the applied pulse width was 1μs, the resulting pulse width due to circuit constraints is $\approx 1.5\mu$s. The pulse width used in the calculations and data analysis below use the actual width as measured from the start of the trigger to the zero crossing with about 10% error. The figure on the right is an oscilloscope screen shot of the train of 2π pulses. The fact that there is no signal between the pulses, demonstrates that there is no residual field between the pulses, an all-important fact for the operating principles of the PPR magnetometer

2.4 Spin Exchange Relaxation

We have assumed that the response of the magnetometer is not degraded significantly beyond the response of a SERF magnetometer even though it is operating in high magnetic fields. This assumption rests on the fact that the magnetic field is zero for the majority of the time and therefore in the SERF regime where spin exchange collisions do not contribute to relaxation. Our assumption upon starting this project was that the 2π pulses would be so short that we could neglect any relaxation that would happen when the field is pulsed. Due to longer pulses than originally hoped, the 2π pulse widths are on par with T_{SE}; therefore, on average, there is one collision per pulse. This is experimentally demonstrated by the increase in the effective relaxation rate of the magnetometer when pulsing is turned on.

The measurements we take compare the $\hat{x}$ polarization at zero field to the $\hat{x}$ polarization with the pulsing on. We have a good handle on how to calibrate the Rb polarization measurement from using the 2π pulse signal (Fig. 2.7a). Since the 2π pulse quickly rotates the atoms from $\hat{x}$ into $\hat{y}$, the amplitude of the signal measures P_x. The amplitude can be calibrated to polarization units by measuring it as a function of pump intensity which is proportional to pumping rate. A polarization normalization factor $V_{0,\mathrm{amp}}$ is then extracted:

$$P = \frac{R}{R+\Gamma_0} \rightarrow V_{\mathrm{amp}} = \frac{V_{0,\mathrm{amp}} R}{R+\Gamma_0} \tag{2.18}$$

This measurement needs to be done at low pulsing repetition rates (50Hz) to minimize the duty cycle dependence of the spin exchange relaxation. We then have two equations for the polarization we measure. For the SERF:

$$P = \frac{R}{\Gamma'} \tag{2.19}$$

and with pulsing:

$$P = \frac{R}{\Gamma' + \Gamma_1} \tag{2.20}$$

where $\Gamma' = R + \Gamma_0$ and Γ_1 is the additional relaxation rate with the pulses. Combining these two equations results in a measurement of the relative relaxation rates:

$$\frac{\Gamma_1}{\Gamma'} = \frac{P_{\mathrm{SERF}}}{P_{\mathrm{pulse}}} - 1 \tag{2.21}$$

We find that there are three parameters that increase the relaxation rate Γ_p: increasing the pulse repetition rate (Fig. 2.8a), increasing the pulse width (Fig. 2.8b), and decreasing the intensity of the pump light (Figs. 2.9b). The conclusion is that there is a duty cycle and pumping rate dependence to the additional relaxation rate, which strongly indicates relaxation during the pulse.

Since the pulse width is on the order of $T_{\mathrm{SE}} = 2\mu\mathrm{s}$, we assume assume that for short pulses, there can only be one spin exchange relaxing collision during a pulse. As a qualitative understanding each collision can potentially change the hyperfine level of the alkali, so if this happens after an angle ϕ out of 2π is rotated, then the electron will finish its rotation in the opposite direction. The resulting total precession angle will be off by 2ϕ at the end of the pulse. Since the field during

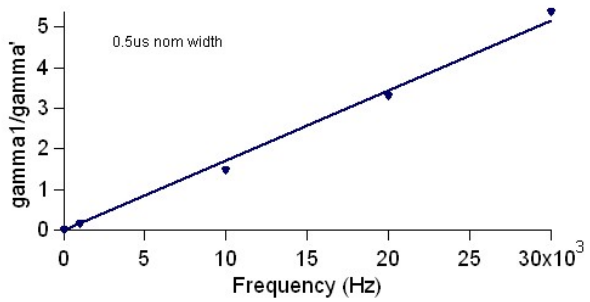

(a) The relaxation rate increases as pulse repetition rate increases.

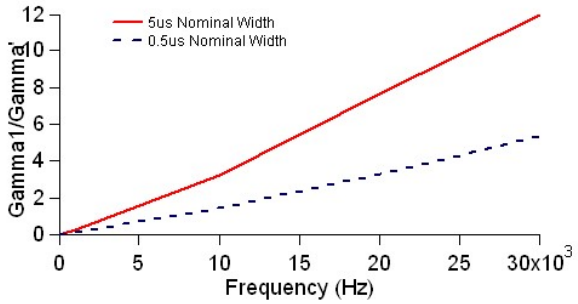

(b) The relaxation rate has a stronger frequency dependence for the longer pulse width.

Figure 2.8: The figure shows the frequency and width dependencies of the relaxation rate with 2π pulses on; it is normalized to the relaxation rate with 2π pulsing off.

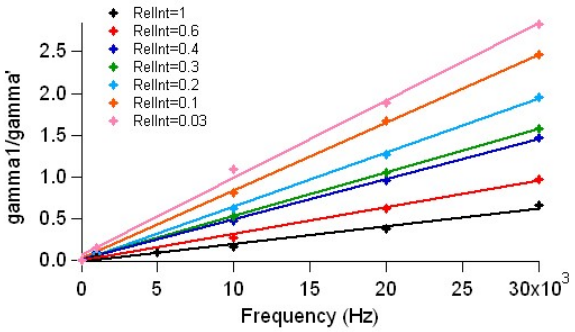

(a) The relaxation rate decreases pump intensity increases.

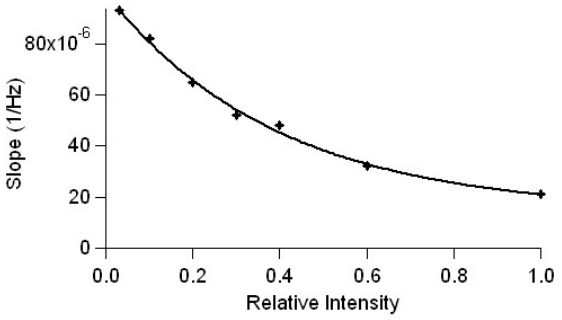

(b) The slopes of the data on the right

Figure 2.9: The figure shows the frequency dependence of the relaxation rate with 2π pulsing on as a function of pump intensity normalized to the relaxation rate without pulsing. The data points in figure (b) are the slopes of the lines in figure (a) plotted against their respective relative intensities.

a pulse is ≈ 1G, the spin-exchange rate is not fast compared to the Larmor rate; therefore, for the system as a whole, the relaxation rate due to spin exchange collisions during the pulses increases above that of the SERF magnetometer. The effect, however, is limited to the short interval of the pulse, thus resulting in the duty cycle dependence shown above.

As to the pumping rate effect, the amount the angle error contributes to relaxation is dependent on the initial polarization of the alkali atoms. As the initial polarization increases, the spin-exchange collisions are less likely to change the hyperfine level, which results in a lower relaxation rate. This light-narrowing suppression of the spin-exchange rate is utilized in other experiments as will be discussed in section 2.5.

Knowing the parameters that affect the relaxation, we can develop a model that accounts for the polarization loss we observe. Starting with a fractional angular momentum loss $\Delta F_x/F_x = \alpha(P_x)$ we can define the new relaxation mechanism:

$$\frac{d\boldsymbol{F}}{dt} = -\alpha(P_x)d\Gamma_{SE}\boldsymbol{F} = \Gamma_p\boldsymbol{F} \tag{2.22}$$

where $d = \tau f$ is the duty cycle of the pulses with width τ and frequency f. The duty cycle and $\alpha(P_x)$ describe the suppression of Γ_{SE} when using pulsed parametric resonance. The new relaxation rate is:

$$\Gamma_1 = \alpha(P_x)\tau f\Gamma_{\mathrm{SE}} \tag{2.23}$$

The function that defines $\alpha(P_x)$ is complicated by the atoms' behavior at intermediate polarizations due to the hyperfine interaction; therefore, numerical modeling is necessary to extract the behavior of the atoms as the polarization decreases from 1 to zero. Following the formalism in [Happer, Jau, and Walker, 2009], this modeling was done by assuming spin temperature and then analyzing the evolution of the density matrix accounting for the full hyperfine interaction as the alkali undergoes its 2π precession. A simplified version of this modeling is detailed in Appendix A.

The results of this modeling are seen in Fig 2.10; the y-axis is the fractional total angular momentum loss α and the x-axis is P_x. The portion between 0.6 and 1 where we usually operate closely follows a linear trend $\alpha(P_x) = \alpha'(1 - P_x)$ with $\alpha' \approx 0.3$. The nearest fit to the model for

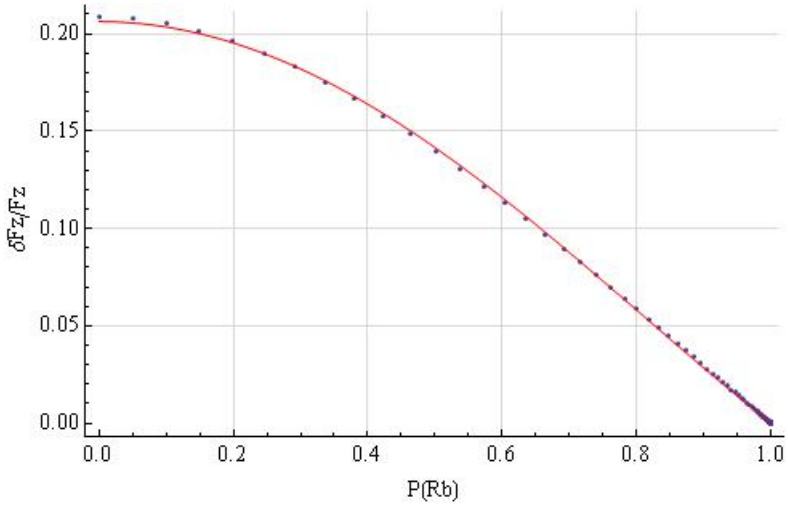

Figure 2.10: The result of the SE modeling is shown with the blue points and the nearest fit to a quadratic function (Eqn. 2.24) is shown in red. The model calculates the fractional angular momentum loss due to the 2π pulsing as a function of Rb polarization.

all polarizations is:

$$\alpha(P_x) = 0.2063 - 0.2762P^2 + 0.06995P^4 \tag{2.24}$$

as shown in red in Fig 2.10.

In order to analyze the experimental data to see whether or not it fits to the model we take the data that shows the frequency, pulse rate, and polarization dependence of the relaxation rate and organize it to extract values for α . Taking the analysis similar to that which gave us Eqn. 2.21 we get

$$\frac{P_{\mathrm{SERF}}}{P_{\mathrm{pulse}}} - 1 = \alpha(P_x)\tau f + af \tag{2.25}$$

The additional term af is used to account for an observed offset that we assume is due to imperfect pulsing. These imperfections are most likely pulse width and repetition rate fluctuations. The frequency f is the applied pulse repetition rate. When $(\frac{P_{\mathrm{SERF}}}{P_{\mathrm{pulse}}} - 1)/f$ is plotted against τf, the slope of the resulting line is $\alpha(P_x)$. We can do these measurements at different densities, which correspond to different spin-exchange rates: $\Gamma_{\mathrm{SE}} = \kappa_{\mathrm{SE}}[Rb]$ and $\Gamma_1 = d\Gamma_{\mathrm{SE}}\alpha(P_x)$ to get an even broader understanding of the behavior.

The above analysis needs to be expanded, however, to account for the slowing down factor, which is vital for an accurate understanding of the data. The slowing down factor describes the fraction of the total angular momentum stored in the electron spin: $F = qS$, where q is the slowing down factor. At high polarizations it is $2I + 1$ (4 for ^{87}Rb and 6 for ^{86}Rb) where I is the nuclear spin; it increases to 6 for ^{87}Rb at low alkali polarizations. When we pull it into the analysis:

$$q\frac{dS_x}{dt} = \frac{R|j_{-1}|^2}{2} - \Gamma'\frac{P_x}{2} - \Gamma_p\frac{qP_x}{2} \tag{2.26}$$

Becomes, in steady state

$$P_x = \frac{R|j_{-1}|^2}{\Gamma' + q\Gamma_p} \tag{2.27}$$

which reduces to

$$\frac{P_{\mathrm{SERF}}}{P_{\mathrm{pulse}}} - 1 = \frac{q\Gamma_p}{\Gamma'} \tag{2.28}$$

so that

$$\Gamma_p = \frac{\Gamma'}{q}\Big(\frac{P_x(0)}{P_x(f)} - 1\Big) = \alpha(P_x)\tau f k_{\mathrm{SE}}[Rb] + \Gamma_{p0} \tag{2.29}$$

We add the term $\Gamma_{p0} = af$ as we did for Eqn. 2.25 to account for the fact that when extrapolating Γ_p, it does not go through zero. Mapping out

$$\alpha(P_x) = \frac{\Big(\frac{P_x(0)}{P_x(f)} - 1\Big)\frac{\Gamma'(P_x)}{q(P_x)}\frac{1}{f} - a}{\tau\Gamma_{\mathrm{SE}}} \tag{2.30}$$

as a function of the different measured parameters τ, f, [Rb], pumping rates, and offset a, we obtain curves such as in Fig. 2.11, which shows all the parameters varied at a constant pulse width $\tau = 1\mu s$. With no free parameters, the extracted data generally match the model to within 20%. We did a similar analysis for several different pulse widths ranging from $1-8\mu s$ and extracted $\alpha(0)$ by scaling the numerical factor equation; this results in an experimentally meaured $\alpha(0) = 0.2 \pm 0.01$. The results of this procedure are seen in Fig. 2.12. The data agree well with the model, showing a light-narrowing suppression as well as a duty cycle suppression of the spin-exchange relaxation rate.

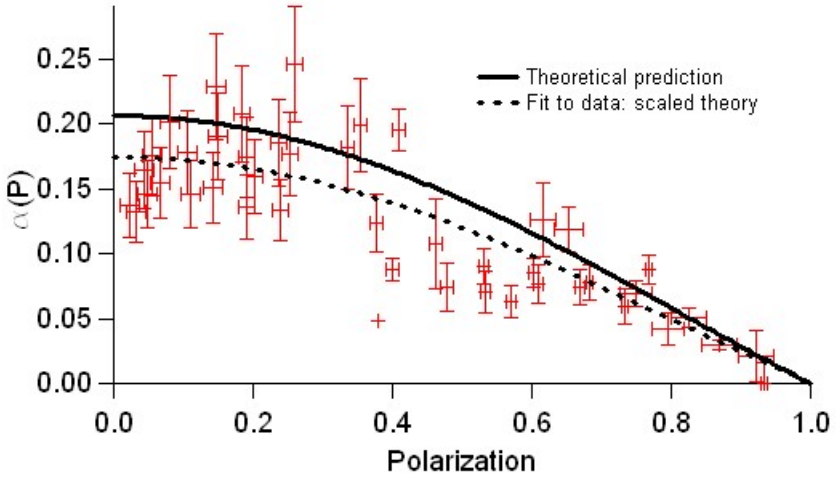

Figure 2.11: Each data point corresponds to an α value extracted from measurements of the pulse width, pulse repetition rate, Rb polarization, and Γ' as well as the known values of κ_{SE} and $q(P_x)$ as described in Eqn. 2.30. The data presented here is for a single pulse width $\tau = 1.5\mu$s.The two curves shown are the theoretical prediction (solid black) and the theoretical prediction scaled by a constant (dashed black).

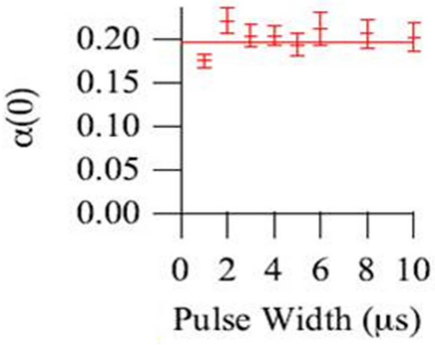

Figure 2.12: This plot combines multiple sets of data for different pulse widths and extracts $\alpha(P = 0)$. These points give a scaled $\alpha(0) = 0.2 \pm 0.01$, while theory predicts $\alpha(0) = 0.21$.

2.5 Comparison to SERF and Light Narrowed Magnetometer

The success of the PPR magnetometer is determined by whether or not, with the suppression of the spin-exchange relaxation, we are able to maintain magnetometer sensitivity comparable to SERF sensitivity when working in a large magnetic field. Since the SERF magnetometer is not designed to work in high magnetic fields, we also compare the PPR magnetometer to methods configured to work in similar regimes. For the purposes of simplicity in our comparisons, we direct the pumping light along the bias field direction and detect the response to changes in Ω_x.

The response of a magnetometer is determined by the slope of the response of the sensitive direction. From Eqn. 2.4 with $\hat{z}$ pumping and $\hat{y}$ detection the SERF magnetometer detects:

$$P_y = \frac{R\Omega_x}{\Gamma'^2 + \Omega_x^2} \tag{2.31}$$

which is only valid in small fields. Here $\Gamma' = R + \Gamma_0$, so if we optimize Eqn. 2.31 for pumping rate, we obtain $R = \Gamma_0$. Then, to find the magnetometer's response, take the derivative of Eqn. 2.31 with respect to Ω_x and get

$$\mathcal{M} = \frac{(4\Gamma_0^2 + \Omega_x^2)\Gamma_0 - 2\Gamma_0\Omega_x^2}{(4\Gamma_0^2 + \Omega_x^2)^2} \tag{2.32}$$

Setting $\Omega_x = 0$, the resulting magnetometer response is $\mathcal{M} = \frac{1}{4\Gamma_0}$.

Doing a similar procedure for the PPR magnetometer where we now have $\Gamma_2 = \Gamma'/q + \alpha d\Gamma_{\mathrm{SE}}$, we start with the steady state solution for P_y:

$$P_y = \frac{R\Omega_x}{\Gamma_2^2 + \Omega_x^2} \tag{2.33}$$

and take its derivative to find the sensitivity

$$\mathcal{M} = \frac{(\Omega_x^2 + \Gamma_2^2)R - 2R\Omega_x^2}{(\Gamma_2^2 + \Omega_x^2)^2} \tag{2.34}$$

Once again, we are operating where $\Omega_x = 0$ and the sensitivity reduces to $\mathcal{M} = R/\Gamma_2^2 = P/\Gamma_2$ with $\Gamma_2 = \Gamma_0 + R + d\alpha(1 - P_x)\Gamma_{\mathrm{SE}}$. In order to optimize for the pumping rate that maximizes sensitivity, we must simultaneously solve $P = R/\Gamma_2$ and $\mathcal{M}$ to extract $\mathcal{M}(R)$ then find $\delta_R\mathcal{M} = 0$.

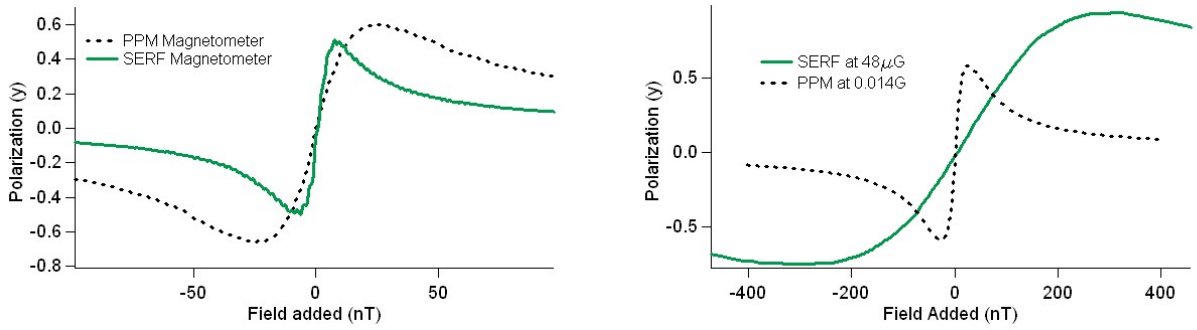

(a) SERF and PPR at zero field

(b) SERF and PPR in high magnetic field

Figure 2.13: Figure (a) is an experimental comparison of the SERF and PPR magnetometer responses at zero field. The difference in their responses is a factor of 3.5. Figure (b) is a comparison of the SERF magnetometer operating at "high" magnetic field and the PPR magnetometer operating at high magnetic field. Although the bias field for the SERF case is $300\times$ smaller than the bias field for the PPR magnetometer the PPR magnetometer's response is $10\times$ higher.

This results in $R = \sqrt{\Gamma_0 \alpha' q d \Gamma_{\rm SE} + \Gamma_0^2}$, which is higher than the optimum pumping rate for the SERF magnetometer due to the additional relaxation. Plugging this value of R into Eqn 2.34 on resonance, we obtain a PPR magnetometer sensitivity of

$$\mathcal{M} = \frac{[Rb]|j_{-1}|^2}{2\sqrt{\Gamma_0 \alpha' q d \Gamma_{\rm SE}} + \Gamma_0} \tag{2.35}$$

Figure 2.13a shows the comparison between a SERF and PPR magnetometer. There is a factor of 3.5 between the slopes of their responses. If we plug into Eqn 2.35 the experimentally measured values $\Gamma_0 = 500/\text{s}$, $\alpha' = 0.3$, $d = 0.05$, q, and $\Gamma_{\rm SE} = 2 \times 10^5/\text{s}$ we calculate that the ratio should be 3, which puts us in reasonable agreement. Figure 2.13b is a comparison between a SERF magnetometer operating in a relatively high magnetic field and a PPR magnetometer. Take note that the magnetic field for the PPR is $300\times$ larger than the field for the SERF magnetometer, but its response is still $10\times$ higher.

The other more relevant point of comparison is between the response of the PPR magnetometer to an analogous magnetometer operating where $\Omega_z >> \Gamma_{\rm SE}$. The scalar magnetometer described in Ref. [Smullin et al., 2009] operates with a bias field B_0 along the direction of the pumping.

A transverse RF field at $\omega_1 = \gamma B_0$ is then applied, and the response to other transverse fields is detected. The RF amplitude is optimized for maximum signal and its frequency is scanned through resonance, resulting dispersive and absorptive signals. The Rb is at high polarizations in this magnetometer and is therefore "light narrowed" in a way analagous to the $(1-P)$ dependence of the PPR magnetometer: $\Gamma_2 \approx \Gamma_{\mathrm{SE}}(1-P)/5$ [Smullin et al., 2009]. A simplistic analysis indicates that the linewidth of the optimized PPR should be 13 times narrower than the optimized light-narrowed scalar magnetometer.

Figure 2.14a shows a comparison of individually optized PPR and scalar magnetometers. The PPR magnetometer has a sensitivity that is 33 times greater than the scalar magnetometer. If we remove the light narrowing effect by operating at low polarizations, we obtain linewidths as seen in Fig 2.14b. The PPR magnetometer's linewidth is still narrow due to the duty cycle suppression of the spin exchange relaxation rate, while the scalar magnetometer line has broadened since it is no longer benefiting from the full $(1-P)$ spin-exchange suppression.

2.6 Significance

In conclusion, using pulsed parametric modulation to operate an atomic magnetometer in high fields is successful. We have nearly restored SERF sensitivity in fields orders of magnitude above SERF operating conditions. Additionally, the PPR magnetometer out performs other types of magnetometers that operate in equivalent fields. However, one may naively say the result is inconsequential, arguing what we are doing is adding a large magnetic field "shim" to cancel another large magnetic field; the only difference is that instead of a DC cancelling field, we apply an AC coupled pulsed field, which is worse because it has this additional relaxation. What this method gains us over and above simply shimming out the bias field is that the alkali polarization is transverse to the bias field. By itself, this may not be particularly interesting, but the beauty and usefulness of this method is seen in its applications, which will be the subject of the rest of this thesis.

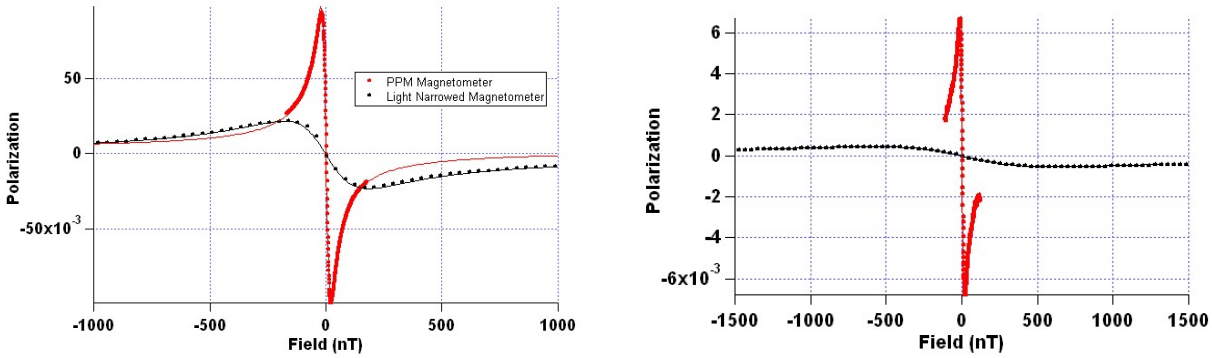

(a) High polarization PPR vs light narrowed

(b) Low polarization PPR v light narrowed

Figure 2.14: Figure (a) is a comparison of the PPR magnetometer to a light narrowed magnetometer [Smullin et al., 2009]. Both magnetometers benefit from the light narrowing effect. Beyond the light narrowing effect, the PPR also suppresses spin-exchange relaxation collisions via the duty cycle effect, so its response is $33\times$ greater than the light narrowed magnetometer. If we essentially take away the light narrowing effect, we obtain the comparison in (b) where the PPR magnetometer is virtually unchanged and the light narrowed magnetometer's response is greatly suppressed. This demonstrates the effectiveness of the duty cycle suppression of which the PPR magnetometer takes advantage.

2.7 Strange Results from Sinusoidal Longitudinal Operation

As a side note, we experimented with another method of high field operation that gave us unexpected results. We originally thought that the best comparison would be to a longitudinal, sinusoidal parametric modulation magnetometer, which is another method for operating in high bias field conditions. This magnetometer is set up so that the pump light is along the same direction as the bias and the oscillating field.

The analysis is similar to the transverse case. We start with the transverse spin components $S_+ = S_x + iS_y$ and look at their time evolution:

$$\frac{dS_+}{dt} = i(\Omega_z + \Omega_1(t))S_+ - i\Omega_+ S_z - \Gamma_2 S_+ \tag{2.36}$$

Making the rotating wave spproximation such that $S_+ = A_+ e^{i\phi_1}$ where $\phi_1 = \int \Omega_1 dt$ this gets us to

$$\frac{dA_+}{dt} = (i\Omega_z - \Gamma_2)A_+ - i\Omega_+ S_z e^{-i\phi_1} \tag{2.37}$$

Fourier expanding $e^{i\phi} = \sum_P J_p^* e^{-ip\omega t}$ and $A_+ = \sum_P A_{+p} e^{-ip\omega t}$ we reduce to

$$A_+ = \frac{-i\Omega_+ S_z J_{-1}^*}{\Gamma_2 - i(\Omega_z - \omega_1)} \tag{2.38}$$

Then translating back to S_+ on resonance $\Omega_z - \omega_1 = 0$

$$\langle S_+ \rangle = \frac{-i\Omega_+ S_z}{\Gamma_2} |J_{-1}^*|^2 \tag{2.39}$$

Substituting in for $S_z = \frac{R}{\Gamma'}$

$$\langle S_y \rangle = \frac{-\Omega_x R}{\Gamma_2 \Gamma'} |J_{-1}^*|^2 \tag{2.40}$$

The best case scenario is the SERF regime where $R = \Gamma_0$. At high Rb polarization, for sinusoidal parametric modulation $\Gamma_2 \approx \Gamma_{SE}(1 - P_z)/5$ and for pulsed parametric modulation $\Gamma_2 \approx d\alpha' \Gamma_{SE}(1 - P_z)$; therefore in the pulsed case, the spin-exchange relaxation contribution to Γ_2 should be reduced further than the sinusoidal case by $d\alpha'$. Also, in the sinusoidal case, the maximum transeverse polarization that can be achieved is 0.3, whereas it is 1 in the pulsed case.

Using the simplistic expression $\Gamma_2 = \Gamma_0 + R + \Gamma_{\mathrm{SE}}(1 - P_z)$, we can find the optimum pumping rate to be $R = \sqrt{\Gamma_0^2 + \Gamma_{\mathrm{SE}}\Gamma_0}$. If we plug in the optimized pumping rate then calculate the response

of the longitudinal sinusoidal magnetometer, we find, theoretically, that the PPR should be $20\times$ more sensitive than the longitudinal sinusoidal magnetometer. As can be seen in Fig2.15, this is not the case experimentally. This was a surprising result; the longitudinal sinusoidal modulated magnetometer performed much better than we expected and we never found a way to break it.

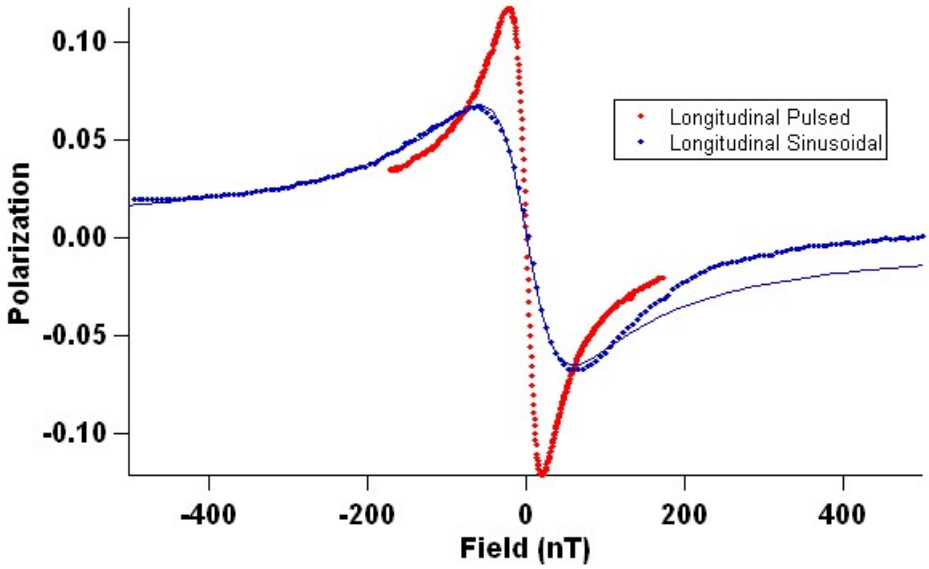

Figure 2.15: This figure shows the strange results we obtained for the longitudinally pumped sinusoidally modulated magnetometer. The pulsed case is only a factor of 3 better than the sinusoidal case, whereas we would expect a factor of ≈ 20 for optimized conditions.

Chapter 3

Synchronous Spin Exchange Optical Pumping

In this chapter, we expand the use of transverse optical pumping from high field magnetometry to NMR. The basic innovation is to replace the usual DC bias field by a sequence of alkali 2π pulses. A simplistic, but accurate way of understanding how our pulsed bias field works is to consider the rotation due to the pulsing field experienced by a noble gas nucleus as compared to the rotation experienced by an alkali electron. Due to the vastly different gyro-magnetic ratios, a 2π pulse for ^{87}Rb is equivalent to a $2\pi\gamma_{Xe}/\gamma_{Rb} = 0.005$ radian rotation for ^{131}Xe and a 0.016 radian rotation for ^{129}Xe. The 2π bias field therefore causes the noble gas isotopes to rotate in a manner similar to a DC field, but the alkali experience no net precession. To do NMR we reverse the alkali polarization twice every noble gas Larmor period, forcing the alkali and the noble gas to co-precess despite the factor of 1000 difference in their gyromagnetic ratios. This is what we call synchronous spin exchange optical pumping (SSEOP). The essential components required to demonstrate SSEOP are seen in Fig. 3.1a. To the PPR magnetometer setup, Fig. 3.1b, we have added liquid crystal variable retarders that flip the handedness of the circularly polarized pump beams, which in turn flips the alkali polarization synchronously with the noble gas precession.

The resonance frequency is detected via the embedded magnetometer, which has benefits and drawbacks. One serious drawback is that the polarized alkali atoms produce a large magnetic field that can shift the NMR frequency. The new method discussed here that utilizes transverse optical pumping with pulsed parametric modulation, eliminates the alkali field shift.

This chapter discusses the successful implementation of synchronous spin exchange optical pumping and shows a factor of at least 2500 suppression of the alkali field shift. Although this method gets rid of the frequency shift of the alkali field, it does not eliminate the alkali field itself.

The linewidth broadening effect of the now perpendicular alkali field is also detailed here along with its compensation.

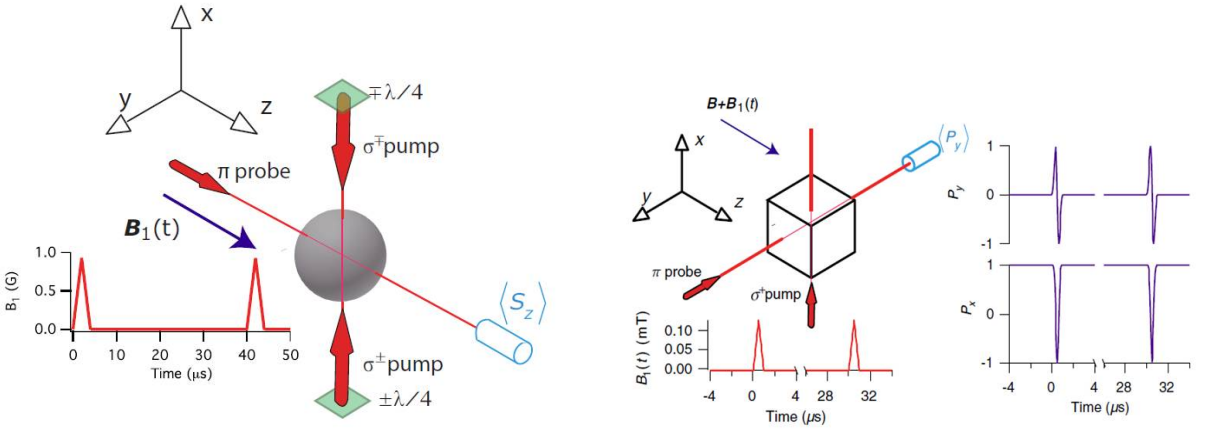

(a) Synchronous SEOP **(b)** PPR Magnetometer

Figure 3.1: Simplified schematics are shown of the optical setup for transverse optical pumping (b) and synchronous spin exchange optical pumping (a). The major changes from (b) to (a) are dual sided pumping, the insertion of the liquid crystal variable retarders to flip the pump polarization, and the probe along $\hat{z}$ instead of $\hat{y}$. The bias field has also changed from $B + B_1(t)$ to just $B_1(t)$ due to the fact that we no longer AC couple the 2π pulses, so there is no longer a large DC field being applied.

3.1 Synchronous Spin Exchange Optical Pumping

This new method operates on the basic principles of spin exchange optical pumping. Starting with a vapor of alkali metal atoms and a high density of noble gas, circularly polarized light first imparts angular momentum to the alkali atoms's valence electron giving it a certain spin polarization (as described in Sec. 2.1). Subsequently, through collisions with the noble gas, the alkali's electron exchanges some of its angular momentum with the nucleus of the noble gas, so that it becomes spin polarized. The two primary means of angular momentum exchange between the noble gas and the alkali are binary collisions and van der Waals molecules, which will be discussed in more detail in Sec. 4.2.5. In conventional NMR, transverse noble gas polarization is

generated by the application of a resonant transverse rf field and the subsequent precession about the bias field is detected by the embedded magnetometer.

To implement SSEOP, we turn on the 2π pulsing that corresponds to a certain bias field $B_{\rm bias} = f_{\rm pulse}/\gamma_{\rm Rb}$ where $\gamma_{\rm Rb} = 2\mu_B/(2I+1)$ from which the Xe resonance frequency is calculated $f_{\rm res} = \gamma_K B_{\rm bias} = \gamma_K/\gamma_{\rm Rb} f_{\rm pulse}$. The liquid crystal modulators then flip the pump polarization, i.e. the alkali polarization, at a frequency f near the Xe resonance frequency. The oscillating Rb polarization, which replaces the electro-magnetic drive in conventional NMR, synchronously pumps the noble gas. As the Xe precesses, it produces an oscillating field B_y, which is directly detected by the magnetometer via Faraday rotation of the $\hat{z}$ probe. Figure 3.2a shows an example of what the Xe signal looks like on resonance. Because the magnetometer gain changes sign twice every noble gas Larmor period, the Xe precession signal is a square wave modulated sine wave. This signal is then fed into a lock-in that detects at $2f$. Figure 3.2b shows a sample resonance linewidth taken by scanning the alkali polarization modulation frequency f. The red trace is the in phase component of the Xe signal and the blue trace is the quadrature signal, 90° out of phase with the red. The black is the K_z component of the Xe spin that produces a $\hat{z}$ field (the mechanism that generates a $\hat{z}$ polarization will be discussed in detail below). In order to observe the K_z signal, we apply a small, low frequency (1kHz) field along $\hat{x}$. This acts as a parametric modulation that, when demodulated, allows us to detect the field that is parallel to the probe propagation direction. It is small enough and low enough frequency that it does not perturb the 2π pulse rotation, but still gives us sufficient signal to detect B_z as produced by K_z.

The time evolution of the transverse components of the nuclear spin, $\langle K_+\rangle = \langle K_x + iK_y\rangle$, of the noble gas is given by:

$$\frac{d\langle K_+\rangle}{dt} = -(\Gamma_2 + i\gamma_K \bar{B}_{\rm bias})\langle K_+\rangle + \Gamma_{\rm SE}\langle S_x\rangle(t) \tag{3.1}$$

where Γ_2 is the transverse relaxation rate; γ_K is the gyromagnetic ratio of the noble gas; $\bar{B}_1$ is the average magnetic field of the alkali 2π pulses, which defines the noble gas precession $\omega_0 = \gamma_k \bar{B}_1$; $\Gamma_{\rm SE}$ is the spin exchange rate between the alkali and the noble gas; and $\langle S_x\rangle(t)$ is the optical pumping waveform that describes the flipping of the alkali polarization. If we then define the

optical pumping term so that $\langle S_x \rangle(t) = \sum_p s_p e^{-ip\omega t}$ the steady state solution is

$$K_+ = \frac{\Gamma_{\rm SE} s_p}{\Gamma_2 + i(\omega_0 - p\omega)} e^{-ip\omega t} = \widetilde{K_+} e^{-ip\omega t} \tag{3.2}$$

where we have defined $\widetilde{K_+}$ as the transverse polarization in the rotating frame. The magnitude of this polarization is $K_{\max} = \Gamma_{\rm SE} s_p / \Gamma_2$. We measure the two components $\tilde{K_x}$ and $\tilde{K_y}$. Both of these should have a maximum noble gas field of $K_{\max}$ and a linewidth of Γ_2. Typically, unless limited by field gradients, $\Gamma_2 = \Gamma_1$.

3.2 Importance of the Alkali Field: Broadening

As mentioned in Sec. 1.1 the importance of this method is derived from the fact that, due to the co-precessing Rb and Xe, the alkali field shift of the Xe resonance frequency has been eliminated. For this reason, all preliminary analysis of the system was done neglecting the contribution of B_A to the time evolution of the noble gas spins. However, there are several pieces of evidence that this is not the case. The first is that the raw signal itself exhibits no phase shift as seen in Fig. 3.2a; the blue Xe signal trace is detuned one linewidth from resonance. The lack of phase shift is dramatically demonstrated when looking at the quadrature signal from the lock-in. Fig. 3.2b shows the in phase, quadrature, and B_z signals as resonance is scanned. The linewidth of these curves is much broader than expected and the quadrature signal is almost zero. Also surprising is the fact that there is a B_z signal from the Xe nuclei that are supposed to be rotating solely in the $\hat{x}$ -$\hat{y}$ plane.

3.2.1 Accounting for Alkali Field

If we now add in the effect of the alkali field, we see that when the pumping is off resonance, a phase shift between the alkali and the noble gas is accumulated. The alkali field exerts a torque on $\tilde{K_y}$, which will tip the nuclear spin into $\hat{z}$: $-\gamma_K B_{KS} \times \langle K \rangle = \gamma_K B_{KS} \widetilde{K_y} \hat{z}$. We define $b_{KS}\bar{S}$ as the alkali field that the Xe sees and $b_{SK}\bar{K}$ as the Xe field the alkali sees. This is the cause for the unexpectedly large $\hat{z}$ component of the noble gas polarization, and can be seen as the reason for the suppression of $\tilde{K_y}$. Factoring in the torque felt by the nuclei due to the alkali field on the time

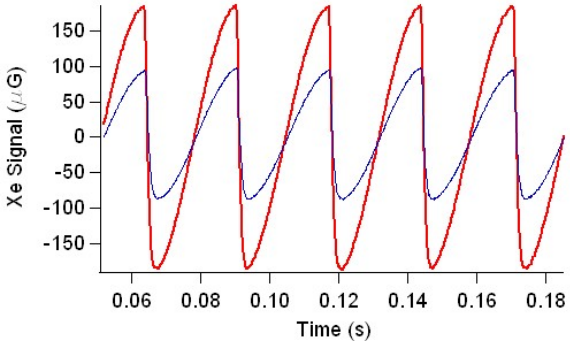

(a) Uncompensated Xe signals

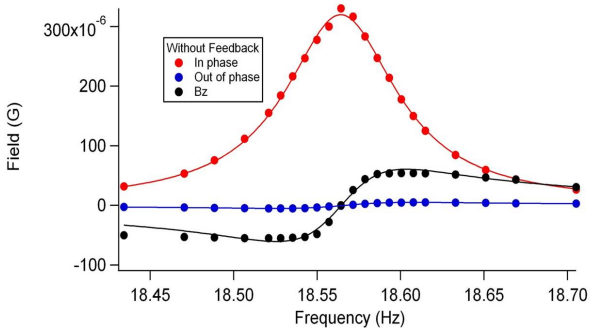

(b) Uncompensated Xe linewidths

Figure 3.2: The two figures correspond to the Xe signal and accompanying linewidths for a system that does not compensate for the alkali field. In (a) the red trace is the on resonance signal and the blue trace is tuned halfway down the in phase resonance curve; there is no apparent phase shift in the signal. Figure (b) shows the dramatic suppression of the quadrature component of the signal in blue.

evolution of the $\hat{z}$ component of the Xe:

$$\frac{dK_z}{dt} = -\gamma_k b_x(t) K_y - \Gamma_1 K_z \tag{3.3}$$

The alkali field $b_x(t) = b_{KS}\langle S_x\rangle(t)$ is oscillating in phase with S_x as in Eqn 3.1 so we obtain in steady state:

$$K_z = -\frac{\gamma b_{\mathrm{x,p}} \tilde{K_y}}{\Gamma_1} = -\tan(\alpha)\tilde{K_y} \tag{3.4}$$

where we have defined the parameter $\tan\alpha = \frac{\gamma_K b_{\mathrm{x,p}}}{\Gamma_1}$ as the angle the Xe tilts into $\hat{z}$ due to the torque exerted by the alkali field. The parameter $b_{\mathrm{x,p}}$ is the p^{th} Fourier amplitude of the alkali field.

Now seeing the effect $B_A\hat{x}$ has, we want to know how it changes the characteristic lineshapes we measure. For the transverse noble gas polarization

$$\frac{dK_+}{dt} = \Gamma_{\mathrm{SE}} S_x(t) - (\Gamma_2 + i\gamma_K B_1(t))K_+ + i\gamma_K b_x(t) K_z \tag{3.5}$$

this can be reduced to

$$\frac{dK_+}{dt} = -K_+(\Gamma_2 + i\omega_0) + (\Gamma_{\mathrm{SE}} s_p - i\Gamma_1 \tan\alpha^2 \widetilde{K_y}) e^{-ip\omega t} \tag{3.6}$$

Defining $\Delta = p\omega - \omega_0$ we can separate Eqn 3.6 into its real and imaginary steady state components to obtain

$$\widetilde{K_x} = \frac{\Gamma_{\mathrm{SE}} s_p - \widetilde{K_y}\Delta}{\Gamma_2} \tag{3.7}$$

and

$$\widetilde{K_y} = \frac{\widetilde{K_x}\Delta}{\Gamma_2 + \Gamma_1 \tan\alpha^2} \tag{3.8}$$

Solving these two equations simultaneously gives

$$\widetilde{K_+} = \frac{K_{\max}}{1 + \frac{\Delta}{\Gamma_{\mathrm{eff}}}}\left(1 + \frac{i\Delta\Gamma_2}{\Gamma_{\mathrm{eff}}^2}\right) \tag{3.9}$$

where $K_{\max} = \Gamma_{\mathrm{SE}} s_p/\Gamma_2$. The new effective linewidth that we measure with the alkali field taken into account is

$$\Gamma_{\mathrm{eff}} = \sqrt{\Gamma_2^2 + \Gamma_1\Gamma_2 \tan^2(\alpha)} \tag{3.10}$$

which is broadened over Γ_2 by a term proportional to the alkali field squared. The second term of Eqn. 3.9 which describes the quadrature behavior, is suppressed by a factor $\Gamma_2/\Gamma_{\text{eff}}$. These new equations describe the behavior of data.

As an interesting side note, this broadening effect is very similar in form to power broadening as presented in Abragam, 1990. Conceptually the analogy is that as the noble gas tilts into the z-axis, the alkali field is acting as an electromagnetic drive that is essentially over-driving the noble gas resonance. This causes braodening of the linewidth:

$$\Gamma_{\text{eff}} = \sqrt{\Gamma_2^2 + \frac{\Gamma_2}{\Gamma_1}\gamma^2 B^2} \tag{3.11}$$

The difference between the two effects is that the effect we see conserves the peak value; as the linewidth broadens, the peak polarization remains constant. This is because on resonance, there is no phase shift between the alkali and the noble gas, thus no torque. Other broadening mechanisms like power broadening see a decrease in the peak value on resonance.

3.2.2 Alkali Field: Narrowing

The important feature of the alkali field is that it follows the alkali polarization modulation waveform, which is a square wave; therefore, we are able to essentially turn it off by applying a square wave magnetic field along $\hat{x}$ 180° out of phase with the alkali polarization modulation. This means that in Eqn 3.3 we now put $b_x(t) = b_{KS}\langle S_x\rangle(t) - B_c(t)$ where $B_c(t)$ is the compensation field. The effect of this compensation field is dramatic. The plot in Fig 3.3a shows the in phase, quadrature, and $\hat{z}$ components of the resonance without the compensating field on and Fig 3.3b shows the same signals with the compensating field. Doing this procedure narrows the linewidth a factor of ≈ 15 and enhances the quadrature slope up to a factor of ≈ 75 at high density. A very clear way to see that the phase sensitivity is restored is to look at the raw Xe signal again and see that the blue trace in the uncompensated case of Fig. 3.4 now demonstrates a phase shift. As can be seen, the $\hat{z}$ signal is suppressed, but not entirely eliminated; suppressing it beyond this point does not significantly affect the in and out of phase signals, but, with more careful nulling, we have been able to achieve over a factor of 30 suppression of the induced $\hat{z}$ field.

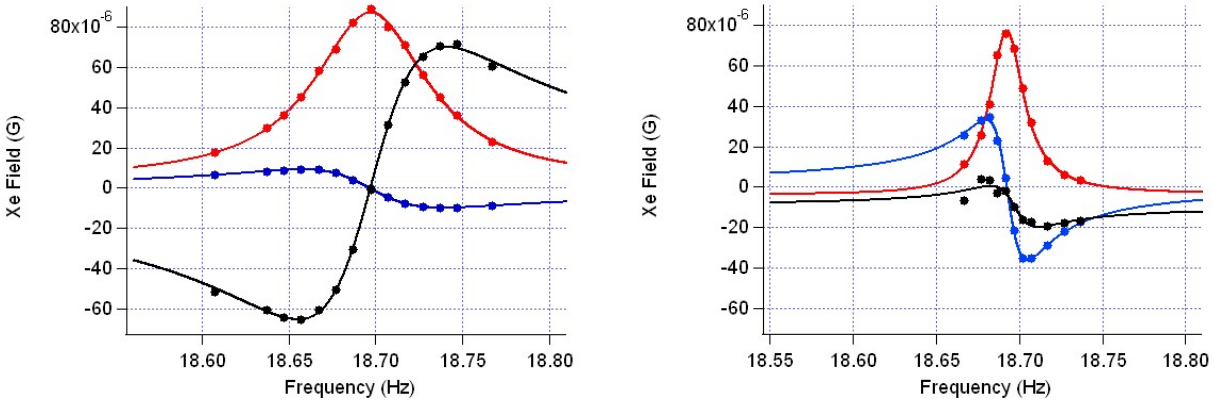

(a) Uncompensated linewidths

(b) Compensated linewidths

Figure 3.3: The addition of a B_x field to compensate for the alkali field produces a change in the in phase, quadrature, and B_z signals as shown from (a) to (b). The inewidth narrows a factor of 15 and the quadrature slope enhances a factor of up to 75 at high density.

Careful adjustment of the compensation field is then done by scanning across resonance to minimize K_z. This procedure is complicated by the fact that both the amplitude and the phase of the compensating field must be adjusted in order to obtain perfect cancellation. The phase of the compensating field depends on how quickly the alkali atoms flip their polarization, which causes a slight delay in the alkali field timing from the triggered polarization flip. If the phase is not adjusted, then the amplitude of the in phase signal is significantly reduced as can be seen in Fig 3.5. There is a residual loss in amplitude that cannot be compensated for by phase or field adjustment.

As a measure of how well we compensate, the width of the in phase and the slope of the quadrature can be plotted as a function of compensating field. They should minimize/ maximize at the alkali field value. The measurement is taken by starting where the compensation field amplitude and phase are well adjusted to the alkali field; then points with different compensation field amplitudes are taken. The width of the in phase signal as a function of compensation field should follow

$$\text{width} = \sqrt{\Gamma_2^2 + \frac{\Gamma_2}{\Gamma_1}\gamma^2(B - B_c)^2} \tag{3.12}$$

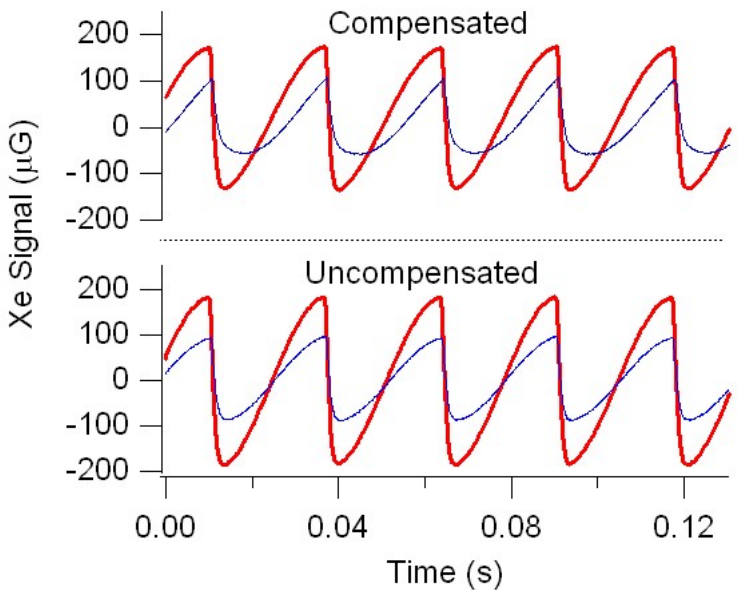

Figure 3.4: The uncompensated and compensated Xe signals show the enhanced phase behavior of the signal. The blue traces in the above signals correspond to the Xe signal detuned by one linewidth. Because of the narrowing, the compensated signal is detuned only 5mHz, while the uncompensated signal is detuned 50mHz. The phase shift is now apparent in the signal.

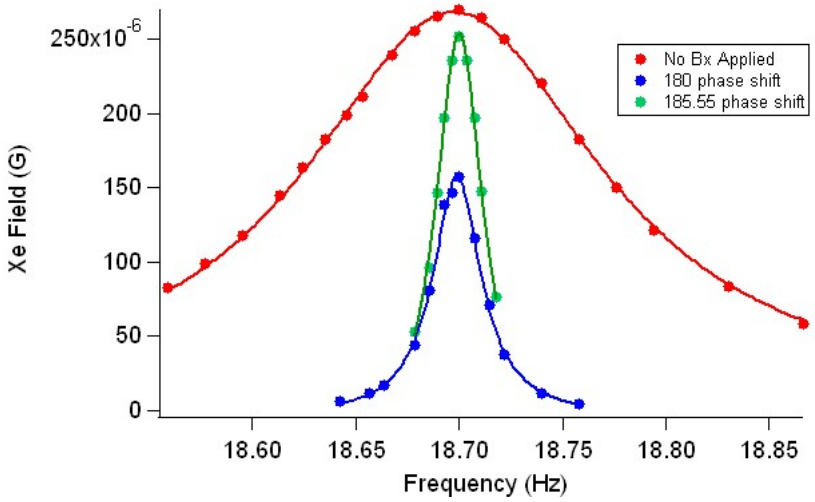

Figure 3.5: The phase of the alkali compensation field must be adjusted to maintain maximum Xe amplitude. The blue and the green curves are taken at the same applied compensation field, but are different in phase by $5.55°$. There is a residual loss in amplitude that cannot be compensated for by phase or field adjustment.

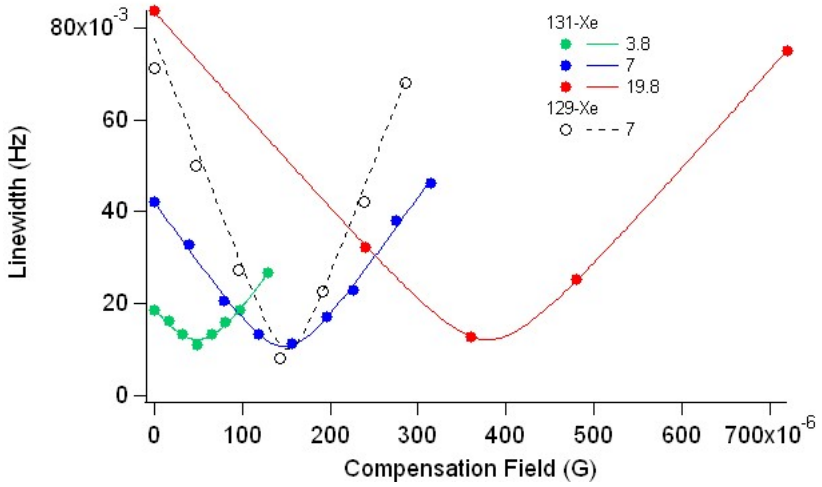

Figure 3.6: The linewidth as a function of compensation field value shows the narrowing effect at several different densities for ^{131}Xe and at one density for the third sub-harmonic of ^{129}Xe. The measured compensation field point agrees fairly well with the calculated alkali field.

and the slope of the quadrature signal should follow:

$$\frac{d\tilde{K_y}}{d\Delta}|_{\Delta\to 0} = \frac{K_{\max}\gamma_2}{\Gamma_2^2 + \Gamma_1\Gamma_2 \tan\alpha^2} \tag{3.13}$$

The data and fits for this experiment are shown in Fig 3.6. We also took this data at several different densities, which correspond to several different alkali field values.

A regime that was not fully explored was that of very high alkali densities corresponding to very high alkali fields. We suspect that as the alkali field increases at higher densities, we will start to see a feedback effect between the large $B_{SK}K_z$ and the large B_A.

3.3 Sub-Harmonic Pumping

A neat feature that we exploited for some of these experiments is using the higher harmonics generated by our square wave polarization modulation to synchronously pump ^{129}Xe at a lower pump modulation frequency $\gamma_K B/p$. When we do this the Fourier amplitude is reduced by $j_p = 2/\pi p$ where p is the harmonic number; this means $\tan\alpha = \frac{2\gamma_K(b_A - b_C)}{p\pi\Gamma_1}$ is reduced and the broadening is not as pronounced.

We start, once again, with the time evolution of the noble gas (Eqn 3.5):

$$\frac{dK_+}{dt} = R\text{sign}[\cos(\omega t)] - (\Gamma_2 + i\gamma_K B_1(t))K_+ + i\gamma_K B_A \text{sign}[\cos(\omega t)]K_z \tag{3.14}$$

Fourier expanding and assuming a single resonance $\mathrm{s}\cos(\omega t) = j_p e^{-ip\omega t}$ where

$$\frac{dK_+}{dt} = Rj_p e^{-ip\omega t} - (\Gamma_2 + i\gamma_K B_1(t))K_+ + i\gamma_K B_A j_p e^{-ip\omega t} K_z \tag{3.15}$$

where the Fourier coefficient

$$j_p = \frac{2}{p\pi}(-1)^{p-1/2} \tag{3.16}$$

Multiplying and dividing the first two terms by Γ_1 allows us to redefine both the maximum polarization:

$$K_{\perp,\max} = \frac{j_p R}{\Gamma_1} \tag{3.17}$$

and the new $\tan\alpha$

$$\tan\alpha = \frac{j_p \gamma_K B_A}{\Gamma_1} \tag{3.18}$$

Both of these terms are now reduced by the Fourier coefficient j_p as defined above. A scan of the pump polarization modulation frequency is shown in Fig 3.7. The third subharmonic of ^{129}Xe is inverted, reduced in amplitude by j_p, and narrower due to the smaller $\tan\alpha$ as compared to the first harmonic.

Because the signal is squarewave modulated, it is important to lock to the correct harmonic and know the subsequent reduction in amplitude. The signal into the lock-in is the square wave (at ω) modulated Xe signal (at $p\omega$), which has the largest signal component at $p \pm 1$, with smaller components at $p \pm 3$ etc. So the lock-in out of phase signal:

$$V_{\text{out}} \propto \langle \text{sign}[\cos(\omega t)] \sin(p\omega t) \sin((p+1)\omega t) \rangle \tag{3.19}$$

and the in phase signal

$$V_{\text{in}} \propto \langle \text{sign}[\cos(\omega t)] \cos(p\omega t) \cos((p+1)\omega t) \rangle \tag{3.20}$$

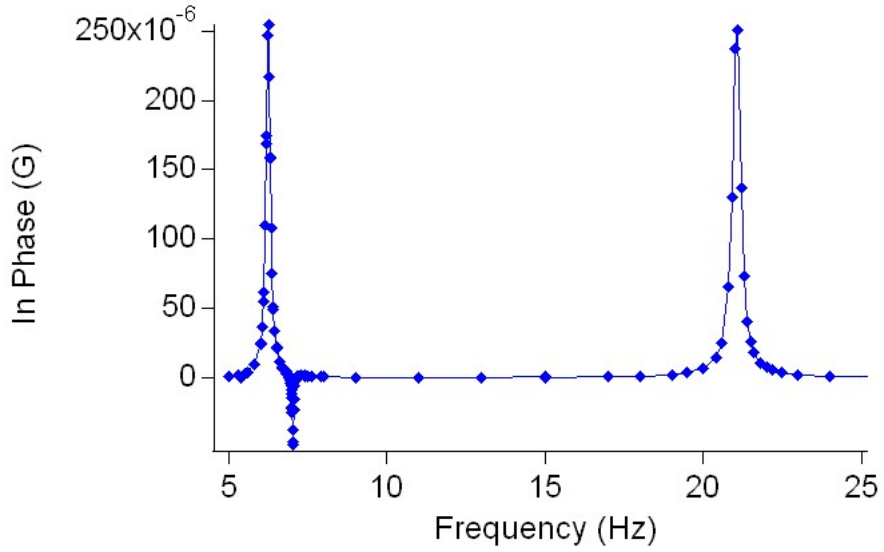

Figure 3.7: When the alkali polarization modulation frequency is scanned starting from the ^{129}Xe resonance at 21Hz down to the ^{131}Xe resonance at 6Hz, a third, inverted resonance peak is seen at 7Hz. This is due to the ^{129}Xe resonance being excited at the thrid harmonic of pump modulation frequency. The proximity of the third subharmonic of ^{129}Xe and the first harmonic of ^{131}Xe allows us to couple the two isotopes.

These time averages must be computed for the each harmonic in order to obtain the correct amplitude ratio between the out of phase and the in phase signals. With first harmonic pumping the ratio $V_{\rm out}/V_{\rm in}$ is 2, while higher harmonics reduce the relative amplitudes.

Extensions to this method are used in pumping two species at the same time and will be discussed in more detail in Chapter 9.

3.4 Upper Limit on Longitudinal Alkali Polarization

This chapter started out by claiming that the importance of successful SSEOP is that it eliminates the alkali field shift from NMR measurements, so it is vital to know by how much we have reduced it. This measurement was done indirectly, for technical reasons that will be described below, by measuring the residual $\hat{z}$ polarization of the alkali. A scan of the Xe resonance is taken monitoring both $\tilde{K}_y$ and S_z; a DC offset in S_z where $\tilde{K}_y$ crosses zero corresponds to non-zero

alkali polarization along the bias field direction, which would cause a shift in the NMR frequency. Using this method at [Rb] = $2.3 \times 10^{13}/\mathrm{cm}^3$we measure $\langle S_z \rangle < 2 \times 10^{-4}$ which is equivalent to an alkali field of 170nG or a frequency shift of 60μ Hz. This is a factor of 2500 reduction from longitudinal NMR. The data is shown in Fig 3.8.

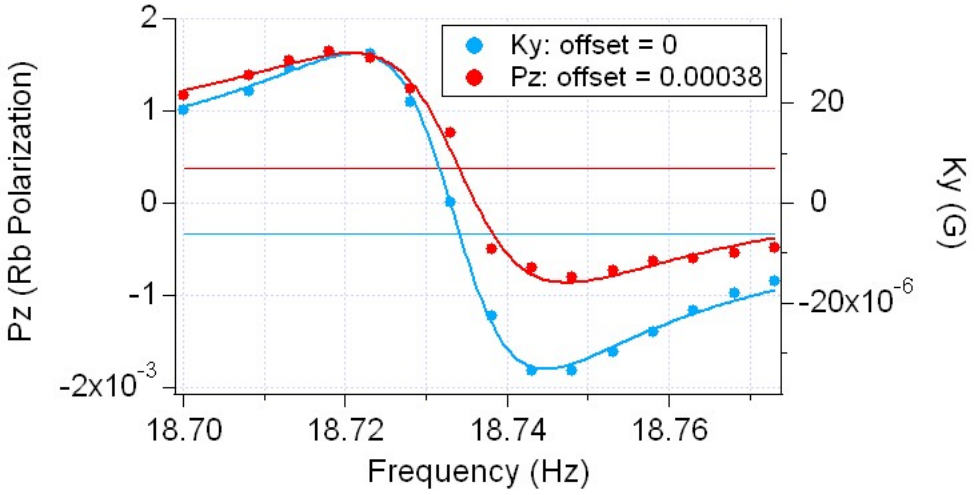

Figure 3.8: The alkali field shift limit is calculated from the DC offset of P_z and is 60μ Hz for this data. This corresponds to a suppresion of 2500 from a longitudinally pumped NMR by $\times 2500$.

3.4.0.1 Failed Methods

The above method is not the most straightforward method of making this measurement. The best way would be to flip B_A and see if there is a frequency shift, but it is not possible to flip the alkali field since it is oscillating at the NMR frequency. We can flip the bias field direction by switching the polarity of the 2π pulses. However, this experiment resulted in a large frequency shift that would correspond to a 30% polarization of the Rb along the bias field direction; the two polarities are shown in Fig. 3.9. We know that the pump, probe, and field coil misalignment is not that bad; therefore, there must be some other effect that is causing such a dramatic change.

Options present themselves as a means of explanation. If the probe is slightly circularly polarized it will cause an AC Stark shift along $\hat{z}$, which exhibits itself as a magnetic field. We would subsequently null out the AC Stark induced shift in the energy levels with a real magnetic field.

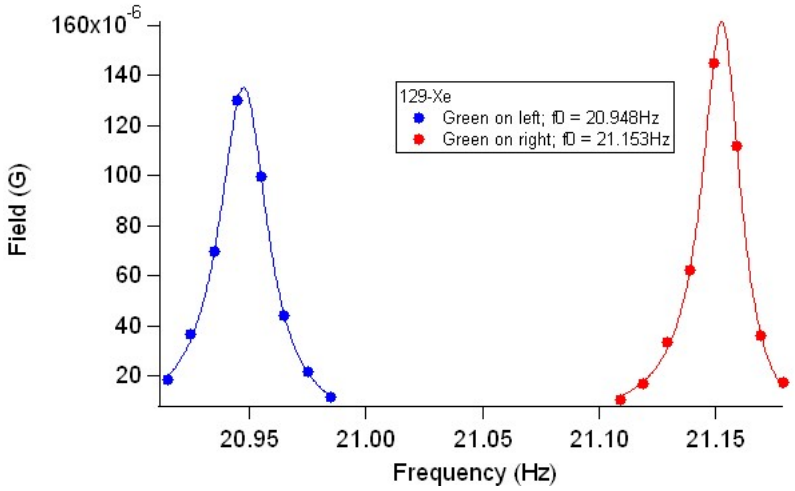

Figure 3.9: Two resonance curves for ^{129}Xe correspond to the two polarities of the 2π pulsing field. The frequency splitting is 0.205Hz.

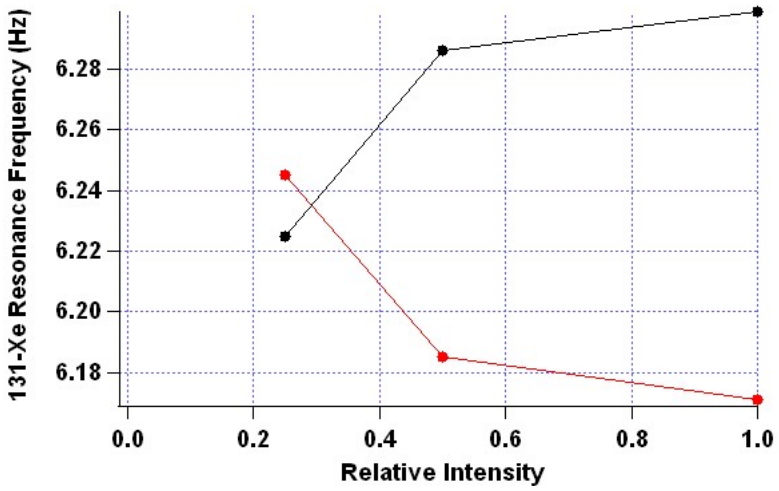

Figure 3.10: The frequency shift between the two polarities of the 2π pulsing field is plotted as a function of probe intensity. If the AC Stark generated by the probe was the sole cause of the frequency shift we see, then the two polarity curves would cross at zero probe intensity. The fact that they do not indicates a residual effect.

Neither the AC Stark shift, that the noble gas does not see, nor the added $\hat{z}$ shim, which the noble gas does see, would change direction as a function of 2π pulse polarity, so it would appear as though the NMR resonance shifts frequency when the bias field is flipped due to the added $\hat{z}$ shim. An experiment that demonstrates this effect is measuring the Xe resonance frequency for the two field polarities as a function of probe intensity. The AC Stark shift decreases as light intensity decreases, so the resonance frequency shift should go to zero at zero probe intensity.The result of this experiment shows in Fig. 3.10 that the two polarities cross as a non-zero probe intensity. The conclusion is that the AC Stark induced by the probe may contribute to some of the frequency shift we see, but not to all of it.

The second is that we are not able to reliably reset the 2π pulse area in such a way that is consistent enough for this experiment. As calculated in Sec. 5.1, we are able to set the 2π pulse area to better than 3 parts in 10000, which corresponds to 4.2mV out of 14V applied 2π pulse voltage. From Sec 7.1.2, we see that a 0.024V change in the 2π pulse voltage results in 1kHz alkali frequency shift. This corresponds to a 1Hz noble gas frequency shift for a 0.032V change in 2π pulse voltage. If we want a factor of 2500 suppression as quoted from the P_z experiment above, we would need to set the 2π pulse voltage to better than 1μV. We are obviously not able to do this with our current setup. It is interesting to note that the precision with which we are able to set the 2π pulses, 4.2mV, corresponds to a 0.125Hz frequency shift in the ^{131}Xe. This is close to what we see. Although it has not been proven, there seems to be reason to believe that this is not the case since the frequency shift was not varying wildly. When these frequency shift measurements were taken, we were not aware of the sensitivity of the resonance frequency to 2π pulse voltage, so it would be worthwhile to look into it more with this in mind.

One piece of evidence that indicates that the alkali field is not causing a significant shift in the NMR frequency is the fact that when we turn on the $\hat{x}$ compensation field, the resonance frequency does not change from uncompensated to fully compensated to < 0.4mHz.

A possible explanation for all this is that we are not able to reliably switch the bias field direction. Likely, there is some coupling of the large pulsed magnetic field to the shield that is exacerbated by the asymmetrical positioning of the cell within the shield. However, we are confident that it is not directly because of any significant alkali polarization along $\hat{z}$.

Chapter 4

NMR Characterization

4.1 Characterization of Xe

In order to gauge the success of our new method of SEOP, we need to first characterize the cell. Most of the experiments performed for this thesis were done in an 8mm "sphere" that is shown in Fig 6.2. This cell contains 32 Torr of ^{129}Xe and 8 Torr of ^{131}Xe. It also has $\approx$ 300 Torr of N_2 as a buffer gas for the ^{85}Rb optical pumping. Since the spin-exchange rate between Xe and Rb is not well known theoretically and depends on composition, the first and most important characterization measurement is that of the spin-exchange rate coefficient. This number dictates the maximum Xe polarization we can attain at a particular alkali density, which allows us to quantify our signals. I present here several methods that all work to varying degrees along with the one that gives satisfactory experimental data as well as a well understood analysis method. We then compare the experimental values to the ones extracted from detailed theoretical modeling. During the course of these measurements we observed in ^{129}Xe an X-factor analogous to that found in ^{3}He in [Babcock, Chann, Walker, Chen, and Gentile, 2006]. The X-factor describes the increase in the wall relaxation rate of the Xe as a function of [Rb] which puts a limit on the maximum attainable polarization.

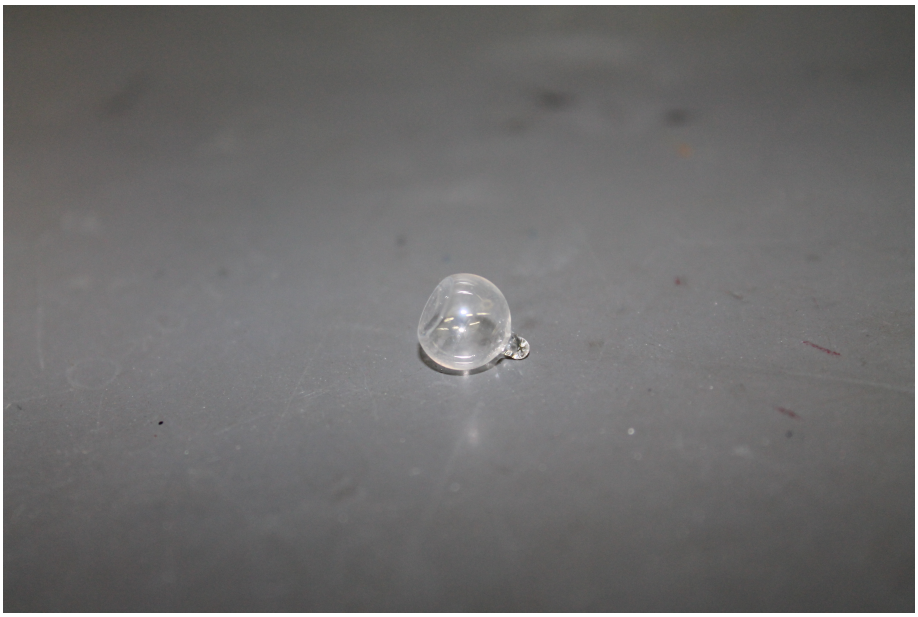

Figure 4.1: This is the cell used for the majority of experiments in this thesis. Its Ehrlenmeyer flask like shape caused the laser beams to be greatly distorted.

4.2 Spin-Exchange Rate Measurement Methods

We tried five different methods for measuring the spin-exchange rate coefficient. I will present these methods and their respective pitfalls and then describe the final method, which is the cleanest measurement of this important characterization. We found the unreliable methods still valuable in that they gave us a better grasp of the system as a whole.

To evaluate how we will measure Γ_{SE}, we start with the basic equation that describes the Xe polarization:

$$P_{\mathrm{Xe}} = \frac{\Gamma_{\mathrm{SE}} P_{\mathrm{Rb}}}{\Gamma_{\mathrm{SE}} + \Gamma_0} \tag{4.1}$$

We have a good handle on P_{Rb} as described in Sec. 6.8.1, so in order to get a measurement of the spin-exchange rate Γ_{SE}, we need to measure the Xe polarization and $\Gamma_1 = \Gamma_{\mathrm{SE}} + \Gamma_0$ where Γ_0 is the fundamental relaxation rate due to the cell and its composition; this includes the wall relaxation rate.

The Xe polarization is found from a calculation of the Xe field:

$$B_{\mathrm{Xe}} = \frac{8\pi g_k}{3\mu_N} \Big(\frac{e\hbar}{2Mc} \Big)^2 \kappa[\mathrm{Xe}] P_{\mathrm{Xe}} \tag{4.2}$$

combined with a calibrated measurement of the Xe field. In the above equation κ is the Fermi contact enhancement factor, P_{Xe} is the Xe polarization, $[\mathrm{Xe}]$ is the Xe density, and M is the proton rest mass. The calibration for the Xe field is done by applying a magnetic field of known amplitude (using the applied voltage, the output resistance, and the coil's current to field conversion) at the Xe resonance frequency along $\hat{y}$. The resulting fake Xe signal's amplitude or, if lock-in detection is used, demodulated signal gives a calibration of signal size in volts to magnetic field. Factors of 2 are easy to miss in this calibration. For example, care must be taken that the numbers being used are amplitudes and not peak to peak values.

4.2.1 DC Pulse Measurement

The first Γ_{SE} method involves a time dependent measurement of the Xe polarization. Theoretically, by turning on the pump or flipping the pump polarization and measuring the buildup of field

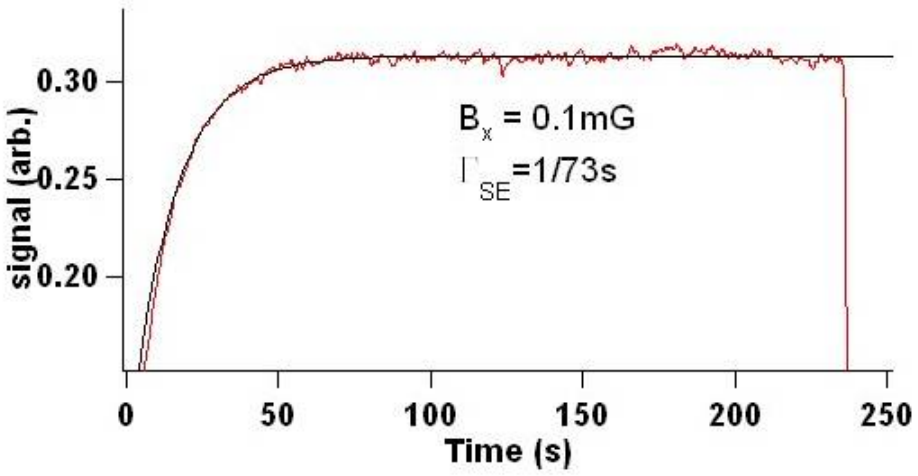

Figure 4.2: The figure shows the data from the attempt at extracting$\Gamma_{\rm SE}$ from the DC pulse method. This set was taken at a low bias field where it is more likely that there is mixing of the two isotopes in the resulting signal.

along $\hat{x}$, we can extract a value for the maximum Xe field at $t = \infty$:

$$P_{\rm Xe}(t) = P_{\rm Xe}(\infty)(1 - \exp[-(\Gamma_{\rm SE} + \Gamma_0)t]) \tag{4.3}$$

and subsequently extract the spin-exchange rate from knowing that the time constant from the buildup gives $\Gamma_{\rm SE} + \Gamma_0 = \Gamma_1$ therefore

$$\Gamma_{\rm SE} = \frac{\Gamma_1 P_{\rm Xe}(\infty)}{P_{\rm Rb}} \tag{4.4}$$

In this measurement, since we expect $\Gamma_{\rm SE}$ to be different for either isotope it is important to separate the two Xe isotopes so that the extracted P_∞ is specific to an individual isotope. We accomplish this by applying a known DC $\hat{x}$ field and a transverse oscillating $\hat{z}$ field at one of the isotopes' resonance frequencies; this tilts that isotope into the transverse plane. The signal when the pump light is turned on contains only one isotope. We measure the buildup of the $\hat{x}$ field by lock-in detection of an applied $\hat{y}$ field. Sample curves are shown in Figs 4.2 and 4.3.

The experiment done at low DC $\hat{x}$ field has a clean buildup of field when the pump turns on, but at this low bias field, the Xe isotopes are not well separated in frequency space. Because of this the

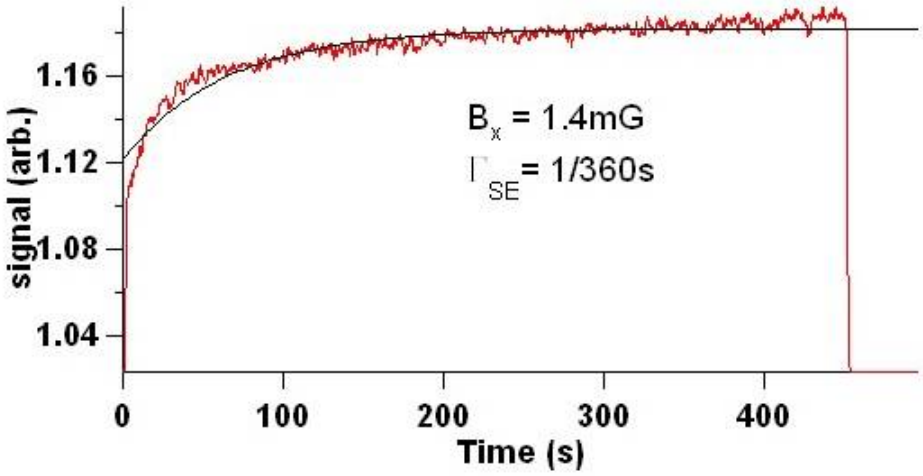

Figure 4.3: This data for the DC pulse method was done at a high bias field where there should be little mixing of the two isotopes in the resulting signal. However, the signal does not follow a clear exponential buildup.

buildup likely contains both isotopes, and without knowing more about the spin-exchange rate for each isotope, we cannot separate the two time constants. As the bias field is increased, however, other unknown issues begin to crop up and the field buildup is no longer a clean exponential. Likely, there is interference in the buildup due to all the competing fields that are applied for separation and detection.

4.2.2 Longitudinal NMR

The second method is a longitudinal NMR measurement in which a bias field is applied along the pump direction $\hat{x}$ and the transverse Xe spin is excited by application of a resonant field perpendicular to the polarization. The tilt of the Xe polarization into $\hat{z}$ is found from the time evolution of the transverse components $P_+ = P_y + iP_z$ on resonance:

$$\frac{dP_+}{dt} = -\Gamma_2 P_+ - i\frac{\Omega_y}{2}P_x \tag{4.5}$$

where $\Omega_y = 2\pi\gamma B_y \cos(\omega t)$. The imaginary portion gives P_z which is the transverse polarization component we detect:

$$P_z = -\frac{\Omega_y P_x}{2\Gamma_2} \tag{4.6}$$

Along the pumping direction:

$$\frac{dP_x}{dt} = -\Gamma_1 P_x + \Gamma_{\mathrm{SE}} P_{Rb} + \frac{\Omega_y P_z}{2} \tag{4.7}$$

In steady state, we obtain

$$P_x = \frac{\Gamma_{\mathrm{SE}} P_{\mathrm{Rb}} + \Omega_y P_z/2}{\Gamma_1} \tag{4.8}$$

Plugging Eqn 4.8 into Eqn 4.6 and rearranging, the resulting transverse polarization as a function of drive field Ω_y is

$$P_z = \frac{-2\Omega_y \Gamma_{\mathrm{SE}} P_{Rb}}{4\Gamma_1\Gamma_2 + \Omega_y^2} \tag{4.9}$$

We can optimize this equation with respect to drive field amplitude to get an expression for Γ_{SE}:

$$\Gamma_{\mathrm{SE}} = \frac{P_{\mathrm{Xe}}}{P_{\mathrm{Rb}}}\sqrt{\Gamma_1\Gamma_2} \tag{4.10}$$

The procedure for this method goes as follows:

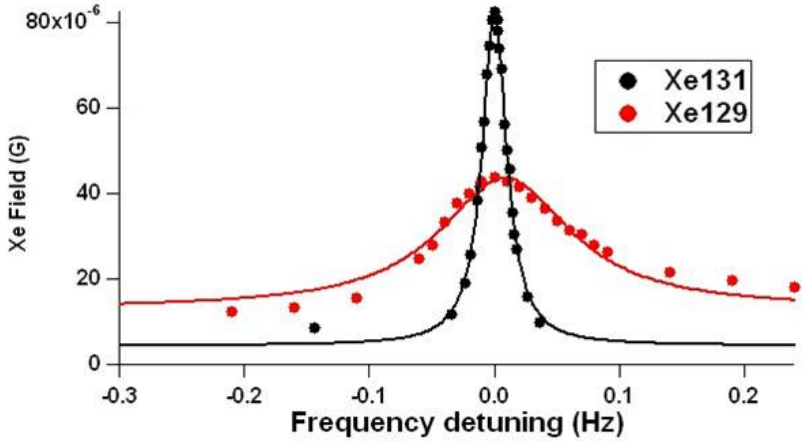

Figure 4.4: Shown are the NMR linewidths for ^{131}Xe and ^{129}Xem which were used in the second method for measuring $\Gamma_{\rm SE}$.

- Apply a large enough B_x to separate the two Xe isotope resonance frequencies
- Apply a sinusoidal B_y at either the ^{129}Xe or ^{131}Xe resonance frequency
- Monitor the response to that frequency
- Scan the frequency to obtain a resonance peak
- Using a calibration for the Xe field, as described in Sec. 4.2, this gives $P_{\rm Xe}$
- Take a series of these measurements as a function of B_y amplitude

This procedure produces well defined resonance peaks for the two isotopes as can be seen in Fig 4.4. Scanning B_y and plotting the amplitude of the resonance curve as a function of applied field amplitude results in Fig 4.5, which can subsequently be fit to Eqn 4.9 to extract $\Gamma_1\Gamma_2$ and $\Gamma_{\rm SE}$.

From the fit to this data, the extracted $\Gamma_{\rm SE} = 0.034/{\rm s}$ and $\Gamma_1\Gamma_2 = 0.062/{\rm s}^2$. In order to double check this method, we need to verify the value for $\Gamma_1\Gamma_2$ and extract a value for Γ_2. If solve for the steady state $\hat{z}$ polarization off resonance:

$$P_z = 2\sqrt{\frac{S_z^2\Gamma_{\rm SE}^2\Omega_d^2}{(4\Gamma_1\Gamma_2+\Omega_d^2)^2+16\Gamma_1(\omega-\Omega_z)^2}} \tag{4.11}$$

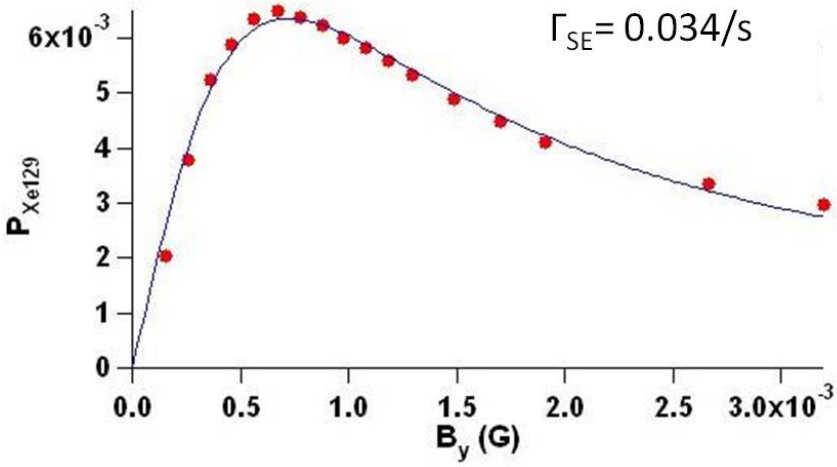

Figure 4.5: In the second method for measuring Γ_{SE} we took data corresponding to the peak Xe polarization (normalized Xe field) as a function of drive field amplitude. This method resulted in a reasonable fit for Γ_{SE}, but failed to agree with subsequent measurements.

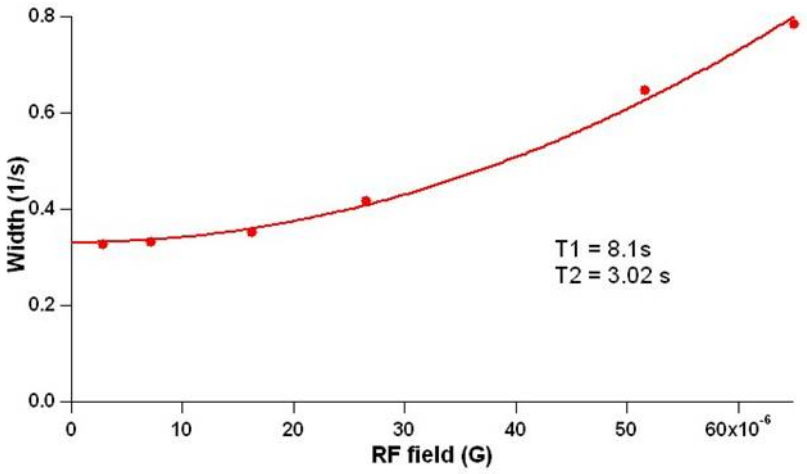

Figure 4.6: A plot of the measured resonance width as a function of drive field amplitude. The extracted values for Γ_1 and Γ_2 and $\Gamma_{\rm SE}$ do not agree with the values obtained from the measurement of Xe polarization as a function of drive field amplitude.

If we define an amplitude A as being $A(4\Gamma_1\Gamma_2+\Omega_d^2) = 2\Omega_d\Gamma_{\rm SE}S_z$ then we can reduce Eqn 4.11 to

$$P_z = \frac{A}{\sqrt{1+\frac{16\Gamma_1^2\Delta^2}{(4\Gamma_1\Gamma_2+\Omega_d^2)^2}}} \tag{4.12}$$

In Eqn 4.12, there is a detuning Δ and we define a width parameter $1/\gamma^2 = \frac{16\Gamma_1^2}{(4\Gamma_1\Gamma_2+\Omega_d^2)^2}$. Now we can use the width of the NMR resonance as a function of drive field amplitude to extract values for Γ_1 and Γ_2 from the parameter γ

$$\gamma = \Gamma_2(1+\frac{\Omega_d^2}{4\Gamma_1\Gamma_2}) \tag{4.13}$$

When we do this, we obtain data and fit as seen in Fig 4.6. There are several issues with the results of this measurement. The first and most prominent is that the $\Gamma_1\Gamma_2 = 0.043/\mathrm{s}^2$ extracted from the above method does not match $\Gamma_1\Gamma_2 = 0.063/\mathrm{s}^2$ extracted from the fit with Eqn 4.9. The second issue is that the NMR lineshapes are asymmetrical revealing that there is something missing in the analysis. Third, the NMR frequency seems to be drifting. I will address the latter two concerns first.

The lineshapes in Fig 4.4 are lopsided and look as though the phase of the lock-in detection is off. The phase of the lock-in is carefully set to zero far off the Xe resonance frequency, but as

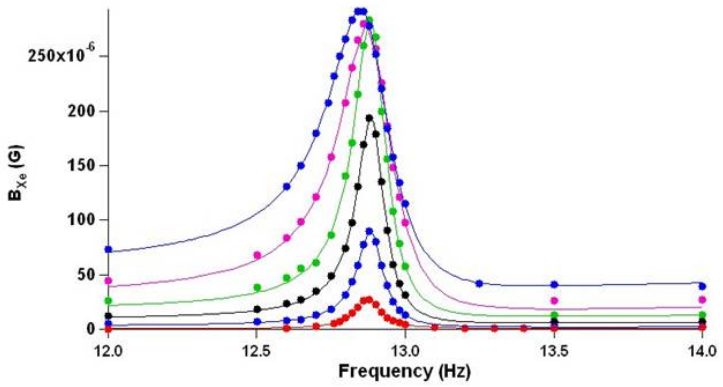

Figure 4.7: The NMR peaks are aymmetrical due the Xe phase changing as resonance is scanned. The different colors correspond to different drive field amplitudes

the frequency is scanned, the phase of the Xe changes with respect to the Rb thus distorting the lineshape. If we then return to the equation for the transverse spin components and introduce a phase dependence $K_+ = K_\perp e^{i\omega t}$ and then translate back to K_+ we obtain

$$K_+ = \frac{2\Omega_d \Gamma_{\mathrm{SE}} S}{4i\Delta\Gamma_1 + 4\Gamma_1\Gamma_2 + \Omega_d^2} e^{-i\omega t} \tag{4.14}$$

Using the same definition for A,

$$K_+ = A \frac{\cos\alpha - \frac{\Delta \sin\alpha}{\gamma}}{1 + \frac{\Delta^2}{\gamma^2}} \tag{4.15}$$

where we now have the parameter α that accounts for the phase of the Xe as resonance is scanned. This accounts for the skewed lineshapes and the apparent resonance frequency shift as seen in Fig 4.7.

Of the first concern, we never came to a definitive conclusion as to why the values for Γ_1 and Γ_2 never align with each other, but hypothesized that because the theory analyzing the NMR behavior is complex, that we are still missing a piece. As subsequent studies revealed, this piece may have been an alkali field issue. The theory also becomes more complicated when using ^{131}Xe, which has a nulcear spin of 3/2. Because of both of these factors, we abandoned this method in search of one that is more straight forward.

4.2.3 Γ_1 Measurement Procedure

In conjunction with the above procedure, we worked on a separate method to measure Γ_1. If we were to use this method to extract a value for Γ_{SE}, we would need to combine it with NMR linewidth measurements to obtain Γ_2 and B_{Xe}. However, this method runs into the same problem as described above in that we do not understand the NMR lineshapes well enough to extract meaningful results for Γ_2 and Γ_{SE}, but it is a straight forward way to measure Γ_1.

The procedure goes as follows:

- Polarize all atoms along the $\hat{x}$ direction with an applied bias field to separate the two isotope frequencies
- Turn off the pumping for time τ
- Turn the pump light back on and apply to one of the isotopes a transverse resonant RF pulse
- Measure the Xe signal amplitude after the pulse as a function of τ, the time the pump is off

The data and fits for Γ_1 of both isotopes can be seen in Figures 4.8 and 4.9. Care must be taken to ensure that the time the pump is turned on is sufficiently long so that the Xe is fully polarized when the pump is once again blocked.

4.2.4 π Pulse Method

In order to free the spin-exchange rate measurement from the complications due to the NMR linewidths, we settled on a separate experiment in which we once again apply a bias field large enough to separate the isotope frequencies. An RF pulse is applied along a transverse direction to flip one of the isotopes π radians. The time constant of the field buildup along the $\hat{x}$ direction, measured by lock-in detection of the response to an oscillating B_y, will give us Γ_1 and the Xe field can be extracted from the peak value of the signal that results from the pulse. This is similar to the first method, but we are using the RF field to excite the isotope we want to measure.

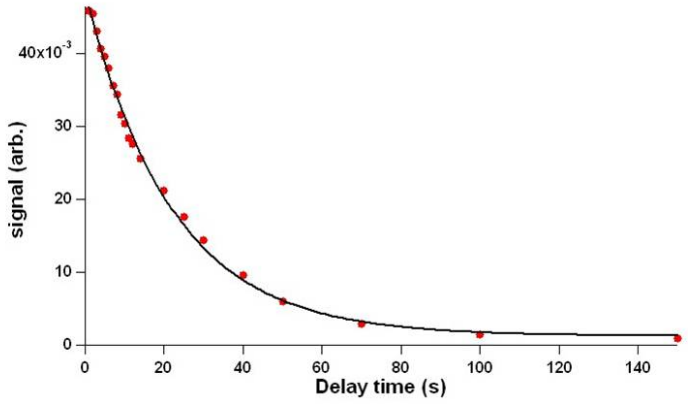

Figure 4.8: The Xe field as a function of time the pump is turned off results in $\Gamma_1 = 1/22$s for ^{129}Xe at this particular density of 2×10^{13}.

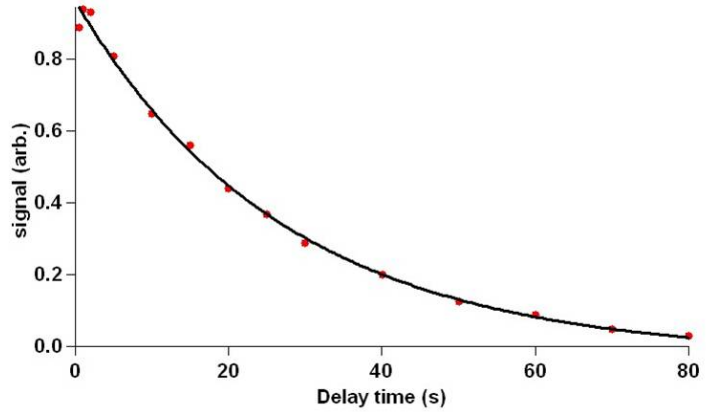

Figure 4.9: The ^{131}Xe data taken at the same density as Fig 4.8 results in $\Gamma_1 = 1/27$s for ^{131}Xe at [Rb]$\approx 2 \times 10^{13}$.

In this new method, we have eliminated the need for a Γ_2 measurement. Previously, when using the NMR method, we get $\Gamma_{\rm SE}$ from

$$\Gamma_{\rm SE} = \frac{P_{Xe}}{P_{Rb}} 2\sqrt{\Gamma_1 \Gamma_2} \tag{4.16}$$

Now when the resonant drive field is eliminated, we have no transverse relaxation contribution and the spin-exchange rate is simply:

$$\Gamma_{\rm SE} = \frac{P_{Xe}}{P_{Rb}} \Gamma_1 \tag{4.17}$$

where the Xe polarization is obtained from the ratio of the measured Xe field to the calculated maximum field produced by the total amount of Xe in the cell: $P_{\rm Xe} = B_{\rm Xe}/B_{\rm Xe,100}$. $P_{\rm Rb}$ is measured in the usual way described in Sec 6.8.1. The peak Xe field is extracted from the peak of the curve and Γ_1 is extracted from the time constant. Doing these measurements at a few different densities gives Fig 4.10 from which a spin-exchange rate coefficient of $\kappa = 3.28 \times 10^{-16} {\rm cm}^3/{\rm s}$ is found.

There are a couple of issues with this method that throw doubt on the result. One of these is the introduction of the wrong isotope into the signal since when the π pulse is not perfectly tuned, it is easy to introduce signal from the wrong isotope. Separating the two isotopes once again proves to be difficult because of similar behavior as was seen in the first method; as the bias field increases, the signal size decreases. Although we are unsure of the origin, this behavior may be because the magnetometer sensitivity gets smaller with an added field of around 1-2 mG or the fields are complicating the alkali rotation as discussed with the first method. We ended up operating where the signal maximizes. Pulse shape considerations are important to consider as well. Any DC offset or "tail" to the applied RF pulse results in mixing the isotope signals. This was a particularly difficult issue when measuring ^{131}Xe. If there was any imperfection in the RF pulse applied to excite ^{131}Xe, ^{129}Xe was very easily excited as well since it is so much more sensitive to fields.

The other main concern with this measurement comes from the fact that at low density the π pulse measurement has very poor signal to noise, so it is difficult to obtain a consistent peak field and Γ_1 measurement. There are a several options for how this noise is introduced. The simplest

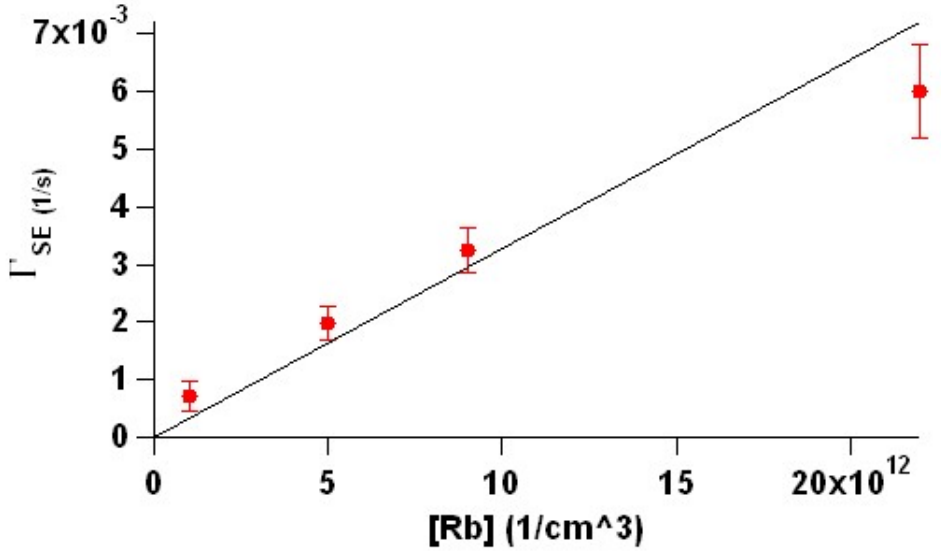

Figure 4.10: The spin exchange rate as measured by the π pulse method is plotted as a function of density. This method results in $\kappa_{\mathrm{SE}} = 3.28 \times 10^{-16}\mathrm{cm}^3/\mathrm{s}$, which, despite the noise troubles, is in good agreement with the final method.

solution is a noisy B_x shim, but switching the B_x shim driver to a very stable laser current source shows no difference.

A more complicated, but still viable option is a noisy AC Stark shift, i.e. pump intensity and frequency noise, which would also increase $\hat{x}$ field noise. In order to evaluate this issue, we measured the field noise that would be created by pump intensity and frequency fluctuations to see if they have substantial contributions to the noise level we see. To obtain a calibration of pump intensity or pump frequency to B_x, we monitor the change in B_x as a function of either relative intensity or pump frequency. With this information, we can then convert the measured pump intensity or frequency fluctuations to magnetic field fluctuations. Pump intensity is monitored via far off resonance pump transmission. The most sensitive measurement of pump frequency is monitoring the pump transmission halfway down the absorption spectrum. The results of these tests show that pump intensity fluctuations are too small to account for the field noise, but pump frequency fluctuations may contribute. This path was not pursued any further due to the success of the next Γ_{SE} method.

Something to note is that there is a difference in the frequency noise between the two laser drivers. We are using a Thorlabs driver for one laser and an SRS driver for the other. The SRS controller has high frequency components, while the Thorlabs controller does not. We never switched the controllers to see if this behavior was controller or laser dependent, but it is something to keep in mind for potential future questions. We never resolved the B_x noise issue since we moved on to the final Γ_{SE} method.

4.2.5 The Reliable Spin-Exchange Rate Measurement and Accompanying Experiments

The beauty of this method of measuring Γ_{SE} is that we can do a simultaneous measurement of both isotopes. The process is to polarize all the Xe along $\hat{x}$ with an applied B_x quantization field for a time τ then hit the Xe with a strong DC pulse along $\hat{y}$. The two Xe isotopes will then precess in the $\hat{x}$ -$\hat{z}$ plane about B_y with their respective characteristic frequencies. The resulting signal

follows

$$\text{sig} = B_{129}\sin(2\pi f_{129}t) + B_{131}\sin(2\pi f_{131}t) \tag{4.18}$$

The fit will result in the respective frequencies and field amplitudes for the two isotopes at time τ. After the measurement is taken, the pump light is turned off long enough so that the Xe is completely depolarized. A series of these measurements are then taken as a function of τ to extract a rise time corresponding to Γ_1 and a maximum value for $P_{\text{Xe}}(\infty)$ for each isotope.

A couple of things are important to be wary of for this experiment to work properly. The first is that the time the pump is off must be sufficiently long so as to ensure that the Xe is completely depolarized before the next pulse is applied. The second is the timing of the $\hat{x}$ bias and $\hat{y}$ pulsing fields. As we increase the $\hat{x}$ quantization field, we expect the measured Xe field to level off. This is because B_x helps to define the pumping axis, which allows for a more stable Xe polarization along that single axis. When using the two large fields that are perpendicular ($\hat{x}$ quantization and $\hat{y}$ pulsing), it is crucial that the $\hat{x}$ bias field is turned off when the $\hat{y}$ DC pulse is applied so that the axis about which the Xe precesses is clearly defined. If there is a time delay in simultaneously triggering off B_x and turning on the B_y pulse, the two fields will overlap. This small (70ms) timing error accounts for the Xe field falling off at higher bias fields; once it is resolved we obtain the green dashed curve in Fig 4.11 and Fig 4.11b instead of the solid black line. The ^{129}Xe still drops off a little at the very high bias fields, but there may still be a residual triggering issue to which the ^{129}Xe is more susceptible.

Calibrating the fields correctly is also vitally important. The measurement being made is P_y

$$P_y = \frac{\Omega_z R_x + \Omega_y \Omega_x R_x/\Gamma'}{\Omega_y^2 + \Gamma'^2} \tag{4.19}$$

which gives sensitivity to both B_x and B_z

$$P_y = \frac{R_x}{\Omega_y}\left(\frac{\Omega_z}{\Omega_y} + \frac{\Omega_x}{\Gamma'}\right) \tag{4.20}$$

Assuming $\Omega_y >> \Gamma'$, the sensitive field is Ω_x even though Ω_z will also respond since the DC pulse is along $\hat{y}$. The ratio of Ω_x/Ω_z for the measurements I was taking is 20; if they were much closer, it would be necessary to do a more complicated form of calibration.

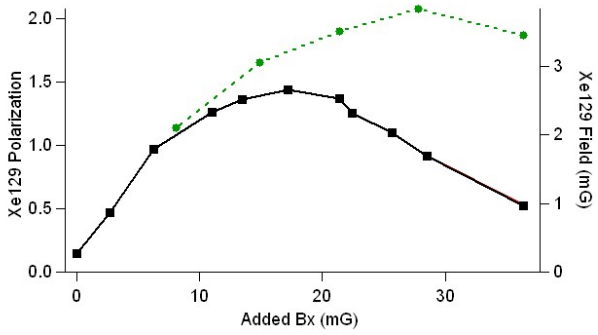

(a) Xe field as a function of B_x for ^{129}Xe.

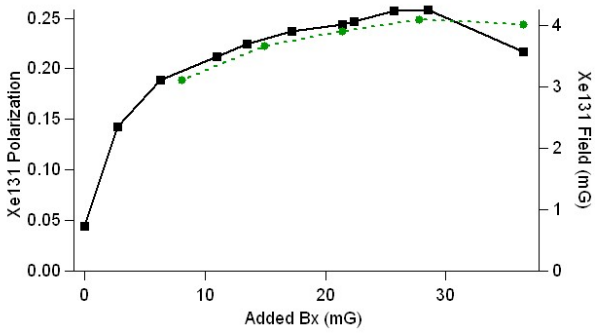

(b) Xe field as a function of B_x for ^{131}Xe.

Figure 4.11: The Xe field is plotted as a function of applied B_x. We found that due to a timing issue in how we made the measurement the Xe field would fall off at high B_x. The green trace is with the timing issue resolved and the black is with it unresolved. As quantization field along the pumping direction is added, the Xe field size should increase and level off at the max field value. This is because the quantization field helps to define the pumping axis allowing a more stable Xe polarization along that single axis.

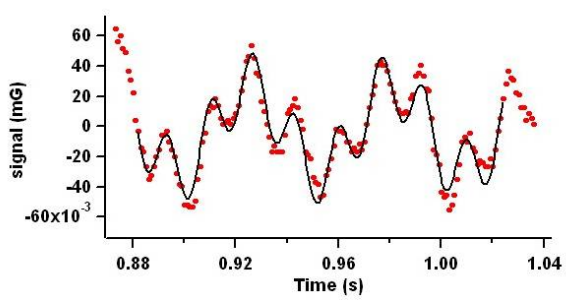

(a)

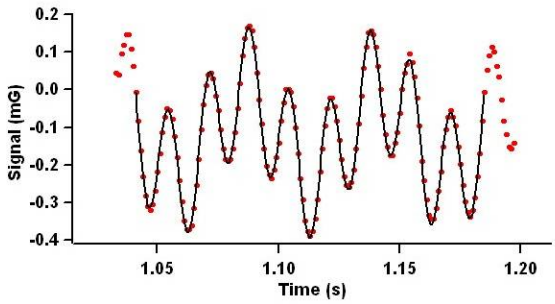

(b)

Figure 4.12: Xe signals from the Γ_{SE} measurement. (a) is the measurement done for short pumping time and (b) is the measurement done for long pumping times. These curves are fit to a sum of two sine waves to extract the size of the Xe field as a function of pumping time.

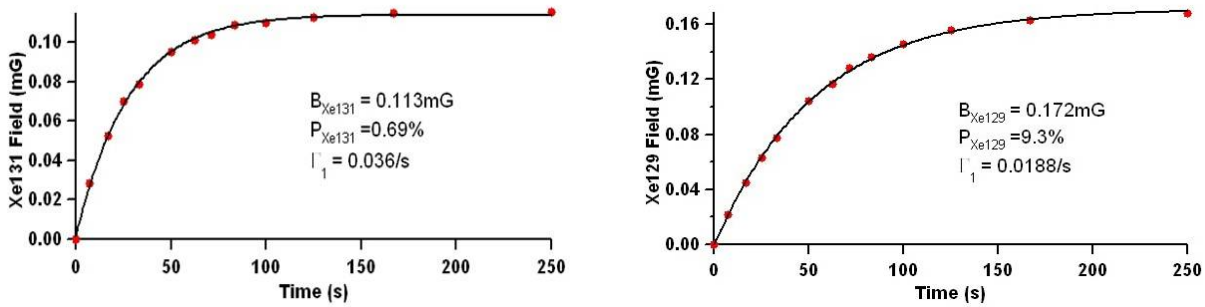

(a) Γ_1 for ^{131}Xe

(b) Γ_1 for ^{129}Xe

Figure 4.13: The measurement for T_1 comes from the fit of the Xe signal as a function of pumping time. The maximum Xe field is also extracted from this curve.

With the quantization axis defined by B_x and the field behavior understood, the Γ_1 measurement proceeds smoothly. The Xe rotation data is shown in Fig 4.12a and 4.12b for short and long pumping times. The resulting field buildup is seen in Figs 4.13a and 4.13b. These measurements are done at several different densities and the spin-exchange rate as a function of density is shown in Figs 4.14a and 4.14b. The spin exchange rate coefficient can then be extracted from the measured Γ_1 and P_{Xe} via:

$$\Gamma_{\mathrm{SE}} = \frac{P_{\mathrm{Xe}}}{P_{\mathrm{Rb}}}\Gamma_1 \tag{4.21}$$

One simple way to check if the rates are near what is expected is to compare the ^{131}Xe to the ^{129}Xe spin-exchange rate. We start with the van der Waals molecule contribution to the spin exchange rate:

$$\Gamma_{\mathrm{SE}} = \frac{1}{2T_x}(\frac{\alpha\tau}{\hbar})^2 \tag{4.22}$$

where T_x is the molecular formation rate and τ is the molecular breakup rate and α is the interaction strength. We know that the molecular formation rate must be the same as the molecular breakup rate:

$$\frac{[\mathrm{Xe}]}{T_x} = \frac{[\mathrm{RbXe}]}{\tau} = \frac{\kappa_{\mathrm{chem}}[\mathrm{Xe}]}{\tau} \tag{4.23}$$

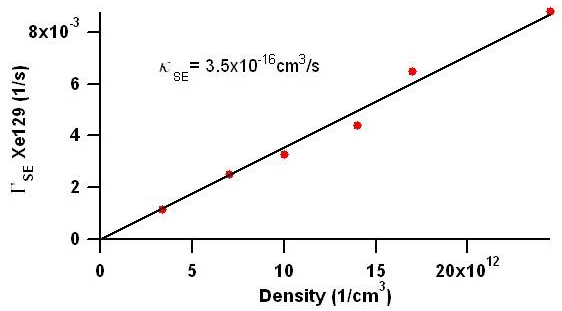

(a) The spin exchange rate coefficient for ^{129}Xe

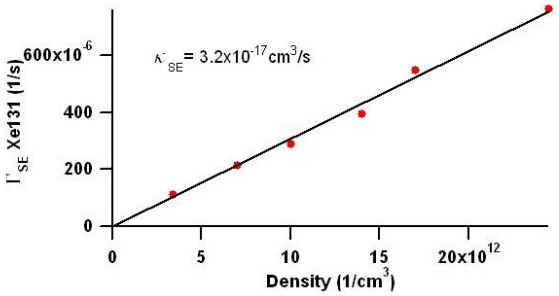

(b) The spin exchange rate coefficient for ^{131}Xe

Figure 4.14: The spin exchange rate is plotted as a function of density.

then

$$\frac{1}{T_x} = \frac{\kappa_{\rm chem}[\rm Rb]}{\tau} \tag{4.24}$$

which will give

$$\Gamma_{\rm SE} = \frac{\kappa_{\rm chem}[\rm Rb]}{2}\frac{\alpha^2\tau}{\hbar^2} \tag{4.25}$$

The interaction strength α is proportional to the gyromagnetic ratio, so the ratio of the Xe spin exchange rates should be proportional to the square of the gyromagnetic ratios:

$$\frac{\Gamma_{\rm SE}(131)}{\Gamma_{\rm SE}(129)} = \left(\frac{\gamma_{131}}{\gamma_{129}}\right)^2 = \frac{1}{11.4} \tag{4.26}$$

We then need to use our measure quantities Γ_1 and $P_{\rm Xe}$

$$\Gamma_{\rm SE}(131) = \frac{3}{5}\frac{P_{131}}{P_{\rm Rb}}\Gamma_1(131) \tag{4.27}$$

and

$$\Gamma_{\rm SE}(129) = \frac{P_{129}}{P_{\rm Rb}}\Gamma_1(129) \tag{4.28}$$

gives

$$\frac{\Gamma_{\rm SE}(131)}{\Gamma_{\rm SE}(129)} = \frac{3/5P_{131}}{P_{129}}\frac{\Gamma_1(131)}{\Gamma_2(129)} \tag{4.29}$$

The factor of 3/5 comes from the fact that

$$P_K = \frac{\langle K_z\rangle}{K} = \frac{\epsilon(P)}{2K}P_S\frac{\Gamma_{\rm SE}}{\Gamma_1} \tag{4.30}$$

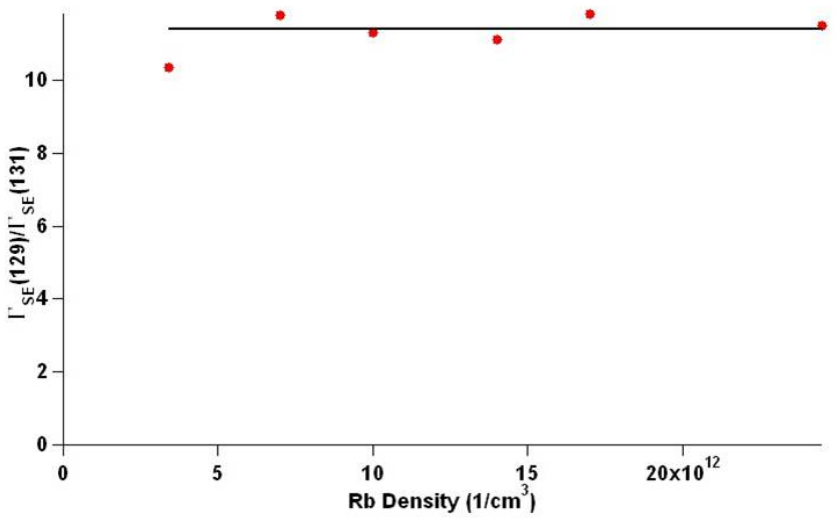

Figure 4.15: This is a comparison of the ratio of the spin exchange rate at different densities for ^{129}Xe and ^{131}Xe. Theoretical analysis says that this ratio should be 11.4, which is the black line in the figure.

where $\epsilon(P_K)$ is the slowing down factor, which is ≈ 5 at intermediate polarizations and $K = 3/2$ for ^{87}Rb. Taking our measurements for we obtain a result for the ratio of the two spin exchange rates that is consistent with 11.4 at each of the densities as seen in Fig4.15.

If we then combine the spin exchange rate from van der Waals molecules with the binary spin exchange rate we get an expression for the spin exchange rate coefficient:

$$\kappa_{\mathrm{SE}} = \kappa_{\mathrm{binary}} + \frac{\kappa_{\mathrm{chem}}}{2}\frac{\alpha^2\tau}{\hbar^2} \tag{4.31}$$

The full calculation is a little tricky because the different lifetimes of the van der Waals molecules account for different rates of exchange and must be accounted for accordingly. The literature is also lacking a consensus for κ_{chem}. Nevertheless, the resulting calculation agrees with the measured spin exchange rate coefficient. Using the values from literature for $\alpha = 29$MHz [Bhaskar, Happer, and McClelland, 1982] and [Bhaskar, Happer, Larsson, and Zeng, 1983] and $\kappa_{\mathrm{chem}} = 213$ [Nelson and Walker, 2001] and $\kappa_{\mathrm{binary}} = 1.75 \times 10^{-16}\mathrm{cm}^3/\mathrm{s}$ [Jau, Kuzma, and Happer, 2002], we obtain for ^{129}Xe the calculated coefficient is $\kappa_{\mathrm{SE}} = 3.84 \times 10^{-16}\mathrm{cm}^3/\mathrm{s}$ and the measured is $\kappa_{\mathrm{SE}} = 3.5 \times 10^{-16}\mathrm{cm}^3/\mathrm{s}$. For ^{131}Xe, since the calculation is much more complex due to its being

a spin-3/2 particle, we simply divide the above calculated value for ^{129}Xe by 11.4 and obtain the calculated coefficient is $\kappa_{\rm SE} = 3.37 \times 10^{-17}{\rm cm}^3/{\rm s}$ and the measured is $\kappa_{\rm SE} = 3.2 \times 10^{-17}{\rm cm}^3/{\rm s}$.

4.3 X-Factor

During the course of making the measurement for $\Gamma_{\rm SE}$, we discovered a phenomenon that has previously been studied in ^{3}He [Babcock et al., 2006] called the X factor. This is manifested in the fact that we see a density dependence of the wall relaxation rate shown in Fig 4.16. The cause of this phenomenon is unknown, but it is substantially less for ^{131}Xe as is seen in Fig4.17. The wall relaxation rate is measured by taking the measured $\Gamma_1 = \Gamma_{\rm SE} + \Gamma_{\rm wall}$ and subtracting $\Gamma_{\rm SE}$ from it.

The most important manifestation of the effect of the X factor is the limit it puts on the Xe polarization. Without the X factor, the Xe polarization can approach the Rb polarization as the density is increased:

$$P_{Xe} = \frac{\kappa_{SE} n P_{Rb}}{\kappa_{SE} n + \Gamma_{\rm wall}} \rightarrow P_{Rb} \tag{4.32}$$

When the X factor is added to the wall relaxation rate such that $\Gamma_{\rm wall,meas} = \kappa_{SE} n X + \Gamma_{0,\rm wall}$ the Xe polarization is limited to

$$P_{Xe} = \frac{\kappa_{SE} n P_{Rb}}{\kappa_{SE} n (1+X) + \Gamma_{0,\rm wall}} \rightarrow \frac{P_{Rb}}{1+X} \tag{4.33}$$

This behavior is seen when the ratio of Xe polarization to Rb polarization is plotted as a function of density. Fitting the data to Eqn 4.32 gives the fit in Fig 4.18a while fitting it to Eqn 4.33 of Fig 4.18b.

The fit from the data gives an X-factor of 3.4 which limits the ^{129}Xe polarization to $0.225 P_{\rm Rb}$. We had hoped that by increasing [Rb] we would be able to increase the Xe polarization universally, but for ^{129}Xe, this is not the case; we are close to maximum polarization at a few $\times 10^{13}$/cm^3. This might be an inhibiting factor in the argument for using cells with lower Xe density as presented in Sec. 8.1.

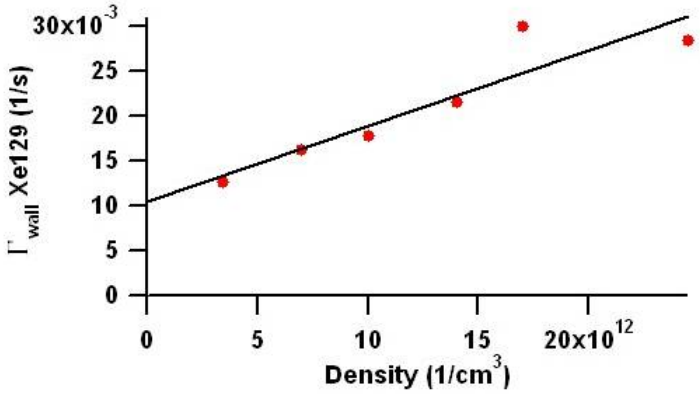

Figure 4.16: The wall relaxation rate for ^{129}Xe is plotted against density.

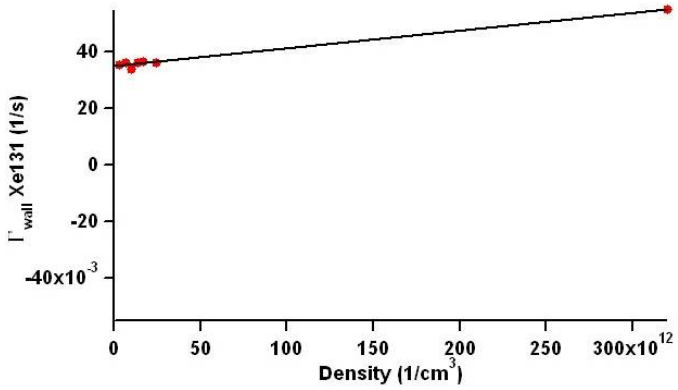

Figure 4.17: The wall relaxation rate for ^{131}Xe is plotted against density. There is very little dependence which means that the X-factor for this isotope is negligible.

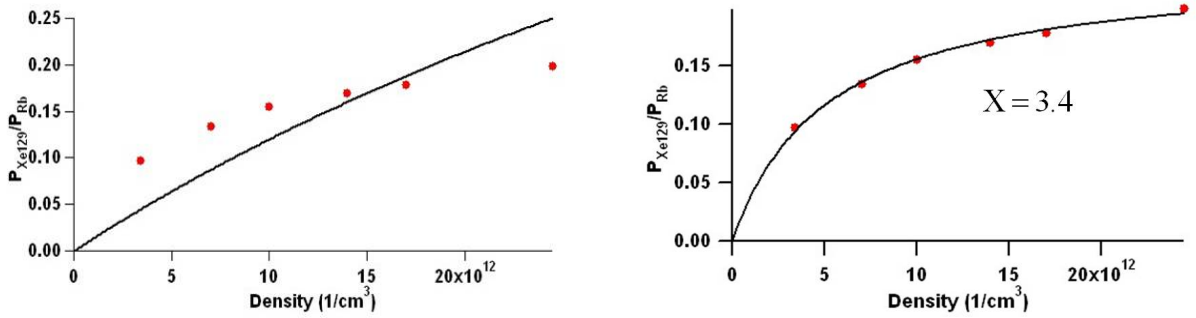

(a) Poor fit without x factor

(b) Good fit with x factor

Figure 4.18: These are plots of the ratio of ^{129}Xe polarization to Rb polarization as a function of density. Since the X-factor dictates the fraction of alkali polarization can be imparted to the Xe nuclei, looking at this fraction as a function of density reveals the maximum attainable polarization. The figure on the right shows the ratio of Xe polarization to Rb polarization and the black fit does not fold in the X-factor. The figure on the right shows the same data with a fit that folds in the X-factor. An X-factor of 3.4 is extracted which limits the Xe polarization to 22.5% of the Rb polarization.

The exploration of the X-factor is something we did not pursue in my tenure here, but it is a simple experiment that could easily be fleshed out using our lower denisity Xe cells.

Chapter 5

Noise Measurements

The sensitivity of any device is limited by its noise floor, so it is vital to know this boundary and reduce it as much as possible, but at some point, fundamental noise levels are hit and the noise cannot be lowered any further. All of the noise measurements we make naturally lead to figures of merit for the applications of the NMR oscillator. In the first part of this chapeter, I will make projections for angle random walk (ARW) and bias stability. These projections are based on noise levels we have measured in the lab, as well as levels we believe are reasonably attainable. As I will point out, they all assume successful dual species operation.

The second part of the chapter discusses noise studies of the PPR magnetometer. These studies were made to determine the best operating parameters for probe laser detuning and direction, 2π pulse settings, and parametric modulation schemes. I will step through each of these and how they change the noise characteristics.

5.1 Noise Projections for Dual Species Pumping

The frequency noise for an NMR oscillator has two main contributions:

$$\delta\dot{\phi} = \gamma\delta B_z + \frac{\delta\phi}{2\pi T_2} \tag{5.1}$$

where δB_z is the noise in the bias field, T_2 is the transverse relaxation time, and $\delta\phi$ is the noise in the phase between the NMR drive (the alkali polarization modulation) and the spin precession, which can be re-written as $\delta\phi = (\mathrm{SNR})^{-1} = \delta B_y / B_{\mathrm{Xe}}$ so that

$$\delta\dot{\phi} = \gamma\delta B_z + \frac{1}{2\pi T_2}\frac{\delta B_y}{B_{\mathrm{Xe}}} \tag{5.2}$$

In dual species operation, δB_z can be stabilized using one of the isotopes, while the measurement is taken with the other. The precession frequency of one species is:

$$f_1 = \gamma_1(B_z + \delta B_z) + \frac{1}{2\pi T_{2,1}}\frac{\delta B_{y1}}{B_{\mathrm{Xe1}}} + X_1 \tag{5.3}$$

where we have introduced X_1 which is the parameter we are interested in measuring. The other noble gas species has frequency:

$$f_2 = \gamma_2(B_z + \delta B_z) + \frac{1}{2\pi T_{2,2}}\frac{\delta B_{y2}}{B_{\mathrm{Xe2}}} + X_2 \tag{5.4}$$

We can now lock one isotope's frequency to a sub-multiple of a clock at frequency f_c, so that

$$B_z + \delta B_z = \Big(f_c - x_1 - \frac{\Gamma_{2,1}\delta B_{y,1}}{2\pi B_{\mathrm{Xe1}}}\Big)\frac{2\pi}{\gamma_1} \tag{5.5}$$

Then f_2 is independent of $B_z + \delta B_z$

$$f_2 = \frac{\gamma_2}{\gamma_1}f_c + X_2 - \frac{\gamma_2}{\gamma_1}X_1 + \frac{\Gamma_{2,2}\delta B_{y,2}}{2\pi B_{\mathrm{Xe2}}} - \frac{\gamma_2}{\gamma_1}\frac{\Gamma_{2,1}\delta B_{y,1}}{2\pi B_{\mathrm{Xe1}}} \tag{5.6}$$

and in terms of X_1 and X_2

$$-X_1 + \frac{\gamma_2}{\gamma_1}X_2 = \mathcal{X} = \frac{\gamma_2}{\gamma_1}f_c - f_2 + \frac{\Gamma_{2,2}\delta B_{y,2}}{2\pi B_{\mathrm{Xe2}}} - \frac{\gamma_2}{\gamma_1}\frac{\Gamma_2\delta B_{y,1}}{2\pi B_{\mathrm{Xe1}}} \tag{5.7}$$

If we then add the noise terms in quadrature and assume that $\delta B_{y,1}^2 \approx \delta B_{y,2}^2$, $B_{\mathrm{Xe1}} \approx B_{\mathrm{Xe2}}$, and $\Gamma_{2,1} \approx \Gamma_{2,2}$, we find the noise associated with the measured parameter $\mathcal{X}$:

$$\delta\mathcal{X} = \Big(1 + \frac{\gamma_2^2}{\gamma_1^2}\Big)^{1/2}\Big(\frac{\Gamma_2\delta B_y}{2\pi B_{\mathrm{Xe}}}\Big) \tag{5.8}$$

If we use the numbers we have measured for $\delta B_z = 2\mathrm{nG}/\sqrt{\mathrm{Hz}}$, $\delta B_y = 2\mathrm{nG}/\sqrt{\mathrm{Hz}}$, $\delta\nu = 10$ mHz, and $B_{\mathrm{Xe}} = 180\mu$G, the noise, as calculated with Eqn 5.8, without dual species stabilization is 700 nHz/$\sqrt{\mathrm{Hz}}$ and with stabilization it is 100 nHz/$\sqrt{\mathrm{Hz}}$. This means that using dual species will reduce the total noise by a factor of 8.

One limit to the magnetic noise levels we measure is the photon shot noise. This is the noise inherent to the detection due to the fact that photons are discrete particles. The limit is given by:

$$\delta\theta = \frac{1}{2}\sqrt{\frac{e}{I}} \tag{5.9}$$

where θ is the rotation angle of the probe light polarization. The rotation of the light results in a current, so the shot noise in terms of photocurrent is:

$$\delta I = \sqrt{2eI_{\mathrm{tot}}} \tag{5.10}$$

In measurements of the shot noise, one must be careful to measure the actual photocurrent, not just the power of the light hitting the photodiodes.

We can compare this measured shot noise limit to the theoretical value calculated in [Budker and Kimball, 2013]:

$$\mathrm{SN} = \frac{\Gamma'}{\pi\gamma_S}\sqrt{\frac{2}{\eta\Phi\mathrm{OD}_0}} \tag{5.11}$$

where we have also folded in the magnetometer response to change it to field units. All the parameters in the above equation are measureable quantities, or are known constants. The on-resonance optical depth $\mathrm{OD}_0 = n\sigma_0$ with σ_0 being the on resonance cross section, Φ is the photon flux, η is the detector efficiency, Γ' is the measured magnetometer relaxation rate, and $\gamma_S \approx \mu_B/3\hbar$. We can use our measured shot noise limit to calculate the shot noise limited performance of the oscillator.

Putting in measured numbers, the shot noise level is $\delta B_y = 0.13\mathrm{nG}/\sqrt{\mathrm{Hz}}$, giving $\delta\mathcal{X} = 10\mathrm{nHz}/\sqrt{\mathrm{Hz}}$, which is almost a factor of 10 better than the Romalis co-magnetometer of Ref. [Kornack et al., 2005]. We are not currently at this limit for DC detection mostly due to technical noise on the probe and poor shielding. We believe these technical issues can be overcome by some of the improvements to our setup that have been mentioned throughout this thesis.

The second figure of merit is the bias stability which defines the long term drift of the NMR gyroscope. In Chapter 3, it was shown that the residual alkali field shift is 60μHz for single species operation. When dual species Xe NMR is implemented, this frequency shift will reduce by the differential alkali field that was discovered in [Bulatowicz et al., 2013] resulting in a 120nHz alkali

field shift. The bias stability of the oscillator will then be determined by drifts in the system (such as alkali polarization) about this number.

An Allan deviation measurement determines the bias stability by measuring the frequency deviation over a long integration period. In this analysis, the long time series $\mathrm{noise} = y(t)$ of length T is divided into $n = T/\tau$ time segments where τ is the averaging time. The average value of the signal $\bar{y}_i$ is computed for each of those segments then the square of the difference between two consecutive bins is taken and summed over all the time segments. The Allan variance for that particular integration time τ is then:

$$\sigma^2 = \frac{1}{2(n-1)} \sum_{i=0}^{n-1} \left(\bar{y}_{i+1} - \bar{y}_i \right)^2 \tag{5.12}$$

The square root of σ is the Allan deviation. Ideally, when the deviation is computed for increasing averaging times it will decrease to a minimum value, where the initial decrease reflects the ARW and the minimum corresponds to the bias stability. At some point the $1/f$ noise that is inherent to the system dominates and the stability measurement increases.

The projected Allan deviation for our setup follows

$$\sigma = \sqrt{\frac{\delta B_y^2}{8\pi^2 \tau^3 B_{\mathrm{Xe}}^2} + \frac{\gamma^2 \delta B_z^2}{2\tau} + \frac{\delta \nu^2 \delta B_y^2}{2\tau B_{\mathrm{Xe}}^2}} \tag{5.13}$$

where the first term is the angle white noise or noise between the phase of the drive and the phase of the noble gas rotation. This component dominates the first part of the Allan variance measurement decreasing as $1/\tau^3$ where τ is the averaging time and B_{Xe} is the noble gas field. The other two terms describe the ARW contributions from the bias field and the phase fluctuations inherent in the noble gas detection, as limited by $\delta\nu$. Figure 5.1 is an Allan variance projection that uses measured noise, field, and T_2 numbers; it results in an uncertainty of $\approx 0.006\mathrm{deg}$ after 1 hr of averaging. We ultimately do not know the limits to the bias stability since it depends on the specific system's long term drifts.

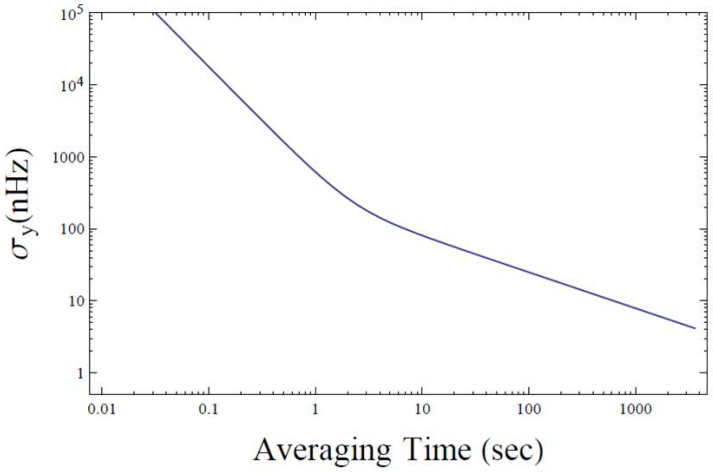

Figure 5.1: An Allan deviation simulation that uses the numbers we currently measure. This results in a bias stability of $\approx 0.006\mathrm{deg}/\sqrt{\mathrm{hr}}$ after 1 hr of averaging.

5.1.1 Parametric Modulation

For many of our purposes we need the ability to measure magnetic field components both perpendicular and parallel to the probe beam. To do this we implement parametric modulation along the pump beam direction. For reasons that will be explained, this parametric modulation is non-conventional and, therefore, warrants some explanation.

In conventional parametric modulation an sinusoidally oscillating field is applied along the pump direction. The field components to be detected appear as the first and second harmonic signals on the probe Faraday rotation. For sinusoidal modulation, the relative amplitude of the response as a function of the oscillating field amplitude follows a Bessel function. This means that the oscillating field amplitude can be adjusted so that both the $1f$ and the $2f$ components have good response. Parametric modulation allows us to observe with a $\hat{y}$ probe, B_y at the first harmonic:

$$S_y = \frac{2J_0 J_1 \Omega_y R}{\Gamma'^2 + J_0^2 \Omega_y^2} \sin(\omega t) \tag{5.14}$$

and B_z at the second harmonic:

$$S_y = \frac{2J_0 J_2 \Omega_z R}{\Gamma'^2 + J_0^2 \Omega_z^2} \sin(2\omega t) \tag{5.15}$$

For sinusoidal modulation J_0, J_1, and J_2 are Bessel functions. The above equations can be used for $\hat{z}$ detection as well, but now the first harmonic detects B_z and the second harmonic detects B_y. For future experiments, it is important to point out that the parametric modulation is not limited to sinusoidal modulation, but can be any periodic function. This is important because we need the modulating field to be zero during the 2π pulses, otherwise uncontrolled alkali rotations will occur.

The desire is to create a field waveform that closely mimics sinusoidal modulation, but is zero during the 2π pulses. The resulting waveform is that shown in Fig 5.2. The waveform has been adjusted to be zero for longer than the 2π pulse to ensure that there is no overlap. Technically, because of the characteristics of the driving circuit, the shape of the waveform and the timing of the zero crossings must ultimately be finely adjusted by hand while looking at the applied field and the 2π pulses.

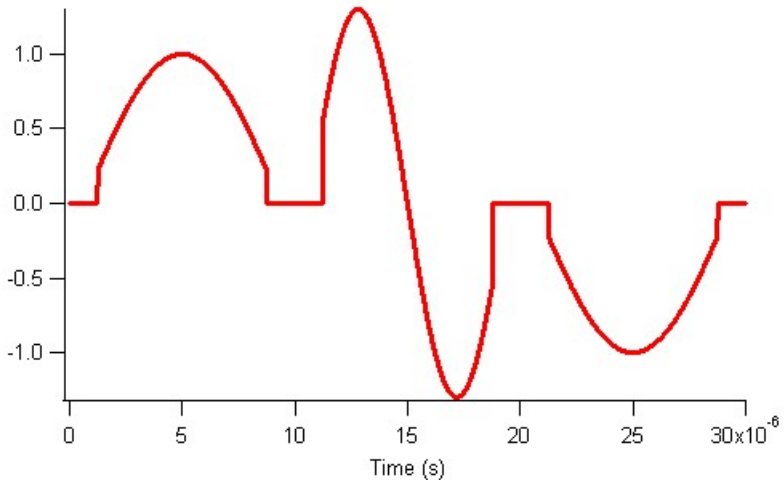

Figure 5.2: The parametric modulation waveform created ostensibly to have zero field during the 2π pulses. Note that because of AC coupling, the actual waveform applied to the circuit is the integral of this function.

5.2 $\hat{y}$ Detection: Noise from 2π Pulsing

When using the PPR magnetometer to make noise measurements with the parametric modulation as described above, we originally found that the noise levels increase a factor of 10 above the SERF magnetometer's noise. Figure 5.3 shows the B_y noise level with and without the 2π pulses. In addition to the unexpected factor of 10 increase, the $\hat{y}$ and $\hat{z}$ noise levels are the same (Fig. 5.4). We instead anticipated higher B_z noise since we expected the pulsing field along $\hat{z}$ to be noisy. Because this is not the case, but instead δB_y and δB_z are at similar levels, it is likely that what we are detecting is not real magnetic noise along either direction.

These noise measurements are taken with our original PPR detection direction, which is $\hat{y}$, so that the 2π atom rotation can be observed directly. Along with this benefit comes the drawback that any pulse fluctuation shows up as polarization noise on the probe. The polarization noise on the the detection would then be seen as equal B_y and B_z noise. We can verify the pulse noise dependence by measuring the field noise as a function of the pulsing parameters: width and repetition rate. Figure 5.5a shows the difference in noise for 10kHz and 25kHz pulsing as compared to the no pulsing case. Figure 5.5b is data for multiple pulse frequencies and widths. The repetition rate dependence is simply explained by the fact that as the noise source from the pulsing comes less frequently, the noise decreases. The pulse width trend shows that for narrower pulses, any pulse width fluctuations become a more significant error on the total atom rotation, resulting in higher noise. The trend minimizes at the optimal pulse width, then begins to increase once again, but not as dramatically, most likely due to multiple spin exchange collisions during the pulse. Another interesting conclusion that can be drawn from these pulse width and repetition rate results is that a higher n for $2n\pi$ pulses gives lower noise. Not only can the repetition rate be decreased while keeping the same bias field, but the noise for a 6π pulse at 25kHz is lower than the noise of a 2π pulse at the same rate.

One further test to ensure that the noise we measure with the $\hat{y}$ probe is not magnetic noise introduced by the pulsing, that couples in some way to $\hat{y}$, is to direct the pump parallel to the pulsing field. Because the pump and the field are parallel, the 2π pulses will not rotate the atoms;

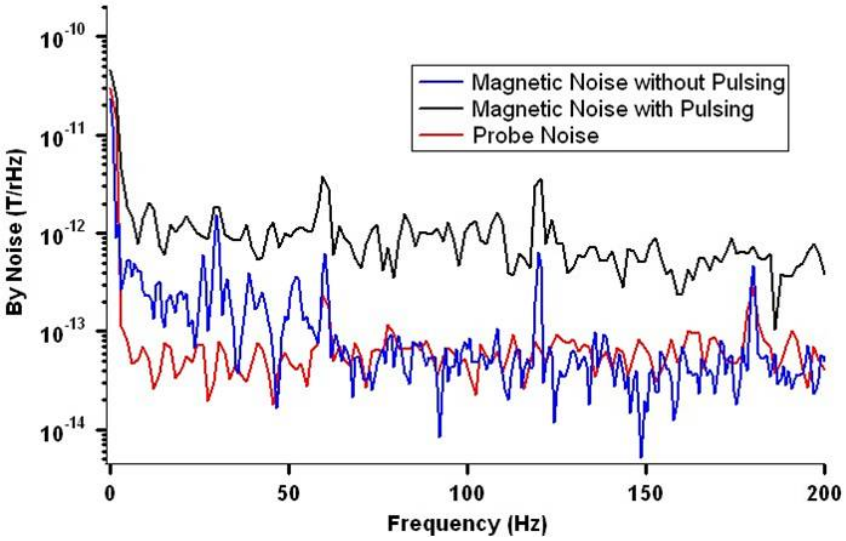

Figure 5.3: The majority of the noise is introduced with the 2π pulsing.

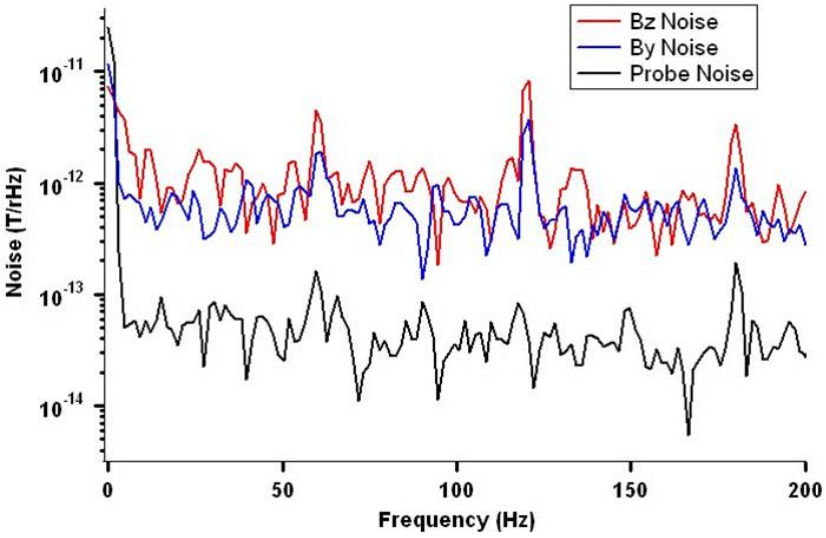

Figure 5.4: An unexpected result is that the B_y and B_z noise are the same. We would expect the B_z noise to be higher since that is the direction of the 2π pulses. This is a strong indication that we introduce noise polarization due to pulse area fluctuations when the 2π pulses are turned on.

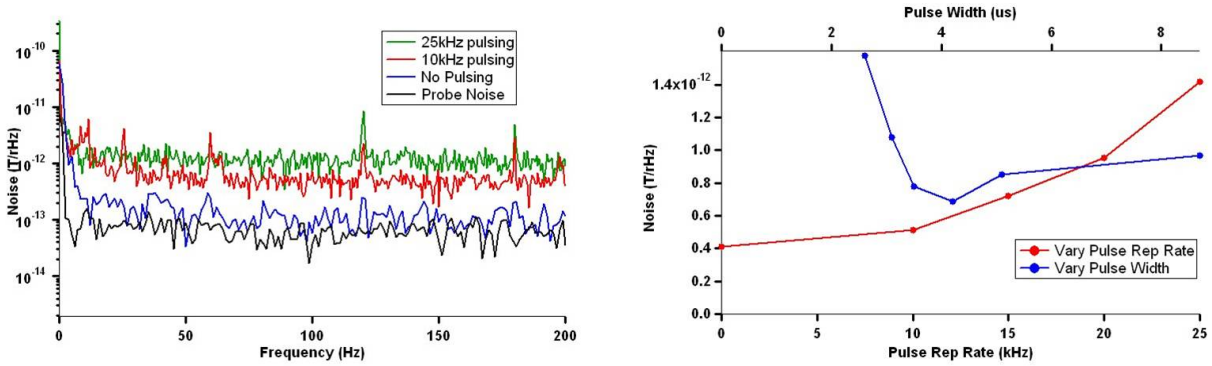

(a) **(b)**

Figure 5.5: The figure on the left shows the noise spectra as the pulse repetition rate changes for two frequencies. The figure on the right plots the noise for several different pulse repetition rates and pulse widths. As the repetition rate decreases, the noise decreases due to the noise source becoming less frequent. As the width narrows, any fluctuation on the pulse becomes a more significant error on the total rotation; therefore, the noise increases.

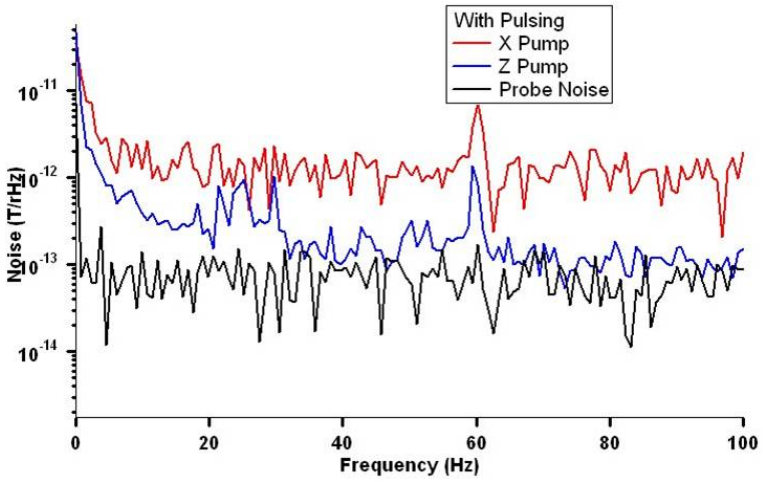

Figure 5.6: As a test for polarization noise caused by fluctuations on the pulse, we direct the pump parallel to the pulsing field. The fact that the noise level does not increase when the 2π pulses are turned on indicates that the high noise level is not magnetic field noise introduced by pulse width fluctuations.

in this way, we can measure the field noise, not the polarization noise, introduced by the 2π pulses. The results of this experiment are seen in Fig. 5.6. As can be seen, the noise with the 2π pulsing on does not increase when the pump is directed along $\hat{z}$. This is a clear indication that the increased noise level is from polarization fluctuations on the probe due to noisy 2π pulses.

The results of these experiments raised the question of how stable the pulses need to be in order to reach the non-pulsing noise levels. A rough estimate of the pulse width stability required to reach 1×10^{-13} T$/\sqrt{\text{Hz}}$ is calculated by equating the pulse width τ_p and its error σ_p to the field fluctuations between pulses σ and the time the pulses are off τ: $\sigma_p \tau_p = \sigma \tau$. Then we can use the duty cycle to define $\sigma = d\sigma_p$ and the field noise:

$$\delta B = \frac{d\sigma_{\mathrm{r},p}/\gamma\tau_p}{\sqrt{f}} \tag{5.16}$$

where f is the pulsing frequency and $\sigma_{\mathrm{r},p}$ is now the pulse width fluctuations in rotation units. Solving for the pulse rotation fluctuation noise required to get 1×10^{-13} T$/\sqrt{\text{Hz}}$ we find $\sigma_{\mathrm{r},p} = 3 \times 10^{-6}$. Converting this to a pulse width using $\gamma \frac{1}{2} B \delta\tau_p = 3 \times 10^{-6}$ we find $\delta\tau_p = 13$ ps. This is much more stable than anticipated from our current pulse drive circuit. In order to stabilize the

pulse widths even further, a new capacitive discharge circuit was built. However, this circuit, as described in detail in section 7.2, gave us no better pulse stability than the other.

5.3 $\hat{z}$ Detection: New Parametric Modulation

The results of the above experiments reveal that detecting along $\hat{y}$ is not an option. For this reason, we redirected the probe along $\hat{z}$ so that we would no longer pick up the 2π pulse rotations. The first attempt was unsuccessful as seen in Figure 5.7, but a mixing of the $\hat{y}$ polarization noise into $\hat{z}$ can simply be explained by a stray B_x during the 2π pulses: $P_z \propto \Omega_y R_x + \Omega_z \Omega_x R_x / \Gamma'$. This is experimentally demonstrated (Fig 5.8) by adding a DC B_x and observing the B_y noise increase, while the B_z noise stays the same. The conclusion from this test is that, even with the fancy parametric modulation scheme, there is a residual B_x during the 2π pulses that mixes P_y noise into the $\hat{z}$ probe. This hypothesis is proven by turning off the parametric modulation field while using $\hat{z}$ probe detection and measuring a reduced noise level. The green trace in Fig 5.9 is the B_y noise with $\hat{z}$ detection without parametric modulation; it is lowered to the level of the noise without 2π pulsing, which is the blue trace.

Because of these results, we implement a new parametric modulation scheme where the parametric field is a sequence of $\pi/2$ pulses instead of a continuous waveform. In this way, the separation between the PM pulses can be adjusted so as to ensure zero field when a 2π pulse comes. The adjusted pulse sequence is shown in Fig 5.10a, where the spacing in the parametric modulation has been appropriately adjusted. The resulting $1f$ (B_z) signal is shown in red and the $2f$ (B_y) signal is shown in green in Fig 5.10b.

Figure 5.11 shows that once this new form of parametric modulation is implemented, the noise with and without the pulsing is the same. In conclusion, the dramatic increase in noise that we observe when using $\hat{y}$ detection or $\hat{z}$ detection with a non-optimum parametric modulation field is due to pulse fluctuations causing polarization noise. The experiments reveal that the pulses we generate are stable to at least 100 ps out of 2μs, but that is not stable enough to continue using $\hat{y}$ detection, so the probe must be moved to $\hat{z}$ and pulsing parametric modulation must be

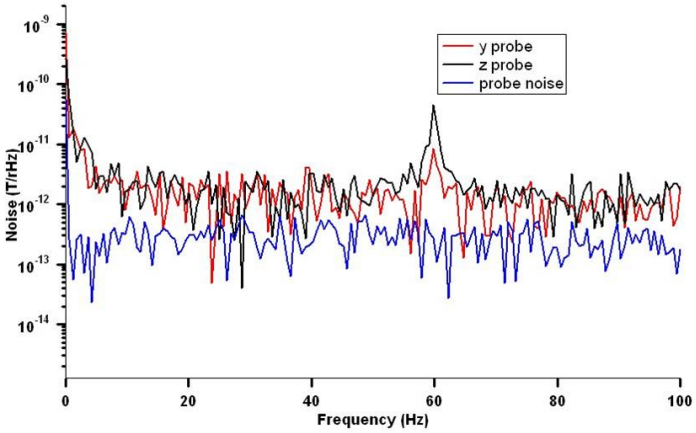

Figure 5.7: The initial noise measurements with $\hat{z}$ probe compared to the $\hat{y}$ probe measurements show no reduction in noise.

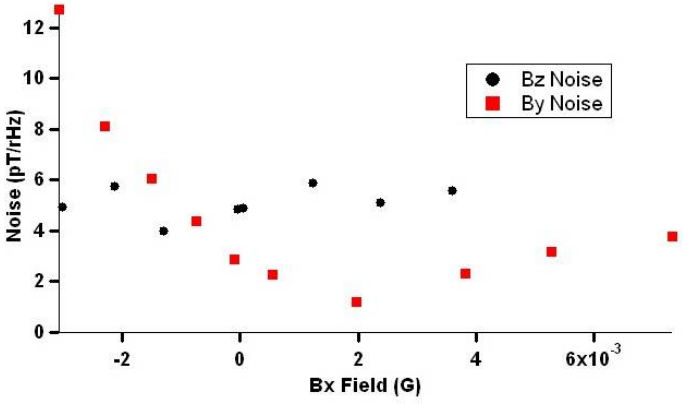

Figure 5.8: B_y and B_z noise are plotted as a function of applied B_x. This experiment demonstrates the mixing of P_y noise into P_z by a stray B_x during the 2π pulse.

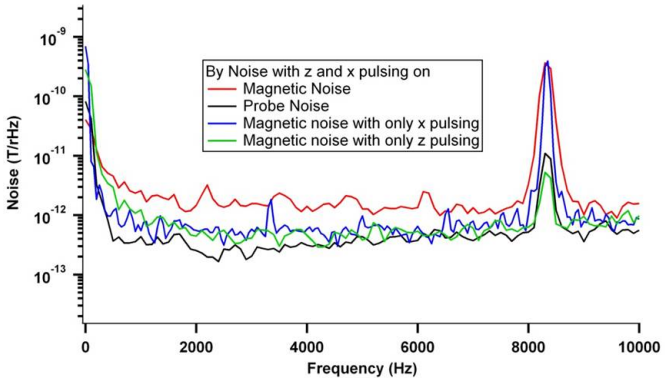

Figure 5.9: The red trace is the noise level for $\hat{z}$ probe with the parametric modulation. The blue trace is the noise without 2π pulsing, but with parametric modulation. The green trace is the noise with 2π pulsing, but without parametric modulation. The noise very clearly decreases when parametric modulation is turned off indicating that the parametric modulation is the source of the stray B_x that mixes the $\hat{y}$ polarization noise into $\hat{z}$.

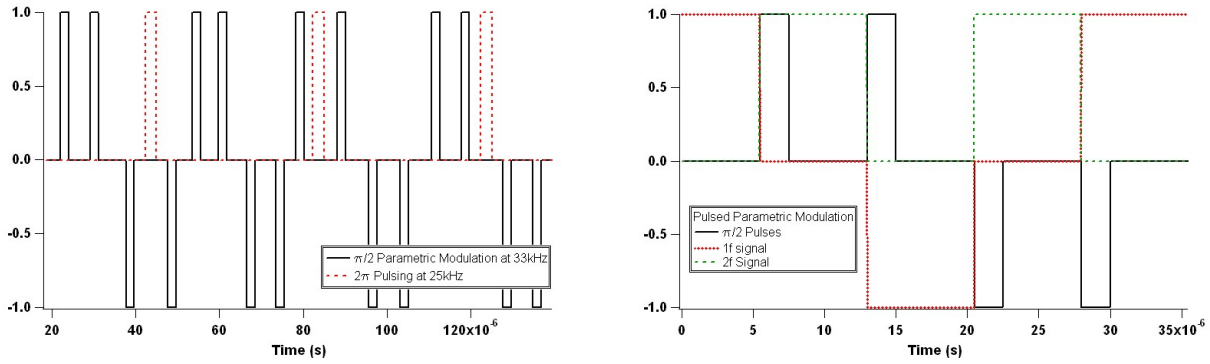

(a) **(b)**

Figure 5.10: The figure on the left is a train of the parametric modulation pulses (solid) shown staggered with the 2π pulses (dashed). The spacing of the PM pulses has to be adjusted to accomodate the 2π pulses. Changing the spacing of the 2π pulses did not work; probably for reasons described in Sec. 7.1.2. The figure on the right shows the expected 1f and 2f signals due to the PM pulsing sequence.

implemented in order to measure B_y and B_z simultaneously. Doing this, we get the noise numbers quoted at the beginning of this chapter.

5.3.1 Pulse Parametric Modulation Cross-Talk

There is one outstanding issue with this new method of parametric modulation which is cross talk between the $\hat{y}$ and $\hat{z}$ channels.This problem is exacerbated by the fact that the Rb atoms have a relaxation rate which tends to mix the 1f and 2f signals making it necessary to choose a pulsing frequency that is fast enough to make the Rb relaxation negligible. The current pulsing frequency of 33kHz is almost fast enough, but due to the fact that the pulses have a finite width and we need to time them with the 2π pulses, increasing this frequency is not particularly viable. Since discovering these issues, we have moved away from optimized parametric modulation detection for both $\hat{y}$ and $\hat{z}$ fields and use direct detection for B_y and a very small $\hat{x}$ sinusoidal perturbation for B_z only when it is necessary.

Some work modeling the effect of the cross talk has been done by Mike Bulatowicz, but the results he obtained in regards to pulse spacing and shape have not yet been tested.

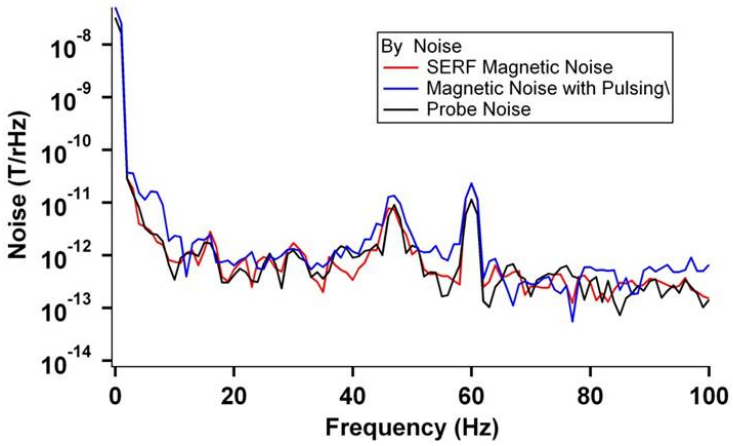

Figure 5.11: Using the staggared pulsed parametric modulation scheme, the noise does not increase when the 2π pulsing turns on.

Chapter 6

Apparatus Setup and Operation Details

This chapter details the apparatus' components and their respective optimization procedures. Also contained in this chapter are alkali magnetometer operation procedures for optimizing the alkali polarization and density and characterizing relaxation rates. Operation details that are specific to the noble gas are in Chapter 4.

As a point of reference, a photo of the shield, placement of the apparatus in the shield, and the majority of the optics is shown in Fig 6.1.

Figure 6.1: The apparatus is shown within the shields. Note the asymmetry of the ports in the shield; this forces us to place the cell and field coil setup closer to one endcap than the other, which is a main cause of field gradients. The pulsing field coils have been designed to minimize these gradients.

6.1 Cell and Heaters

Most of the measurements in this work were taken in a nominally spherical cell with an 8mm diameter filled with 40Torr of Xe with 80% ^{131}Xe, 300 Torr N_2, and ^{85}Rb. The cell is mounted in a 3-D printed ceramic form housed in a boron-nitride heatsink, this oven is heated by two pairs of 50Ω Minco resistive film heaters adhered to two of its sides. In order to cancel to first order residual fields produced by the heaters, the heater pads are sandwiched and wired in such a way that the resistors are in series, but the current in a pair flows in opposite directions. We further suppress any stray DC field produced by the heaters by running AC current through them at a frequency outside of the bandwidth of our magnetometer. The heater circuit needs to supply 8W of power in order to heat the cell to 120C; we do this by using an audio amplifier to amplify an input signal at 20kHz. We use this frequency because the power amplifier is rated to only 50kHz and its output starts to fall off at 20kHz. This is not quite high enough in frequency to eliminate all residual signal from the heaters. In the future we hope to increase this frequency to about 100kHz. The heat sink and heaters are all wrapped in aerogel insulation and inserted into the center of our magnetic field coils.

We currently have no active temperature sensor in our setup, so we take absorption lineshape measurements to monitor the density of the Rb atoms. These linewidths we fit to:

$$[\mathrm{Rb}] = m(f-f_0) + \mathrm{I}_0 * \exp\Big[-\frac{3 f_{osc} n l c^2}{2 f^2}\frac{\Delta_n}{\Delta_p} \times \Big(\frac{7/12}{1+4((f-f_1)/\Delta_p)^2} + \frac{5/12}{1+4((f-f_2)/\Delta_p)^2}\Big)\Big] \tag{6.1}$$

where $f_1 = f_0 + 1.77$ GHz and $f_2 = f_0 - 1.265$ GHz are the hyperfine resonance frequencies in GHz; f_{osc} is the oscillator strength (0.696 for the D2 transition and 0.342 for the D1 transition). $\Delta_p = 7.4$GHz is the pressure broadened linewidth, which is found at very low density by fitting the absorption profile and letting Δ_p be a free parameter; it should be approximately 18Ghz/Amg [Romalis, Miron, and Cates, 1997]. $\Delta_n = 6$MHz is the natural linewidth. We also have inserted a linear term to Eqn. 6.1 that accounts for the changes in laser intensity as the frequency is scanned.

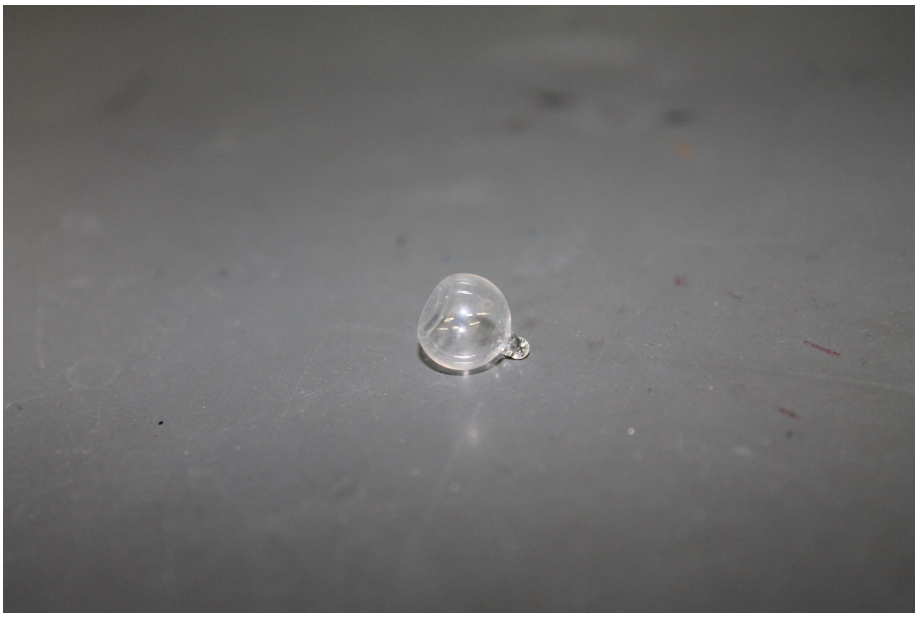

Figure 6.2: This is the cell used for the majority of experiments in this thesis. Its Ehrlenmeyer flask like shape caused the beams to be greatly distorted.

A DC offset is also inserted to account for residual light seen by the photodiodes. These measurements are consistent day to day, with variations within 10%, but we hope to put in a thermistor for active stabilization in the next iteration.

6.1.1 Cell Imperfections

The cell that we are currently using is a non-ideal shape: they are nominally spherical with a pull-off and a flat section opposite it (see Fig 6.2. Because of this shape the light going through the cell, although collimated upon entrance, is highly distorted by the time it exits. This causes three main problems. The first is the difficulty of alignment, which will be discussed in the section below. The second is related to alignment, and deals with the distortion within the cell. Since the light upon exiting is distorted, it is likely that the light within the cell is also distorted and travelling in many different directions. This leads to uncertainty in both pump and probe directions within the active region. It is likely that we have pump light along directions that are not $\hat{x}$, which would cause a multitude of potential problems including: a decrease in polarization, a non-perpendicular

alignment of the pump and probe, atom signal in directions there should be no atom signal, alkali fields pointed in uncompensable directions, etc. Despite the potential seriousness of each of these problems, we have not been able to pinpoint anything in particular that inhibits our ability to do the experiments; therefore, we have been able to do many proof of principle experiments in this non-ideal cell. Once we get down to the details of noise measurements where these problems may compound, we will need to either switch to a cubic cell or make sure the noise is not dependent on this issue. The former is the easier solution. We have not yet switched to the new cell because the current cell is so well characterized.

6.2 Magnetic Field Coils

The magnetic field coils that we have implemented are designed for our particular setup to minimize field gradients at the center of the cell with low inductance and low coupling to the magnetic shields. The magnetic shield that we are currently using forces us to place the cell off center (see the optical access ports in Fig 6.1), closer to one endcap than the other. Because of the proximity of the endcap, if we use a simple field coil design, such as a Helmhotz configuration, we have significant field gradients across the cell due to reflections in the end-caps. If the field is not uniform then there will be points in the cell that produce slightly less than a 2π rotation and points that produce slightly more. The inductance requirement is for ease of driving the current quickly through the circuit. We are not sure that inductive coupling to the shield will cause us any issues, but there are a couple of experiments that we have done to indicate it might be a problem, e.g Sec. 3.4.0.1. Since the DC shim fields are small, the $\hat{x}$, $\hat{y}$, and $\hat{z}$ shim coils can all be approximately Helmholtz configurations. The $\hat{x}$ and $\hat{y}$ are three turns with a field/current calibration of 1.13G/A and the $\hat{z}$ is 10 turns with a field/current calibration of 2G/A. The coil calibrations are all done using the atoms as a measure of a resonance frequency: $\hat{x}$ and $\hat{y}$ with the noble gas frequency from free induction decay and $\hat{z}$ from an AC coupled PPR magnetometer experiment. The measured calibrations agree well with calculated field/current calibrations.

The pulsing coils deserve a little more attention. The first iteration for uniform field, based on a Merrit configuration as described in [Kirschvink, 1992], did not take into account the magnetic

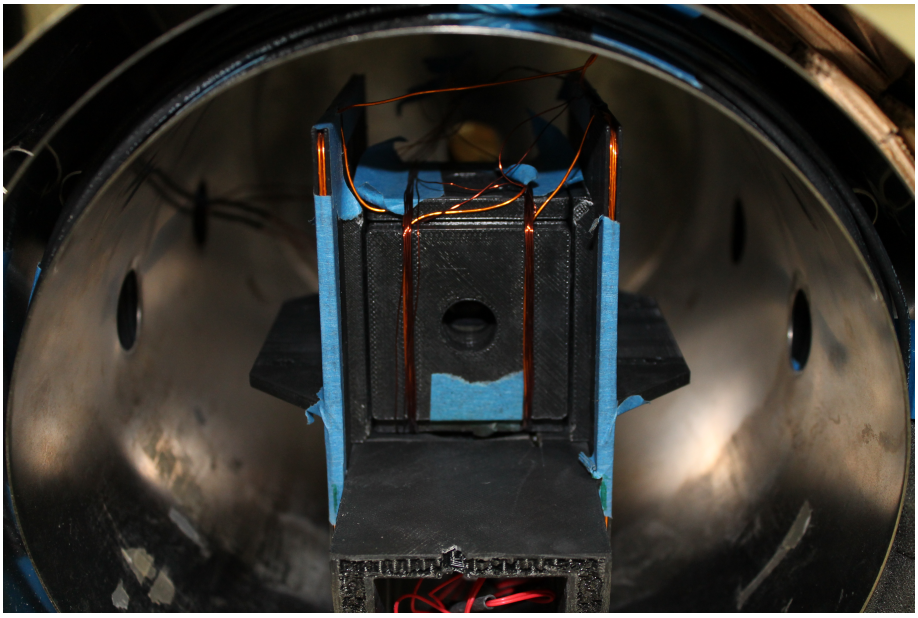

Figure 6.3: This is a side view of the field coil frame. The pulsing coil consists of the two large frames on the end and the two near the center.

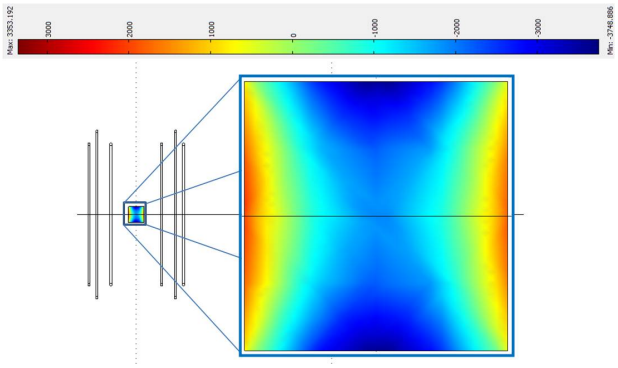

(a) A finite element analysis of the first coil design that was intended to cancel the magnetic moment at the shield shows a large field gradient due to not taking the asymmetry of the shield into account.

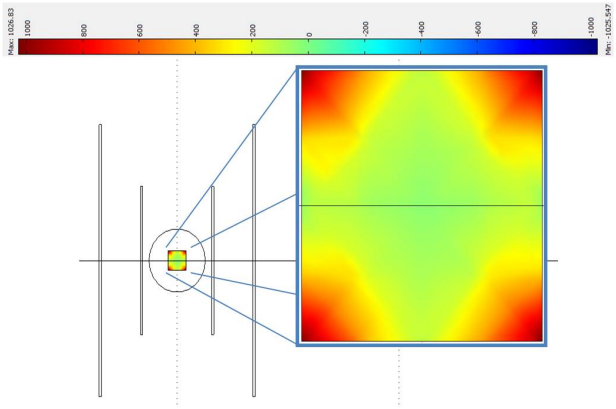

(b) A finite element analysis for the coils designed by Mike Bulatowicz shows a much improved magnetic field gradient across the cell as compared to the figure on the right

Figure 6.4: The color in both images shows departure from volumetric average in parts per million. Scales are different in figures (a) and (b). Figure (a) spans 6000ppm; figure (b) spans 2000ppm.

shielding and its effect on the field in the cell, so the configuration produced the field gradient seen in Fig 6.4. Because of this dramatic gradient, we enlisted the help of Mike Bulatowizc to design a set of coils that would reduce the field gradient, and have low coupling to the shields and low inductance. The field uniformity of his final design is shown in Fig. 6.4. It consists of two pairs of square coils:

- Coil 1: backward polarity; 3 loops; 10.906 cm side length; centered at x = -3.471 cm
- Coil 2: forward polarity; 10 loops; 5.93 cm side length; centered at x = -1.600 cm
- Coil 3: forward polarity; 10 loops; 5.93 cm side length; centered at x = +1.602 cm
- Coil 4: backward polarity; 3 loops; 10.906 cm side length; centered at x = +3.472 cm

The different polarities of the field help to cancel the magnetic moment at the shield; the slight asymmetry cancels the resulting gradient from the endcap.

Because it is important to know in order to build the pulsing circuit, we measure the inductance of the pulsing coils with a simple LR circuit. By sending in a square wave or a pulse, we can measure the voltage over the resistor to extract the inductance from the time constant $\tau = L/R$ associated with the voltage buildup. The pulsing coil set is 29μH in good agreement with the calculated 32μH.

6.3 Mounting Cell and Field Coils in the Shield

Because the cell needs to be mounted precisely in the center of the mutually perpendicular field coils, we designed a single 3D printed frame around which all the field coils are wound. The frame also has a hole for the cell oven that is centered in the field coil frame. Because this space for the oven was designed with room for the insulation, the reliability of perfectly centering the cell can be improved. The frame was printed at the WID on the UW campus out of black ABS plastic. A higher temperature grade plastic is desirable in the future since this plastic warps at the temperatures we keep the oven inspite of several layers of insulation between the oven and the coil frame. The warping is not significant enough to change the coil placement.

Future iterations of the coil frame and general setup design might want to take some of these suggestions:

- Higher grade/ higher temperature plastic for the field coil frame
- Better coil frame stand: can be put back in the exact same place within the shield and is held in place within the shield
- Different design for $\hat{x}$, $\hat{y}$, and $\hat{z}$ shim coils. The $\hat{x}$ and $\hat{y}$ coils are currently very difficult to wind well. Currently there is no actual frame design for the $\hat{z}$ coils since we had originally planned to run both the pulsing and shim fields through the pulsing coils.
- Symmetric magnetic shield
- Windows on the oven to mitigate hot air currents
- Put all the probe optics on pedastal stands to mitigate vibrational noise at ≈ 40Hz.
- Change the optical table legs to floating legs.
- 3D printed alignment pinholes that ensure centering
- Better heating setup: the biomagnetism project has designed a ”puzzle” heater system consisting of four resistive heaters adhered directly to the cell at the active area. These heaters are designed to have minimal stray fields and will be heated with AC current; they have been implemented on that project with good results
- Active temperature monitor
- Better cell holder/oven that has more thermal contact with the cell and less wiggle room
- More reliable way of placing the cell/oven in the coil frame: ensure centering
- Implement a $\hat{y}$ probe by sending the laser through the cubic cell off-center so that it does not hit the pull-off. This is not necessary, but it would be nice to have for 2π pulse diagnostics.

- Implement an automatic de-gaussing circuit.
- Develop and automatic magnetometer response and noise measurement program for the FPGA
- Develop a PID look within Labview with variable gains

The coil frame is mounted inside the magnetic shield by resting it on a semi-circular mounting block, also 3D printed. The mount is then manually aligned with a set of ports along $\hat{x}$ and $\hat{y}$, where $\hat{z}$ is always defined as the long axis of the shield.

6.4 Lasers and Optics

We use three DFB lasers from Eagleyard Photonics. Two of these lasers are centered on the $D1$ transition to be used as our pumping lasers. The other is centered on th $D2$ transition to be used as the probe laser. A simplified schematic of the optical setup can be seen in Fig. 6.5. Each laser comes out of the diode linearly polarized, but then acquires some degree of elliptical polarization while traversing the optics; for this reason the polarization is cleaned up with a polarizing beam splitter before the pump light is circularly polarized. The polarizing beam splitter also lends itself to intensity control of the individual beams with the addition of a $\lambda/2$ plate in the beam path, which adjusts the extinction of the light through the PBS.

In the schematic can be seen the essential components of operation. The probe laser is linearly polarized upon exiting the DFB and its intensity is controlled, for various purposes, by rotating the $\lambda/2$ plate to change the transmission through the polarizing beam splitter. The $\lambda/4$ plate is in place to null out slight elliptical polarizations that may be introduced into the beam. On the other side of the cell is another polarizing beam splitter to separate out the two polarization components for a Faraday rotation measurement.

The frequencies of the two pump beams are determined by the AC Stark shift and are detuned in such as way as to cancel out the average shift seen by the alkali atoms. The effects of the AC Stark shift will be discussed in more detail below. The two beams are combined on a non-polarising

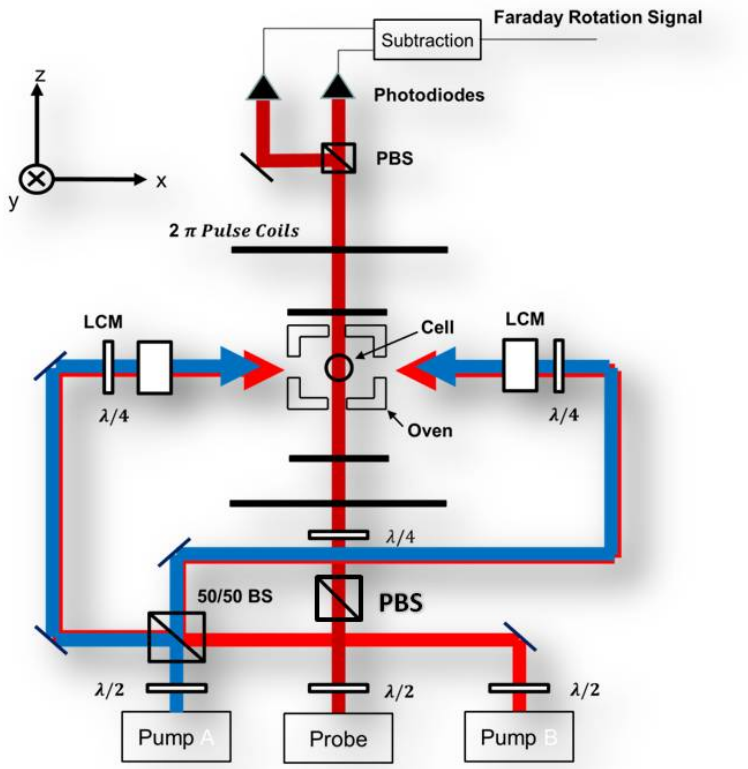

Figure 6.5: A simplified schematic of the optical setup shows the essential components for transverse optical pumping and synchronous spin exchange optical pumping. The two colors of pump light (equally detuned above and below resonance) are combined on a non-polarizing beam splitter then directed along $\pm\hat{x}$. The polarizing beam cubes that clean up the pump polarization are not shown. The probe beam is along $\hat{z}$ since we now have no access to $\hat{y}$ and the Faraday rotation detection optics are shown.

beam splitter and we can subsequently counter-propagate the two, now combined, pump lasers to minimize intensity gradients across the cell.

6.5 Optics: Pump

6.5.1 Pump Polarization Optics

As can be seen in Fig. 6.5, the pump polarizing optics consist of a polarizing beam cube, a liquid crystal variable retarder, and a quarter waveplate. The PBS serves the purpose of cleaning up the beam polarization and providing a method, along with the $\lambda/2$ plate immediately after the laser output, of controlling the beam intensity without changing the frequency. After the PBS the light enters the liquid crystal variable retarder which either flips the linear polarization of the light exiting the PBS by 90° or leaves it unaffected. The light then enters the $\lambda/4$ plate and becomes circularly polarized. Every time the voltage on the LCVR is changed to take the liquid crystals from zero retardance to half-wave retardance the pump light polarization switches from σ^+ to σ^- and vice versa. We flip the polarization twice every noble gas Larmor period.

The liquid crystal variable retarders deserve a little more mention in terms of optimizing their parameters and making note of their deficiencies. We procured these devices from Meadowlark Optics as a simple way to switch the light polarization quickly at a controllable frequency; the time for switching the light polarization with this device is $\approx 150\mu$s, which is short compared to the optical pumping time. The slower the switching time, the longer it takes for the Rb atoms to become re-polarized leading to a decrease in Xe polarization and a larger phase shift in the alkali compensation field (Sec. 3.2.2). It would be possible to compensate for this time delay by adding a π pulse every time the polarization is flipped, but this is difficult to implement because of interferance with the 2π pulse sequence.

The liquid crystal device works by changing the orientation of the individual crystals, which in turn changes the birefringence of the device from zero wave (maximum applied voltage) to full wave retardance. The main issue with this device is that it is not consistent from one device to another and changes with time of operation. The latter is the more serious of the two affronts. The former is fixed by acquiring two drivers and individually optimizing the respective crystals; however, the optimization voltage changes over the course of days and weeks. This change has never been systematically tracked. Most of the time there is a reduction in polarization/signal size

or a change in AC Stark nulling that indicates that the circular polarization of the pump beam has shifted, thus causing one direction of light to be pumping more effectively. Once this is noticed the pump polarization is re-optimized.

The process for optimization is a bit of an art. The typical method begins by adjusting the PBS and the quarter waveplate without the liquid crystal to obtain good circular polarization > 0.99. The liquid crystal is then inserted between the PBS and the $\lambda/4$ plate. The goal is to obtain zero retardance and half-wave retardance with the liquid crystal, so preliminary voltage adjustments are made to obtain the same degree of circular polarization at a high voltage (zero wave), a maximum of 80V for the LCVR, and a mid voltage (half wave), around 30V. The handedness must then be checked by looking at a magnetometer signal and ensuring that the signal flips 180° when the voltage switches. An indication that the same degree of circular polarization has been obtained, is that the resulting signal size for σ^+ should be the same as the size for σ^-.

If good polarization cannot be obtained in this simple way, then the art of balancing σ^+ and σ^- by alternately twisting the $\lambda/4$ plate and adjusting the LCVR voltage at low and high voltage begins. The goal is to get as high and as similar of values for the degree of σ^+ and σ^- as possible. If this is not obtained, then there will be a pumping imbalance that may affect the effectiveness of pumping the noble gas and result in a $1f$ noble gas signal. The imbalance can theoretically be nulled by adjusting the duty cycle of the pumping. The effects of unbalanced pumping have not been studied in full, but it is something to keep in mind.

The best way to help attain high levels of circular polarization is to have all the pump polarization optics in a row immediately before entering the cell. In this way, elliptical polarization is not introduced in between the individual components. As it is now set up, the light exiting the liquid crystal bounces off one mirror before going through the $\lambda/4$ and then into the cell. This is because there is not enough room between the last mirror and the shield to put all the necessary optics (PBS, LCVR, and $\lambda/4$).

6.5.1.1 Other Options for Light Polarization Modulation

The LCVRs have imperfections that make them frustrating to work with. First of all, they are not able to hold their retardance over long periods of operation. This effect has not been studied in detail, but we do notice a degradation of the circular polarization after some time, which could only be attributed to the liquid crystals. They are also finicky to adjust and at times it is very difficult to get good circular polarization. An option for replacing these devices is to use either a spatial light modulator or a MEMS optical switch (Thorlabs OSW12-780E) that will allow us to switch the pump beam path very quickly from one path that gives σ^+ and another that gives σ^-. Some more thought needs to go into this in terms of coupling the light to the device.

6.5.2 AC Stark Nulling

An oscillating electric field will cause a shift in the atomic energy levels that is analogous to the energy level shift cause by a static magnetic field. For this reason, the AC Stark shift will introduce a false magnetic signal along whichever direction the laser light is propagating; this would then be nulled out with a real magnetic field. The discrepancy between a false magnetic field and a real magnetic field is particularly important when doing synchronous spin exchange optical pumping. First of all, the noble gas nuclei are only susceptible to the applied fields, not the shift induced by the light. Secondly, the AC Stark shift is dependent on whether the laser is σ^+ or σ^- polarized light; therefore when we switch the polarization between σ^+ and σ^-, an AC $\hat{x}$ field is introduced if an $\hat{x}$ field was added to cancel the AC Stark field. This is our first handle on nulling the effect. By applying an oscillating $\hat{z}$ field, we can monitor the amount of $\hat{x}$ field that is introduced when the pump polarization is flipped. Assuming the degree of circular polarization is the same for σ^+ and σ^-, we can make adjustments to the other parameters on which the AC Stark depends in order to null it. The other two handles used to null the AC Stark are the detuning and intensity of each pump laser. Two lasers at 795nm are combined on a 50/50 beam splitter and their detunings are set to roughly equal and opposite sides of the optical transition, where the AC Stark is approximately equal and opposite. A quick and easy way to do this is to observe the size of the signal for each pump individually and adjust the detuning close to resonance until the signal sizes

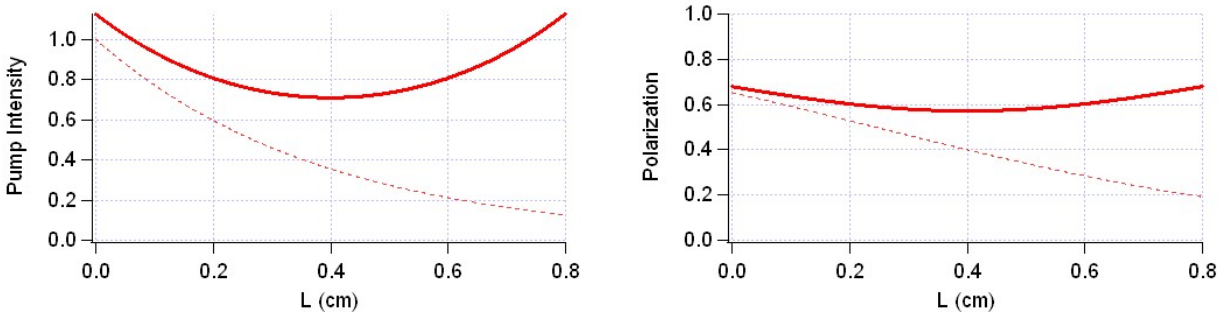

(a) Pump intensity as a function of position

(b) Polarization as a function of position

Figure 6.6: The pump intensity and the atom polarization as a function of position in the cell are shown for single (dashed) and dual)solid sided pumping. As can be seen, dual sided pumping greatly mitigates the polarization gradient across the cell.

of the respective pump beams match. Fine adjustments are made to further null out the effect by observing the oscillating $\hat{z}$ field and adjusting the intensity of an individual pump until all signal is nulled, or is centered on its phase shift, when the pump polarization flips.

6.5.3 Dual Side Pumping

A second order effect that is a concern is the AC Stark gradient. As the pump light propagates through the cell it is attenuated resulting in a linear intensity gradient across the cell. We do not fully know the effect of this gradient, but naively it would compound with the Rb polarization gradient and degrade the magnetometer perfomance. For this reason we implement dual sided ($\pm\hat{x}$) pumping so that the intensity gradient is quadratic instead of linear. The arrangement of the pump polarizing optics must be carefully chosen to ensure that the two pump beams are working together to add angular momentum to the alkali atoms. The basic scheme of the pump polarization optics can once again be seen in Fig. 6.5. The light is transmitted through the polarizing beam splitter, so each beam has the same linear polarization prior to the $\lambda/4$. The quarter waveplates are oriented parallel to each other, so that upon entering the cell the light has the same circular polarization. It is easy to see the effect of the pump beams not working in concert to supply angular momentum; there will be no response. In this case, the $\lambda/4$ needs to be rotated by $45°$.

6.5.4 Setting and Detection of 2π Pulses with Dual Side Pumping

Since we have optical access to the transmitted laser beam on only two of the three axes, we sacrifice the direct $\hat{y}$ detection of the 2π pulses so that we can implement dual sided pumping; this means that the probe beam is directed along the $\hat{z}$ direction. However, we still need to access the information that allows us directly to set the 2π pulse area. This gives us two choices: detect pump transmission or use circular dichroism [Lancor, Babcock, Wyllie, and Walker, 2010].

Using pump transmission to measure the rotation of the spins about the $\hat{z}$ axis is not as sensitive as a Faraday rotation measurement or a circular dichroism measurement, so we decided to try a circular dichroism measurement of the 2π pulse rotation signal. Circular dichroism uses a circularly polarized probe beam to measure the polarization of the atoms as they rotate in the plane of the probe light. Since the absorption cross section $\sigma = \sigma_0(1 - \mathrm{P}/2)$ for $\mathrm{P}_{3/2}$ where σ_0 is the cross section for unpolarized light this method will give us not only a measure of the 2π pulse area, but also a simple measure of the Rb polarization. As the Rb rotates in the $\hat{x}$ -$\hat{y}$ plane, the signal goes from $\mathrm{P} = 1$ --→ $\mathrm{P} = 0$ --→ $\mathrm{P} = -1$ --→ $\mathrm{P} = 0$ --→ $\mathrm{P} = 1$. The measurements that we take consist of four different transmitted intensities. The first is the 100% transmission intensity found by going far off resonance (the intensity change as a function of detuning must be accounted for); secondly, the $P = 0$ intensity is found by blocking the pump beams; third and fourth are the intensities associated with the polarization rotation from $P = 1$ to $P = -1$. When the atoms are 100% polarized the 2π pulse signal size should equal the difference in transmitted intensity from 100% transmission (far off resonance) to $\mathrm{P} = 0$ (blocked pump beams) and the $P = 1$ and $P = -1$ levels should be centered on the $P = 0$ intensity level.

When implementing this measurement, the signal is not what we expect from simple analysis. The glaring error is that the $\mathrm{P} = 0$ intensity is not between the $\mathrm{P} = 1$ and P$= -1$ signals. Also, the calculated polarization is far from what we measure with Faraday rotation. We eventually came to realize that the signals we see are due to light interaction with the hyperfine levels. In spin temperature at high polarization, the atoms are pumped into the F=3 hyperfine level; however, if the pump detuning is near the F=2 hyperfine level where the electron spin is opposite that of the F=3 level, the polarization will be lower than the actual polarization due to the electron spins in

the respective F levels subtracting. Conversely, if the pump is close to the F=3 level, then the polarization measurement will be overestimated. This effect can be corrected:

$$\alpha \mathrm{P}_{\infty} = \frac{\mathrm{T(P)} - \mathrm{T}(-\mathrm{P})}{\mathrm{T(P)} + \mathrm{T}(-\mathrm{P})} \tag{6.2}$$

It's form can be seen in Fig. 6.7. The colors range from P$= 0.1 - 0.9$ where low polarization has the largest correction factor.

Needless to say, this measurement turned out to be more complex than we were expecting, so we temporarily turned to the non-ideal method of detecting the transmission of the pump to set the 2π pulses.

6.5.5 Method for Setting 2π Pulses

Because of the imprecision of pump transmission as a method of setting the 2π pulses,we eventually moved away from this method of direct detection to a more precise, indirect method. The other way to set the 2π pulse area when there is no access to P_y is to utilize the feature that an incomplete 2π rotation causes a non-zero B_z. The method is as follows: the fields are shimmed with the pulsing circuit unplugged. Once this is done, the pulsing circuit is plugged back in and B_z is monitored with an oscillating $\hat{x}$ field; this signal should start at a null point after the initial field shimming, but because of leakage currents in the pulsing circuit, this is not the case. The 2π pulse area is increased until B_z is re-nulled. This method is used to set $2n\pi$ pulse areas by adding area until the n^{th} null point is reached. One must be careful in using this method because there are also "null" points that correspond to $(2n-1)\pi$ pulses where the response of the magnetometer is zero. Using this method, the 2π pulses can be set accurately to a part in 3×10^4. We calculate this accuracy by knowing the noble gas resonance frequency. If the 2π pulse is set incorrectly, the bias field (B_z) and thus the resonance frequency of the noble gas will be off, so we calculate this number by measuring:

$$\frac{f_{\mathrm{Rb}}}{f_{\mathrm{Xe}}} = \frac{\gamma_{\mathrm{Rb}}}{\gamma_{\mathrm{Xe}}} \tag{6.3}$$

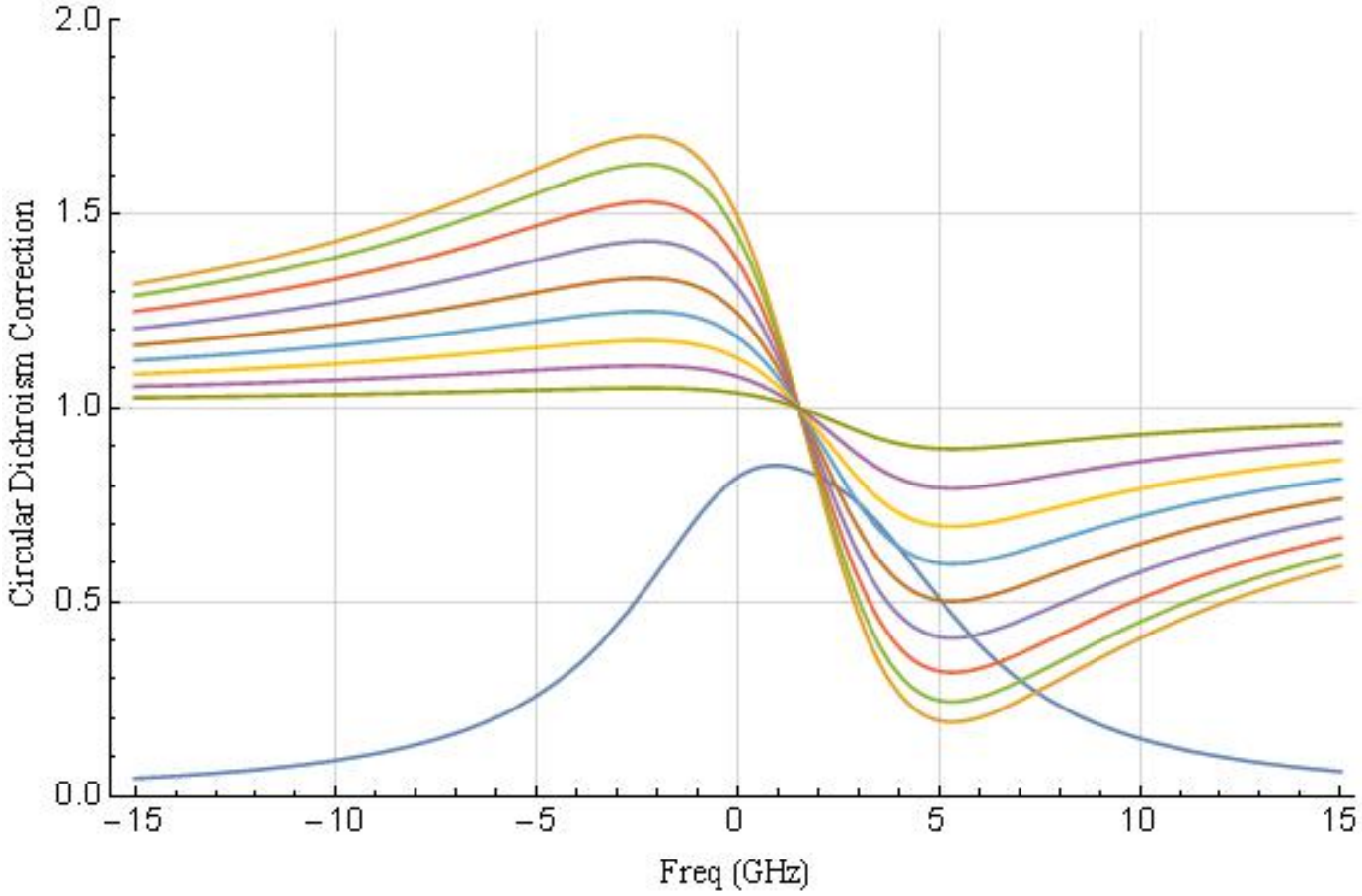

Figure 6.7: The correction needed for the circular dichroism measurement due to the asymmetry introduced from the hyperfine interaction is plotted as a function of pump detuning. The colors range from $0.1 - 0.9\%$ with low polarization having the largest correction factor.

The Rb frequency is known from setting the 2π pulse repetition rate with the FPGA, which is referenced to an atomic clock. The Xe resonance frequency is extracted from a synchronous spin exchange experiment.

For one random experiment chosen from many, the pulse rep rate was at 14kHz and we extracted a resonance frequency of 10.479Hz, which makes $\frac{f_{\mathrm{Rb}}}{f_{131}} = 1336.01$. The exact ratio of gyromagnetic ratios gives:

$$\frac{2\mu_B}{(2I+1)\gamma_{131}} = \frac{2 \times 1.39962}{6 \times 349.11} = 1336.37 \tag{6.4}$$

where μ_B is the Bohr magneton and I is the nuclear spin for ^{85}Rb, and γ_{131} is the gyromagnetic ratio of ^{131}Xe. This gives $\frac{\mathrm{measured}}{\mathrm{theory}} = 0.99973$ implying that with our current nulling methods we can set the 2π pulse area to a couple parts in 10^4.

6.6 Optics: Probe

6.6.1 Probe Optimization

We run the probe laser at about 30mW, but because of the nature of the cell we use, the maximum transmission through the cell and hence the detected power is typically less than half of that. The probe detuning is set to maximize response; therefore, with a signal applied along the magnetometer's sensitive direction, we scan the probe frequency to maximize the size of the signal. This optimal detuning changes with probe intensity and with [Rb]. It will also change depending on whether or not the probe contains any degree of circular polarization in it.

Circular polarization in the probe is seen as a pumping mechanism along the wrong direction with respect to the desirec optical pumping of the atoms and will result in a smaller signal and at times very strange looking signals. It also results in incorrect measurements of magnetometer relaxation rates, so it is vital that there is as little probe pumping as possible. Even though we clean up the probe polarization with a PBS before the cell, we have noticed some residual probe pumping effects. The easiest way to see probe pumping is to block the pump beams and apply large magnetic signals along the different axes. If any of the applied fields generate a signal, then we use a $\lambda/4$ plate placed after the PBS to null it out.

6.6.2 Atom Detection: Faraday Rotation

Detection of the atoms is done by Faraday rotation detection. The detection optics consist of a $\lambda/2$ plate, a polarizing beam splitter, and two photodiodes hardwired as a differential detector. For measurements of fast signals, such as the 2π pulses, we have a 75MHz bandwidth differential detector from Thorlabs. This detector is vital for direct detection of the 2π pulses and making alkali polarization measurements, but is difficult to free-space align; therefore, for noise measurements, where we want minimal intensity flutuations due to the laser wandering on the photodiodes and we don't need highbandwidth, we use large area photodiodes with a smaller bandwidth. There is also a saturation effect that we observe when using this high bandwidth detector; at high powers, the observed magnetometer response is no longer linear with probe intensity, i.e. a factor of 2 increase in probe power does not correspond to a factor of 2 increase in response. When we noticed this effect, the probe power we were using was close to the limit of the detectors; therefore, the probe intensity was reduced by about a factor of 5, which seems to fix the problem. We have since moved away from using the fast photodiodes entirely unless we need to measure a 2π pulse signal for a polarization calibration measurement. In this case, care must be taken to keep the photodiodes from saturating by operating at lower intensities.

The principle of Faraday rotation is that as the alkali spins rotate, they change the index of refraction of the vapor. This causes the linear polarization of the probe beam to rotate by an angle [Ledbetter et al., 2008]:

$$\phi = \frac{1}{4} l r_e c f n P_x D(\nu) \tag{6.5}$$

where l is the path length, r_e is the radius of the electron, c is the speed of light, f is the oscillator strength, n is the number density of the alkali, P_x is the alkali polarization. The last term

$$D(\nu) = \frac{\Delta\nu}{\Delta\nu^2 + (\Delta\Gamma/2)^2} \tag{6.6}$$

The vertical and the horizontal components of the probe polarization are then separated by the polarizing beam splitter and their difference is detected:

$$\phi = \frac{I_1 - I_2}{2(I_1 + I_2)} \tag{6.7}$$

where I_1 and I_2 are the respective intensities associated with the two polarization components. The factor of $1/2$ comes from the fact that the probe light first enters the $\lambda/2$ which rotates the polarization by 2ϕ. Knowing the response of the magnetometer in units of radians/Tesla allows us to compare magnetometer responses across different systems.

6.6.3 Other Detection Options

We have discussed another idea for detection that may help lower the $1/f$ probe noise that we believe is polarization fluctuations from hot air currents. This detection scheme uses two probe lasers tuned to either side of the optical transition and with orthogonal polarizations; this results in the common mode fluctuations (such as intensity noise) to only be second order effects, thus making the atom rotation signal dominate.

With a single beam, the differential detection $sig \propto \sin(2\phi)$ and incoming common mode polarization fluctuations look like atom signal rotations. If there are two probe beams with orthogonal polarizations at the same frequency, then with differential detection their signals would cancel. With two beams with orthogonal polarizations and equal and opposite detunings, the signal is only dependent on real magnetic fluctuations and common mode noise is of second order.

6.7 System Optimization

6.7.1 Nulling Stray Magnetic Fields

Before all measurements with the magnetometer are made, the stray fields must be nulled. This is best done without parametric modulation or 2π pulses, but it is useful, when using a cell with noble gas nuclei in it, to apply pump polarization modulation to keep the noble gas from becoming polarized and adding $\hat{x}$ field. The procedure goes as follows:

- Balance the photocurrents in the detector with the pump beams blocked
- Null out any probe pumping effects as described above

- Adjust the sensitive direction field (B_y for $\hat{z}$ detection and B_z for $\hat{y}$ detection) until at zero
- For $\hat{z}$ detection: Apply an oscillating B_x at a frequency within the magnetometer bandwidth and at an amplitude within the magnetic width; zero any resulting signal with B_z. Sometimes the signal will not pass through zero, but will instead phase shift in which case, center it on the phase shift.
- Apply an oscillating B_z and null the resulting signal with B_x in the same manner as above
- Iterate the previous three steps until the signal is zero and there is no response to applied B_x or B_z.

This procedure follows the magnetometer response equations outline in Sec. 2.1.

6.7.2 Alignment

It is vital that the pump and probe are perpendicular to each other and that each beam is well aligned with its respective axis of the magnetic field coils. If this is not the case then the light will pump the atoms along a direction that is not $\hat{x}$, causing precession about uninteded axes. Misalignment can easily be seen by looking at the raw photodiode signal of the probe along $\hat{z}$ while the 2π pulses are on. A misalignment between the probe and the 2π pulse coils will result in an atom signal at the 2π pulse frequency. These signals can be large, but if calibrated to polarization units, they are quite small in comparison to the polarization along $\hat{x}$. This would be a convenient method of alignment if we had a means of making fine angular adjustments to the beam directions. As it now stands the lever arms on both the pump and the probe are much too long for aligning with the atoms as a reference.

A few of the measurements that could be sensitive to the alignment are:

- Apparent alkali field frequency shift
- Xe 1f signal. This is a signal at the first harmonic of the nuclear precession. It can be caused by a non-zero B_y, but with both misalignments and non-zero AC Stark shifts, there is also a 1f signal that cannot be nulled with B_y. In this case, the AC Stark needs to be re-nulled

or if it is very bad, the alignment checked. There is also the unexplored hypothesis that it is actually a Xe signal at 1f. Some inconclusive studies of the 1f component as the Xe resonance is scanned have been made.

- Poor cross axis rejection when using parametric modulation to detect both B_z and B_y

Because we cannot actively null any of these signals, the alignment is instead done through a painstaking process of using irises and beam cubes. The pump and the probe alignment is done in either one of two ways. The first is carefully aligning the probe beam with respect to the screw holes on the table with the help of irises. A beam cube is then inserted in its path and in the path of the pump. Care is taken to ensure that the probe beam is perpendicular to the face of the beam cube by aligning the beam cube with the table holes as well. The transmitted/reflected probe and the reflected/transmitted pump are then overlapped in the far field. This is the less reliable of the two methods because when the field coils are inserted there is no way to know if the beam is parallel to its respective field coil axis.

Therefore, the better method of alignment is to remove the cell and the shield entirely and prop the magnetic field coils up at the height of the shield ports; pinholes that are centered on the windows of the cell oven are then affixed to the coil frame. Removing the shield facilitates the alignment, since with it in place there is no good way to see where the light hits the pinholes. The alignment of the pumps and the probe is adjusted such that the maximum amount of light goes through the pinholes. Because the field coils are designed and built with the three axes perpendicular to each other, aligning the lasers with the coils themselves should ensure that the pump and the probe are perpendicular and that the two pumps are parallel. The alignment will be as good as the alignment of the pinholes. The main issue with this method of alignment is the vertical placement of the coils outside the shield. There is no height adjustment for the coil frame and it already sits high with respect to the light access ports, so it is vital that the height is correct before aligning the lasers. The best way to accomplish this is to do a rough alignment with the pump and probe and mark where the probe light hits the coil frame, once the shield is taken out, the position can then be readjusted with respect to these marks.

Another issue is that the length over which the light is aligned when using the pinholes on either side of the coil frame is only several centimeters. The alignment is only as good as the horizontal and vertical alignment of the pinholes and could get better as the length over which this is done increases. So instead of aligning the beams using pinholes that are afixed to the coil frame, this alignment could also be done by using irises on either side of the shield. The benefit of this method, besides a longer path length, is that it is not necessary to remove the shielding, but it is still necessary, due to the distorting nature of the cell, to remove the cell.

The largest uncertainty in any of these alignment procedures is the fact that even if the lasers are well aligned without the cell in place, once it has been put in, the distortion of the light within the cell might be great enough to negate the alignment efforts. The extent of the effects of this distortion will be unknown until we put in a cubic cell.

6.7.3 Density Optimization

The alkali density and the detuning of the pumps are set to ensure optimum Rb polarization of about 50% at high density. This is done by first decreasing the density to approximately $2 \times 10^{12}/\mathrm{cm}^3$ where we can obtain high Rb polarization. The pump detunings are then individually set to give between $70\% - 80\%$ polarization on either side of resonance; this should be approximately equally detuned on either side of the optical transition where the AC Stark shift magnitude should be equal. The AC Stark nulling is then completed following the procedure in the above section. Once this process is complete, the density is increased while monitoring the transmission of circularly polarized pump light until 10% is being transmitted. It is preferable to not block one side of the pump while monitoring the transmission, so a glass coverslip pick-off is used; in this way, the majority of the pump light is incident upon the cell from both sides. This procedure ensures that at the entrance to the cell, the polarization is at least 70% and falls to about 50% in the middle.

6.8 Rb Magnetometer Characterization Measurements

This section will cover the measurements needed to characterize the alkali magnetometer. The characteristic measurements for Xe are described in Sec. 4.1.

6.8.1 Polarization

The alkali polarization is measured via the 2π pulse signal seen in Fig 6.8. The benefit of the 2π pulse signal is that it quickly transfers polarization from along the pump direction to along the probe direction on a time scale that is fast compared to the relaxation mechanisms, which results in an accurate calibration of signal size to alkali polarization. This measurement can also be done with a $\hat{z}$ probe, in which case pulsing must be along $\hat{y}$ instead of $\hat{z}$. The polarization of the alkali is

$$P = \frac{R}{R + \Gamma_0} \tag{6.8}$$

and the pumping rate R is proportional to the intensity of the pump beam. Therefore, a calibration of the voltage of the 2π pulse signal to polarization is made by measuring the 2π pulse signal amplitude as a function of pump light intensity and extracting a 100% polarization voltage value:

$$V_{2\pi} = \frac{V_{0,2\pi} R}{R + \Gamma_0} \tag{6.9}$$

This measurement must be taken at low pulsing frequency to avoid relaxation as described in Sec. 2.4. The extracted value $V_{0,2\pi}$ can then be used to find P_x by dividing any 2π pulse signal by it. It can also be used to calibrate the polarization along the probe direction.

These measurements are best done at low density where the polarization is high and the fit to Eqn. 6.9 is reliable. The low density calibration can then be multiplied by the ratio of densities to extract a high density calibration. When doing this measurement at low density for the purposes of a high density calibration, the detuning of the probe must be at the desired high density detuning since the calibration changes as a function of probe detuning (although it can easily be done, we never calibrated the signal size as a function of probe detuning).

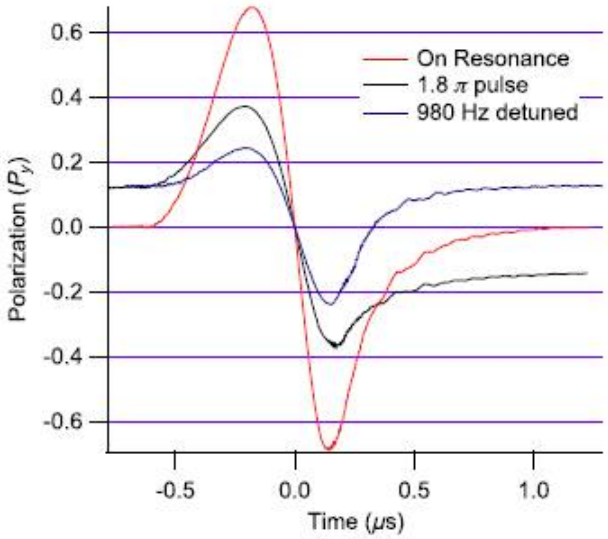

Figure 6.8: The 2π pulse signal as seen with a $\hat{y}$ probe. A 2π pulse signal can also be seen detecting P_z when the pulsed field is applied along $\hat{y}$. The red trace corresponds to a well tuned 2π pulse. When the circuit was AC coupled and a resonance condition between the applied B_0 and the pulsing repetition rate had to be met, the blue would correspond to either a detuned pulse frequency or a change in B_0. Now that the circuit is no longer AC coupled, the blue trace only corresponds to a change in the DC shim of the sensitive direction. The black trace corresponds to a non-optimized 2π pulse area for AC coupled pulses.

At high density, there are optical thickness issues where the polarization drops off too quickly. Sometimes the optical thickness can be worked around by detuning the pumps further from resonance. A characteristic feature of optical thickness adversely affecting this measurement is if the fit gives an offset to R (the relative intensity); i.e. the polarization signal goes to zero before the intensity does.

6.8.2 Γ', Γ_0, R

Since $\Gamma' = R + \Gamma_0$, R and Γ_0 are extracted from measurements of Γ'. The fundamental relaxation rate (spin destruction, wall relaxation, etc.) is the relaxation rate when $R = 0$, so to find it, we take measurements of Γ' as a function of decreasing R (decreasing pump power) and the extrapolate to $R = 0$ to get Γ_0. Once Γ_0 is known, then it can be subtracted from any Γ' measurement to obtain R.

Because of complications due to the slowing down factor, the measurement of Γ' is best done as a steady state experiment. This is done by scanning the magnetic width of the magnetometer. Without the 2π pulsing on, zero the SERF magnetometer then scan the sensitive field direction. Fit the resulting dispersive waveform to

$$\mathcal{D} = \frac{\Delta}{1 + (\frac{\Delta}{\text{width}})^2} \tag{6.10}$$

where the width parameter is Γ' in magnetic field units. To convert from field units to the relaxation rate, $\Gamma' = 2\pi\mu_B \times \text{width}$. Since this is a steady state experiment, there is no slowing down factor. In a cell containing noble gas, this measurement is best done at low [Rb] to minimize the effect of collisions with the noble gas.

6.9 Magnetometer Noise Measurement Procedure

A noise spectrum is the Fourier transform of the signal of interest; in our case, this is the magnetic signal along the sensitive direction of the magnetometer. This means that the Fourier transform in raw signal units must be calibrated to field units taking into account the frequency

response; this bandwidth is determined by the relaxation time of the magnetometer. In order to measure the bandwidth, an oscillating field of known amplitude (in field units) at frequency f is applied along the sensitive axis. The magnetometer response (in raw signal units) is then measured as a function of f and fit to a Lorenztian:

$$\mathrm{Lor} = \frac{1}{\sqrt{1 + (\frac{f-f0}{\Gamma})^2}} \tag{6.11}$$

where Γ is the bandwidth. Once we have the bandwidth information where the response is converted to $V_{\mathrm{sig}}/\mathrm{Gauss}$, we Fourier transform a time series of the signal of interest, scale it, then divide by the bandwidth response function. The procedure for scaling the FFT in IGOR can be found in Appendix C.

Chapter 7

Circuits

This chapter describes several of the circuits we developed to meet the requirements of pulsing large magnetic fields as well as measuring the resulting signal.

Developing a circuit to meet the requirements of the 2π pulsing was a challenge. The issue was that the circuit needs to drive high currents through a coil with a large inductance in $< 5\mu$s. The coil is high inductance because of the large amount of uniform field it needs to produce over$1\mathrm{cm}^3$. Fortunately, Mike Bulatowicz was able to design a set of coils that reduced the inductance a factor of 7 (down to 32μH), which only requires 15V to drive a $2\mu s$ pulse (instead of 100V).

We developed two circuits for the purposes of driving this large coil, so in this chapter I will present the preliminary design and discuss the concerns that we had with it and our reasons for developing a second circuit. Chapter 5 Section 5.2 will go into more depth about noise issues we faced that motivated the second design.

There were also a couple of attempts at a new circuit design for quiet pulsing that did not succeed; I will describe these in less detail.

7.1 Circuit Idea 1

The circuit diagram for Circuit 1 is shown in Fig. 7.1. The switch M1, which is driven by a MOSFET driver, remains open until it is triggered closed by a function generator that controls both the width and the repetition rate of the pulsing. Our particular function generator, AFG2002C from Tektronix, produces pulses with pico-second stability, which is better than what can be produced by many FPGAs. Any modulation of the pulse frequency (as required in dual species pumping;

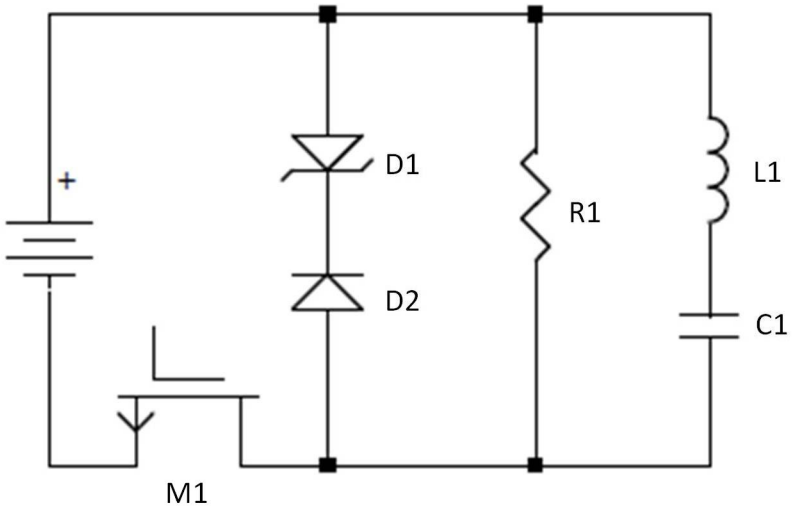

Figure 7.1: The first circuit idea. Voltage is dropped through L1 when the switch is closed and the back emf once the switch closes decays through the 150V zener diode D1.

see section 8.2) or phase synchronization (as required by the parametric modulation schemes; see Sec. 5.3) is controlled by the FPGA that generates the frequency trigger for the function generator. The switch is only closed for approximately half of the pulse width. Once it is opened, the sudden change in current through the inductor generates a large back EMF whose voltage is limited by D1, a 150V zener diode. The current then decays through D1 until the voltage is less than the zener breakdown voltage after which it completes its decay through R1. The voltage drop across the inductor during this process is integrated and converted to field according to

$$V = L\frac{dI}{dt} = Lk\frac{dB}{dt} \tag{7.1}$$

where $k = dI/dB$ is the pulsing coil's conversion from field to current. This results in the sample field pulse shape shown in Fig. 7.2. The rate of the current buildup is controlled by the width of the pulse, but the slope of the decay of the current is fixed by the zener. The area under the curve corresponds to a 2π rotation:

$$2\pi\gamma_{\mathrm{Rb}} \int B dt = 2\pi \tag{7.2}$$

Most of the decay is governed by the diode, but R1 must be carefully chosen so that the remaining current decay is smooth and fast. A resister that is too small will cut short the decay through the zener, which significantly lengthens the pulse. A resister that is too large will result in oscillations after the pulse (Fig 7.2). The optimum resistor value depends on the inductance of the pulsing coils. I only have two data points that correspond to a 160ns ($R = 200\Omega$ and $L = 32\mu$H) and 300ns ($R = 750\Omega$ and $L = 225\mu$H) time constant since we only studied this problem with two field coil designs.

7.1.1 AC Coupling Options

As seen in Fig. 7.1, there is a capacitor C1 at the base of the field coil L1. This AC coupling capacitor was used in the experiments described in Chapter 2, but it has subsequently been taken out. The preliminary AC coupling method, however, was not a capacitor, but a transformer. This method was disposed of fairly early on due to the difficulty of making a transformer that impedance

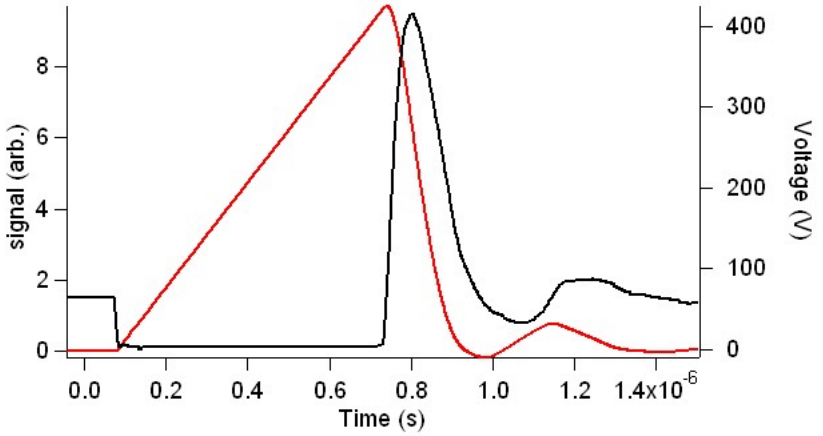

Figure 7.2: The black trace is the voltage at the bottom of the inductor during a 2π pulse, while the voltage at the top remains constant at the applied V_p. The red trace is the integral of the voltage drop across the inductor and corresponds to the current (field) through the coils. The pulse is asymmetric due to the decay being governed by the zener diode voltage. There are oscillations at the end of the pulse due to the resistance value being chosen incorrectly.

matched the inductor we were trying to drive. We had poor coupling efficiency and poor power transfer, so we moved to AC coupling with a capacitor. The capacitor must be large so that the decay of charge through the circuit in between pulses is negligible, which means that we chose the largest capacitor available without resorting to electrolytic capacitors; this is a 30μF tantalum capacitor.

With the AC coupling capacitor in place, the circuit requires a much larger voltage to drive a 2π pulse. Because the capacitor acquires charge during the pulse and does not fully discharge between pulses, the required applied voltage increases as pulse duty cycle increases.

7.1.2 Frequency and Pulse Width Dependence

The circuit and its ability to make a 2π pulse is very sensitive to the pulse repetition rate. A 0.024 V change in the applied 2π pulsing voltage is equivalent to a 1kHz shift in the 2π pulsing frequency. Figure 7.3 shows this dependence. It also shows a strange feature of the circuit where the required voltage suddenly increases around 10kHz. Also to be noted on the plot is the dependence of the $\hat{y}$ shim field on 2π pulsing voltage. All these features are unique to this particular configuration of the circuit ($R = 200\Omega$ and $L = 32\mu$H) and may change depending on the inductance of the coil, the resistance, etc.

7.1.3 Pulse Area Stability and Other Concerns

The main concern with this circuit is the pulse stability. If there is a fluctuation in pulse width, this will lead to a fluctuation in $\hat{z}$ field, as well as a fluctuation of P_y; this latter effect is discussed more in Sec. 5.2 in regards to polarization noise. The necessary pulse stability to obtain a reasonable noise level of $10^{-13}T/\sqrt{\text{Hz}}$ was calculated in section 5.2 as $\sigma_p = 10^{-6}$ rotations which is equivalent to 10 pico-seconds pulse width stability or micro-Gauss pulse amplitude stability; all of these stability requirements are very stringent. We were concerned that the pulses produced by this circuit would not be that stable enough for our noise requirements, so we designed Circuit 2, which should have well defined pulse parameters.

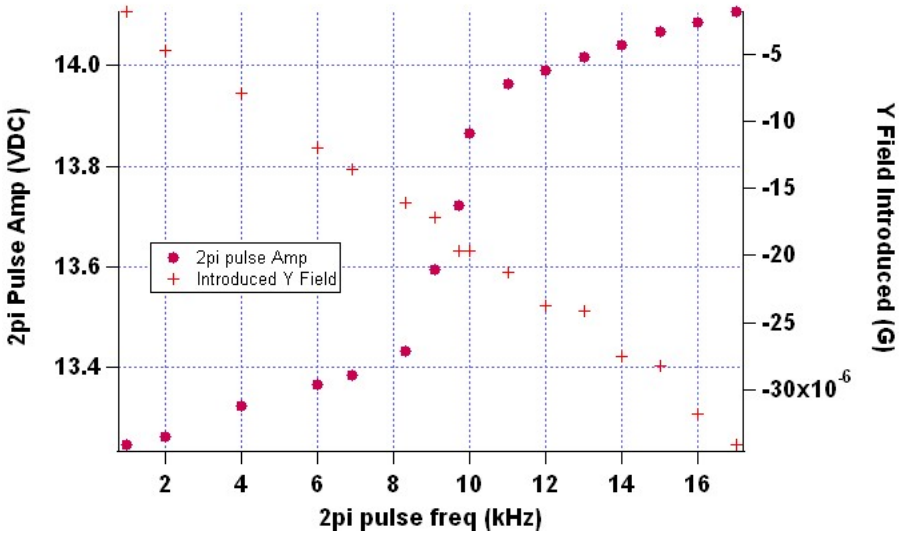

Figure 7.3: As the 2π pulse frequency changes the pulse area changes, which means the voltage required to make a 2π pulse changes. This results in a change in the $\hat{z}$ shim field and will shift the NMR resonance. Also shown on this plot is the change in the B_y shim as the pulse frequency changes.

Another concern that cropped up regarding this circuit is the fact the the pulses applied are asymmetric. If one side of the pulse is shorter than the other, then the time averaged alkali spin is pointed more in one direction than the other. The pulse can be forced into being symmetric by an appropriate choice of the zener diode, which governs the rate of the current decay. However, when we did this, we noticed no change in behavior.

A third issue, is that this circuit seems to be limited to total pulse widths of 1.5μs for reasons we could never figure out. There was always a tail that would lengthen it no matter how short the first part of the pulse was made.

7.1.4 Circuit Parts List

See Appendix D.

7.2 Circuit Idea 2

7.2.1 Reasons to Design a New Circuit

Because of the concern about the stability of the pulse area, we decided to design a circuit that delivers a very specific amount of charge each time a pulse is triggered. Capacitive discharge is the easiest means for accomplishing this. Figure 7.4a shows the basic idea of this circuit. The idea is that when S2 is open and S1 closed, C1 will accumulate $Q = V/C1$ over a time $\tau = R1C1$. When S2 is closed and S1 is open, the capacitor will discharge through the inductor. The diode D1 keeps any charge from flowing the wrong direction through the circuit. The resulting pulse of current through L1 (Fig. 7.5b) is half a sine wave with width determined by $\tau_p = L/C$. The full 2π rotation is in turn set by the applied voltage which controls the amount of charge buildup.

7.2.2 Design Idea

The implementation of this circuit resulted in Fig. 7.4b. In order to prevent current from flowing through the coils directly from the power supply during a pulse, we insert M1, which is a p-type MOSFET. Driving the gate of this MOSFET turns out to be slightly complicated since, in order to turn on, the gate needs to be 10V below the source. In our case, the source voltage

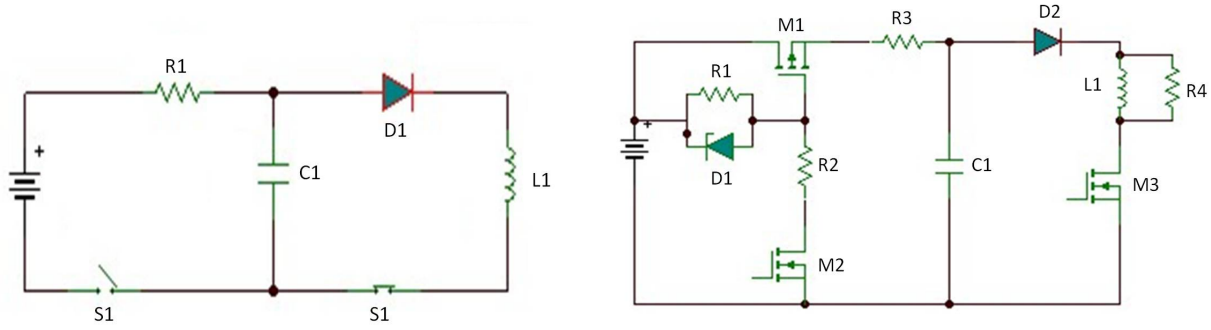

(a) Basic circuit idea

(b) Full circuit

Figure 7.4: The diagrams for the basic capacitive discharge circuit (a) and the implemented capacitive discharge circuit (b). The main difference is the way in which we implement the switches.

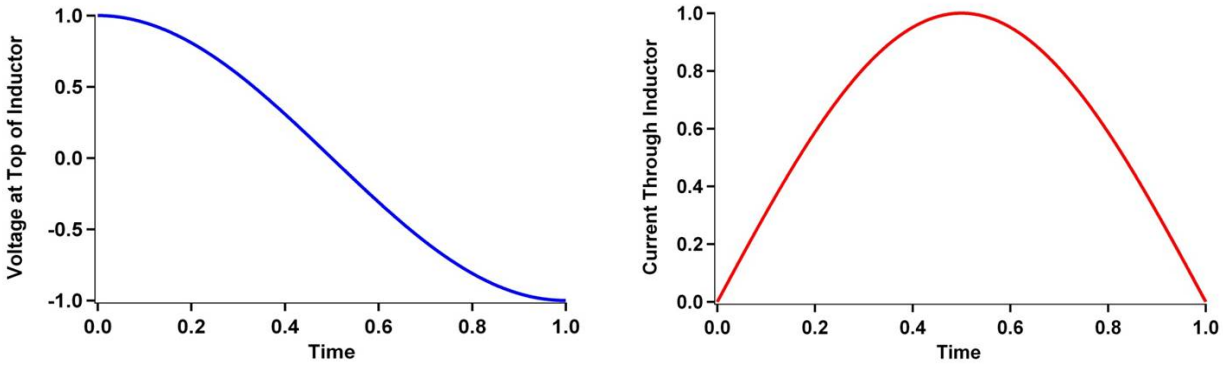

(a) Voltage at the top of the inductor

(b) Current through the inductor.

Figure 7.5: The pulse created by Circuit 2. The time starts when the switch at the bottom of the inductor closes and the capacitor is fully charged. This means that the voltage at the top of the inductor is one diode drop lower than V_C. The figure on the right is the integral of (a) and is the current through the inductor.

changes as a 2π pulse is set. To keep the gate perpetually 10V below the drain, we insert a 10V zener diode between the source and the gate. The timing of M1's gate is then controlled by M2; when M2 is closed, the gate voltage of M1 is 10V below its source voltage, so M2 is also closed and C1 charges. The presence of R1 and R2 control the current flow. When M2 is open, M1 is also open so that current cannot flow from V_p through L1. Because there is a time constant associated with turning M1 off due to its internal capacitance, it must be nominally turned off well before M3 is turned on, but not so long as to allow too much charge to decay from C1.

The capacitive discharge portion of the circuit is the same as described above except for the addition of R4, which controls ringing through L1 after M3 is turned off.

There are a couple timing issues with the circuit's MOSFETs that were never tracked down and solved. The issue is that M2 must be turned back on at the same time M3 is turned off, whereas we originally thought that we would need to wait a short while after M3 turns off to turn on the charging portion of the circuit. This may be due to the high current through M2 during the charging portion of the circuit. The interaction between M2 and M3 might be mitigated if we could better isolate the two portions of the circuit.

7.2.3 Circuit Performance

The purpose of designing this circuit was to reduce noise that we hypothesized was due to pulse width instabilities. Unfortunately, we saw no improvement once this circuit was implemented. This seems to indicate that any pulse instability problem we may have is currently overshadowed by another noise source.

7.2.4 Circuit Parts List

See Appendix D.

7.3 High Voltage Op Amp Circuit

In the pursuit of a circuit that generates stable pulses, we came up with another interesting idea that was never fully implemented.

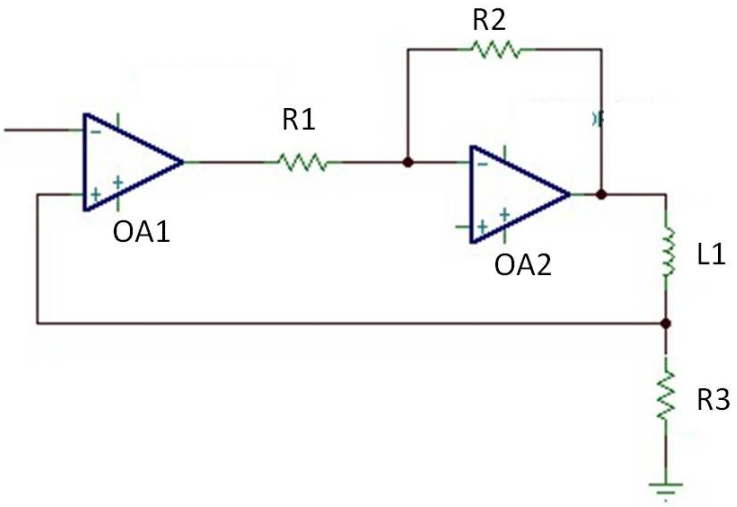

Figure 7.6: The basic high voltage op amp circuit that works by controling the current through R3 by controlling the shape of the pulse. It also compensates for noise through feedback on the pulses.

The circuit is shown in Fig. 7.6. The idea is to control the shape of the voltage pulse across $\mathrm{R_L}$ with feedback, and thus control the current through the inductor. The pulse will be stabilized since any fluctuation in the current through the inductor will be registered as a deviation from the inverting input of OA1, so the output will correct for it. Therefore, in addition to controlling the pulse shape, the voltage noise and hence the current noise at $\mathrm{V_+}$ will be suppressed:

$$V_1 = G(V_+ - V_-) \tag{7.3}$$

$$V_+ = \frac{R_L}{R_L + j\omega L}(v_n - \frac{R_2}{R_1}V_1) \tag{7.4}$$

$$V_+ = \frac{\frac{R_L}{R_L+j\omega L}v_n + \frac{R_L}{R_L+j\omega L}\frac{R_2}{R_1}GV_-}{1 + \frac{R_L}{R_L+j\omega L}\frac{R_2}{R_1}GV_-} \tag{7.5}$$

for large G the noise is greatly suppressed:

$$V_+ = \frac{R_2}{R_1}\frac{v_n}{G} + V_- \tag{7.6}$$

This circuit worked well when driving small inductive loads. When driving large inductive loads, however, OA2 needs to be a high power op-amp and bandwidth limits the performance.

7.3.1 Circuit Parts List

See Appendix D.

7.4 Pulse Gating Circuit

When using the lock in to demodulate the parametric modulation signal, it is necessary to suppress the signal from the 2π pulses, because they saturate the lock in input. This of course is obsolete (almost) with a $\hat{z}$ probe. In this circuit, pictured in Fig 7.7, the MOSFET is triggered off for slightly longer than a 2π pulse. In order to minimize transients on the resulting signal, the second part of the circuit works to hold the signal constant while the pulse is gated out. There are still transients, but the amplitude of the signal that appears at the 2π pulse frequency is greatly suppressed.

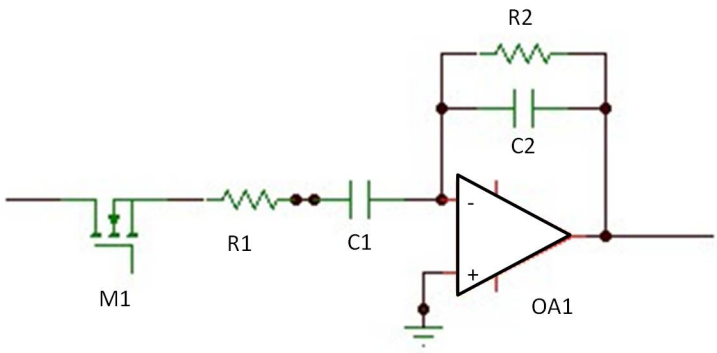

Figure 7.7: The circuit designed to eliminate the large signals due to the 2π pulsing when using lock-in detection of P_y.

Chapter 8

Dual Species Operation

In this section, I will describe the method for exciting two noble gas species simultaneously. The gyromagnetic ratios of the two Xe isotopes differ by a factor of 3.373 [Brinkmann, 1963], so using a single frequency alkali polarization modulation is not possible. We therefore had to devise a scheme that would couple the two species and synchronously pump them simultaneously, without excessive loss of signal. The results described here are only preliminary.

8.1 Choice of Noble Gas

The choice of noble gas is determined by potential signal to noise ratio, quadrupole behavior, and relaxation times. Our original idea was to use ^{129}Xe and ^{3}He as the two isotopes since both are spin-1/2 and therefore do no have the quadrupole interaction. However, as the experiment progressed and we did intensive studies of ^{131}Xe, we could find no indication of a quadrupole interaction. Future work should intentionally test for its presence, but we have looked at many FID signals that show no evidence of quadrupole effects. This has led us to postulate that, due to our unique method of pumping the noble gas, there will be no first order quadrupole interaction. If this is the case, then there is essentially no reason to choose ^{3}He over ^{129}Xe. It is true that the relaxation times in ^{3}He are potentially much longer than they are in Xe, but the Fermi contact interaction is also 100 times smaller. For these reasons and for ease of use, these preliminary studies have concentrated on Xe.

There is also the interesting question of how much noble gas pressure is ideal for the operation of the oscillator. A rough approximation indicates that the Faraday rotation signal should be independent of [Xe]. This means we could operate with low [Xe] which would allows us to go to high [Rb] to increase the signal. The approximation begins with the signal proportional to the Faraday rotation of the Rb into the probe direction:

$$\phi \propto [\mathrm{Rb}P_z \tag{8.1}$$

where

$$P_z \approx \frac{P_x \Omega}{\Gamma_{\mathrm{Rb}} + R} \tag{8.2}$$

and we take the field $\Omega \propto [\mathrm{Xe}]P_{\mathrm{Xe}}$ as the magnitude of the Xe field. This results in:

$$\mathrm{signal} \propto \frac{[\mathrm{Rb}]P_{\mathrm{x}}[\mathrm{Xe}]P_{\mathrm{Xe}}}{\Gamma_{\mathrm{Rb}} + R} \tag{8.3}$$

Substituting in

$$P_{\mathrm{Xe}} = P_{\mathrm{x}} \frac{\Gamma_{\mathrm{SE}}}{\Gamma_{\mathrm{SE}} + \Gamma_{\mathrm{wall}}} \tag{8.4}$$

and

$$P_{\mathrm{x}} = \frac{R}{R + \Gamma_{\mathrm{Rb}}} \tag{8.5}$$

the signal maximizes at $R = \Gamma_{\mathrm{Rb}}$. Knowing that the Rb relaxation rate is dominated by spin exchange collisions with the Xe, we have $\Gamma_{\mathrm{Rb}} \approx k_{\mathrm{SE}}[\mathrm{Xe}]$ and $\Gamma_{\mathrm{SE}} = k_{\mathrm{SE}}[\mathrm{Xe}]$ we see that the result:

$$\mathrm{signal} \propto \frac{[\mathrm{Rb}][\mathrm{Xe}]}{8k_{\mathrm{SE}}} \frac{\Gamma_{\mathrm{SE}}}{\Gamma_{\mathrm{SE}} + \Gamma_{\mathrm{wall}}} \tag{8.6}$$

has no dependence on the Xe density at a fixed [Rb]. Knowing this, it might be beneficial to move to lower [Xe], which would allow us to increase the temperature, i.e increase [Rb], by the same amount [Xe] is decreased. This would give us more signal and higher Xe polarizations by avoiding the additional relaxation losses that result when the [Rb] is increased in the presence of large amounts of Xe. Since making this conjecture, however, we have learned several sobering things. First is the X-factor in ^{129}Xe. Since its wall relaxation rate increases so dramatically as a function of [Rb], its polarization is limited to $\approx P_{\mathrm{Rb}}/3$, so we will not gain significantly in its polarization, whereas there is no significant X-factor for ^{131}Xe, so its polarization should increase.

The other issue that presents itself upon turning up the [Rb] is the broadening of the linewidth due to the alkali field which increases in proportion to the [Rb]. At higher density, the alkali field will be quite large, which means that we are going to need to apply a large compensating field to mitigate its effects. It is not immediately apparent that this will cause us issues, but at some point the additional magnetic field will begin degrading the magnetometer's performance. We certainly do not want to apply a field that is greater than the magnetic width of the magnetometer, which, assuming everything scales as it should, would be the case if we increased the [Rb] a factor of 10 as we originally hoped.

8.2 Dual Species Pumping Scheme

For dual species pumping we utilize extensions of sub-harmonic pumping that was discussed in detail in section 3.3. One way to pump both isotopes is to vary the bias field so that the first harmonic of ^{131}Xe and the third subharmonic of ^{129}Xe are on resonance for part of the time. Looking at the simple scheme of modulating the DC $\hat{z}$ field to couple these two resonances, then the frequency difference between the third subharmonic of ^{129}Xe and the first harmonic of ^{131}Xe would require an 8mG oscillation in a 0.053 mG bias field. This requirement is far above the magnetometer's magnetic width of 1.5 mG, so it would introduce non-llinearities into the detection. Therefore, instead of modulating the field itself, we can modulate the frequency of the 2π pulses. As was discussed in Chapter 3 the 2π pulse frequency sets the bias field magnitude, which means that modulating the pulses has the same effect as modulating the $\hat{z}$ field, but avoids changing the actual field amplitude. This means that the alkali are unaffected by a modulation of the 2π pulse frequency since an alkali 2π pulse is the same as a 0π pulse.

The frequencies that govern this coupling are defined by $\gamma_{129}B = 3f + f_0$ and $\gamma_{131}B = f - f_0$ where B is the bias field defined by $B = B_{\mathrm{bias}} = f_{\mathrm{Rb}}/\gamma_{\mathrm{Rb}}$. The two frequencies that are now "pumping" the Xe are f which is the pump modulation frequency and f_0 which is the rate of the 2π pulse modulation. The depth of the 2π pulse modulation can be adjusted to maximize the response to both the isotopes. In more mathematical detail, we start with the time evolution of the noble gas polarization in the transverse plane:

$$\frac{dK_+}{dt} = (-i\gamma B + \Gamma)K_+ + R \tag{8.7}$$

where $B = B_0 + B_1(t)$ and B_0 is the bias field and $B_1(t) = B_1 \cos(\omega_1 t)$ is the modulation applied to the 2π pulses. We can then make $K_+ = A_+ e^{-i2\pi\gamma B_1 t}$ and Fourier expanding $R = \sum_p R_p e^{ip\omega t}$ and $e^{-i\phi_1} = \sum_q J_q e^{iq\omega_1 t}$

$$A_+ = \frac{R_p J_q e^{i(p\omega + q\omega)t}}{\Gamma + i(\omega_0 + p\omega + q\omega_1)} \tag{8.8}$$

which is in the rotating frame; if we go back to the lab frame then we pick up another J

$$K_+ = \frac{R_p J_q e^{i(p\omega + q\omega_1)t}}{\Gamma + i(\omega_0 + p\omega + q\omega_1)} e^{-i\omega_1 t} \tag{8.9}$$

$\rightarrow$

$$K_+ = \frac{R_p J_q J_s e^{i(p\omega + q\omega_1)t}}{\Gamma + i(\omega_0 + p\omega + q\omega_1)} e^{-is\omega_1 t} \tag{8.10}$$

There are two options for doing the 2π pulse modulation: sine or square wave. We have chosen the square wave modulation because we are better able to compensate for the error in the 2π pulsing circuit that is generated when the pulse repetition rate changes (see details in section 7.1.2). Depending on which is chosen, the Fourier amplitude changes. For sinusoidal modulation, the Js are Bessel functions, while for the square wave modulation

$$J = \frac{1}{T_1} \int_0^T e^{i\phi_1} e^{-iq\omega_1 t} dt \tag{8.11}$$

where

$$\phi_1 = 2\pi\gamma B_1 \begin{cases} t & t < T_1/2 \\ T_1 - t & t > T_1/2 \end{cases} \tag{8.12}$$

Integrating Eqn 8.11 we get the functions as shown in Fig 8.1. The traces correspond to what Bessel function looks like and what the square wave integral looks like. As can be seen they are fairly similar.

With a square wave modulation, we have another free parameter to vary and that is the duty cycle of the wave. As has been the case for everything we have done, the Fourier amplitude loss decreases as the duty cycle decreases. Changing the duty cycle changes Eqn. 8.12 to:

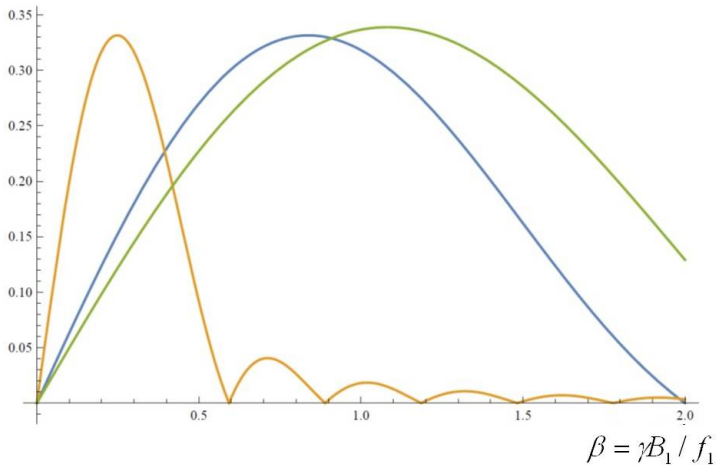

Figure 8.1: The green trace is the Bessel function for sinusoidal modulation for ^{131}Xe. The blue trace is with square wave modulation. The yellow is square wave modulation with $\beta \rightarrow \gamma_{129}/\gamma_{131}\beta$ for ^{129}Xe

$$\phi_1 = \frac{2\pi\gamma B_1}{2} \begin{cases} \frac{t}{d} & t < dT_1 \\ \frac{T_1 - t}{1-d} & dT_1 < t < T_1 \end{cases} \tag{8.13}$$

Figure 8.2 shows the above integral 8.11, with the duty cycle at 10%.

If we go one step further and use a demodulation scheme that can eliminate the additional reduction due to J_0, by demodulating with the exact signal waveform, then we have what is seen in Fig. 8.3. In this case, we pump the ^{131}Xe on resonance (with J_0) and the ^{129}Xe with the J_1 which gives us very little loss on either isotope except for the factor of three in the case of ^{129}Xe due to the third subharmonic pumping.

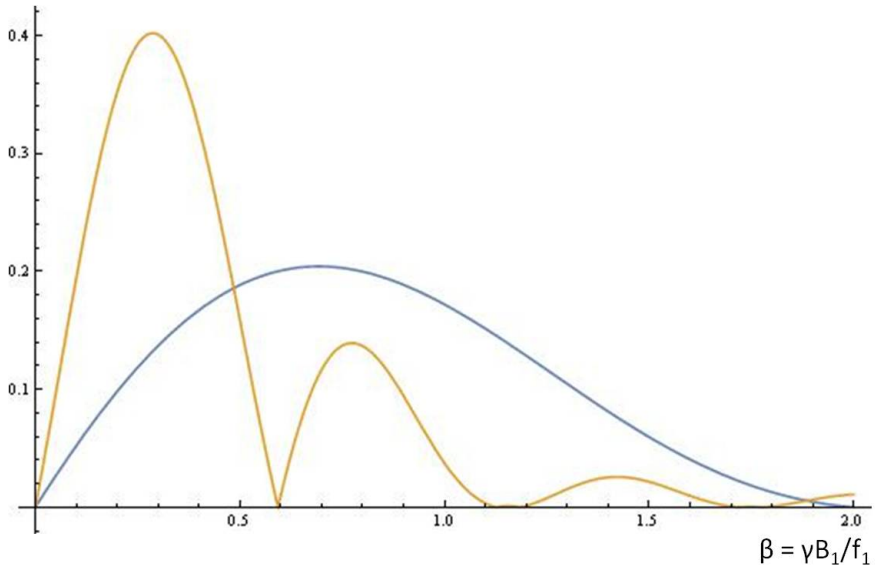

Figure 8.2: If the modulation of the 2π pulses is not a 50/50 duty cycle, then the amplitudes of the Fourier components will increase. This figure is for a 10% duty cycle.

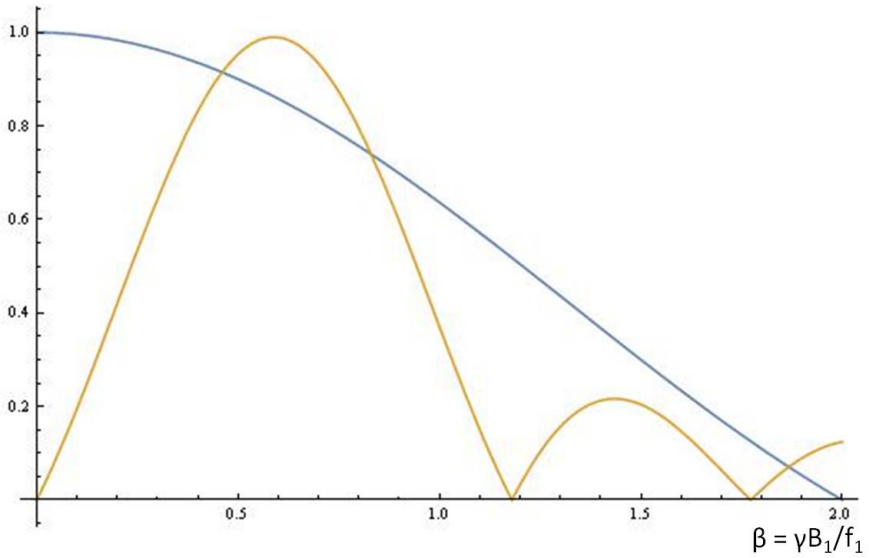

Figure 8.3: If, in addition to the duty cycle, the signal is demodulated with the phase of the modulation waveform taken into account, then the additional J_0 loss is regained.

8.3 Issues Encountered

The first issue we encounter is that the 2π pulsing circuit requires a different applied voltage for different 2π pulse frequencies. The error is about $0.024\mathrm{V_{app}/kHz_{Rb}}$. When the depths we use to modulate are on the order of 1kHz, this means we are shifting the Xe resonance by a significant amount with the modulation on. The first simple solution is to apply a compensating field along $\hat{z}$ to cancel what the 2π pulse modulation adds in. This becomes a problem when access to the $\hat{z}$ coils for other purposes is necessary. A second option is to vary the pulse width to make up for the 2π rotation error. Upon calibrating the necessary pulse width fluctuation we found that the changes necessary are in the 10s of pico-second range, which is much better resolution than we have control over. The third option is to vary the voltage applied to the pulsing circuit with a summing junction. We have successfully implemented this scheme as a substitute for varying B_z directly.

8.3.1 Single Species Excitation

Figure 8.4 shows preliminary data for simultaneous resonance scans of the two isotopes using the procedure: $\gamma_{129}B = 3f + f_0$ and $\gamma_{131}B = f - f0$ where f is the pump modulation frequency and f_0 is the 2π pulse modulation rate. The depth of the 2π pulse modulation rate is scanned to optimize the amplitudes. The relative amplitudes of these signals are not fully understood, but other preliminary studies promise the successful use of this procedure in the near future.

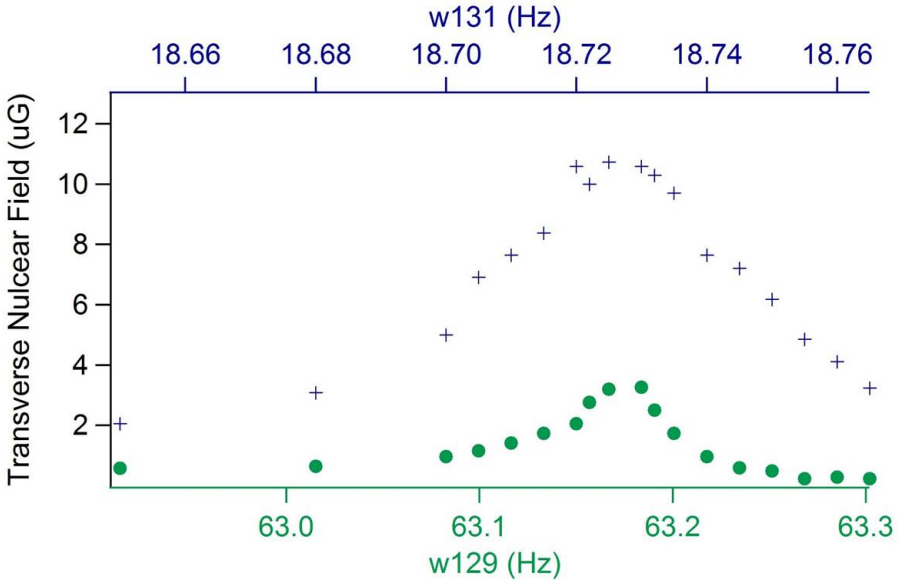

Figure 8.4: Preliminary scans of the two Xe isotopes using 2π pulse modulation as explained above show successful excitation, but smaller amplitude.

Chapter 9

Conclusions and Future Directions

I have shown in this thesis the successful implementation of transverse optical pumping and synchronous spin exchange optical pumping. I proposed that the new method would eliminate the alkali field shift systematic error from measurements of the NMR frequency and I have demonstrated at least a factor of $\times 2500$ suppression of that shift. The results of noise characterization measurements predict a frequency sensitivity of less than 10nHz/$\sqrt{\text{Hz}}$ forphoton shot noise limited dual species operation, which is better by an order of magnitude than other comagnetometer approaches to NMR. It is true that we have work to do in order to reach this number, but it is clear that the method of synchronous spin exchange optical pumping is a viable method for precision measurements with NMR.

9.1 Earth's Rotation Rate Measurement

Once the system is fully operational as a dual species oscillator, the plan is to take a measurement of the Earth's rotation. This should be a fairly simple proof of principle experiment since the rate at which the earth rotates is 6μHz, a factor of 100 above the current noise floor. For the purposes of this mesurement, we have a large $4' \times 4'$ lazy-susan, which will enable us to rotate the apparatus to align it with the earth's axis of rotation.

9.2 Axion

As described in Sec. 1.2 and Ref [Bulatowicz et al., 2013] work has already been done with NMR in the search for axion-like interactions. With the new system that has been described in

this thesis, we should be able to put a more stringent limit on the scalar-pseudo scalar coupling since the bias stability is reduced due to the alkali field shift suppression. This will be done in collaboration with Mike Snow at Indiana University who, along with his students, is currently designing a rotating mass apparatus for use with our setup.

9.3 Gyro with Northrop-Grumman

Our work has been done with some collaboration with the engineers and scientists at Northrop-Grumman Corporation. They have an interest in our work because of the potential for excellent gyroscope performance. We will therefore at some point be collaborating more closely to help them operate/build a gyroscope that implements the technology we have developed.

DISCARD THIS PAGE

Appendix A: Spin Exchange Relaxation Model

The purpose of this model is to explain the angular momentum loss due to a spin exchange collision that occurs in the middle of a 2π pulse. The two hyperfine levels $F = 1$ and $F = 2$ have equal and opposite magnetic moments, so that during a 2π pulse, atoms in one level will precess in the opposite direction as the other. If a spin exchange collision occurs after a rotation θ and the hyperfine level changes, then the atom will subsequently precess in the opposite direction for the remainder of the 2π pulse and will attain a rotation error of 2θ. I will outline the basic idea of the calculation for the fractional angular momentum loss due to this process. This simple analysis results in a behavior that is fairly close to what a more complex analysis obtains.

We start with the spin temperature distribution where we know that in the spin temperature distribution $F = a + b$ and $S = \frac{a-b}{4}$ where

$$a = \frac{4+q}{2q} \tag{A.1}$$

and

$$b = F - a \tag{A.2}$$

are the populations in $F = 2$ and $F = 1$ respectively. The slowing down factor, q is defined as

$$q = 1 + (2I+1) * \coth\left[\frac{\beta}{2}\right] \coth\left[\beta\Big(I + \frac{1}{2}\Big)\right] - \coth\left[\frac{\beta}{2}\right] \tag{A.3}$$

with

$$\beta = 2 \arctan P \tag{A.4}$$

We can then relate F and S:

$$F = qS = qP/2 \tag{A.5}$$

where P is the electron polarization. As the atom rotates during a 2π pulse, it is necessary to recalculate each parameter at the new angle.

We start with an initial polarization steady state P_0 along $\hat{x}$ before the 2π pulse. We use it to calculate the intial values q_0, F_0, and $a_0 = \frac{4+q_0}{2q_0}F_0$ and $b_0 = F_0 - a_0$. The atoms then rotate by θ

resulting in a new distribution given by:

$$F_\theta = a_0 e^{-i\theta} + b_0 e^{i\theta} \tag{A.6}$$

From this new value F_θ, we calculate P_θ, q_θ, a_θ, and b_θ. At this point, the atoms undergo a spin exchange collision and change hyperfine levels, so that they complete the 2π rotation of $2\pi - \theta$ radians precessing in the opposite direction. This results in the final distribution:

$$F_{2\pi} = a_\theta e^{i\theta} + b_\theta e^{-i\theta} \tag{A.7}$$

The cumulative effect relates the final state to the initial state:

$$F_{2\pi} = F_\theta\Big(\frac{q_\theta + 4}{2q_\theta}e^{-i\theta} + \frac{q_\theta - 4}{2q_\theta}e^{i\theta}\Big) \tag{A.8}$$

$$F_\theta = F_0\Big(\frac{q_0 + 4}{2q_0}e^{i\theta} + \frac{q_0 - 4}{2q_0}e^{-i\theta}\Big) \tag{A.9}$$

$$\rightarrow F_{2\pi} = F_0\Big(\frac{q_0 + 4}{2q_0}e^{i\theta} + \frac{q_0 - 4}{2q_0}e^{-i\theta}\Big)\Big(\frac{q_\theta + 4}{2q_\theta}e^{-i\theta} + \frac{q_\theta - 4}{2q_\theta}e^{i\theta}\Big) \tag{A.10}$$

$$F_{2\pi} = F_0\frac{32 + 2q_0q_\theta}{4q_0q_\theta} \tag{A.11}$$

The fraction of angular momentum that is lost is then

$$\frac{\Delta F}{F} = \frac{F_{2\pi} - F_0}{F_0} \tag{A.12}$$

$$\frac{\Delta F}{F} = \frac{1}{2} - \frac{8}{q_0q_\theta} \tag{A.13}$$

The result is seen in Fig A.1a where the fraction of angular momentum lost is plotted against initial polarization. The more complex model that involves the full treatment of the density matrix evolution gives the result in Fig A.1b.

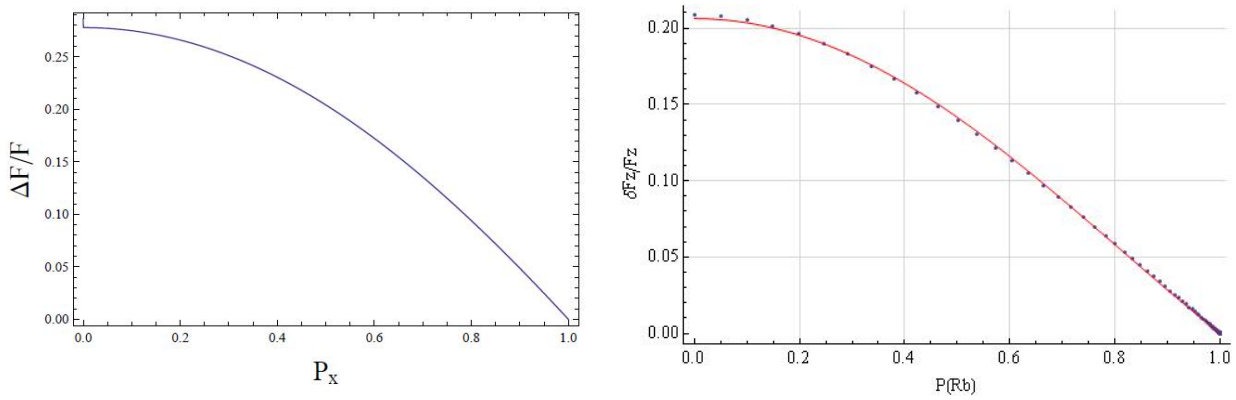

(a) Simple model result

(b) Full model result

Figure A.1: The modeling of the fractional angular momentum loss $\alpha(P_x)$ results in (a) for the simple model and (b) for the more complex model

Appendix B: Feedback

In this appendix I will outline the strange features of the NMR line shapes that are observed upon implementing feedback along the bias field direction. The analysis and use of this method are not fully developed.

While feedback is useful to lower the magnetic noise levels to the probe noise limit on B_z, it is not useful along B_y since the Xe signal of interest is a magnetic field along B_y. Whatever, the signal to noise ratio of that channel is, we are stuck with it. This is a tricky situation since due to the SSEOP, there are transients at the Xe frequency that show up as large components in the FFT. We have come up with a potential solution to this problem that will be presented in the chapter on dual species.

Feedback along $\hat{z}$ is a different matter, however, and we have successfully implemented it in the PPR magnetometer so that the magnetic noise drops to the probe noise level. When using parametric modulation, this probe noise is at the photon shot noise limit. When using this feedback in the context of the NMR, however, we observe interesting line narrowing effects on the linewidth and the slope of the quadrature component. A schematic of the setup with feedback in place is shown in FigB.1

Looking at the equation for the quadrature component of the Xe signal:

$$\widetilde{K_y} = \frac{K_{\max}}{1 + \Delta^2/\Gamma_{\text{eff}}^2} \frac{\Delta\Gamma_2}{\Gamma_{\text{eff}^2}} \tag{B.1}$$

and the $\hat{z}$ component of the Xe polarization

$$K_z = \tan(\alpha)\widetilde{K_y} \tag{B.2}$$

We can then add feedback along $\hat{z}$ such that $S_y = b_{SK}K_z + \delta B_z + B_f \rightarrow 0$ which implies that $\Delta \rightarrow \Delta_0 - \gamma B_f$ and we get

$$\widetilde{K_y} = \frac{K_{\max}\Gamma_2}{\Gamma_{\text{eff}}^2}(\Delta_0 - \gamma b_{SK}\tan(\alpha)\widetilde{K_y} + \gamma\delta B_z) \tag{B.3}$$

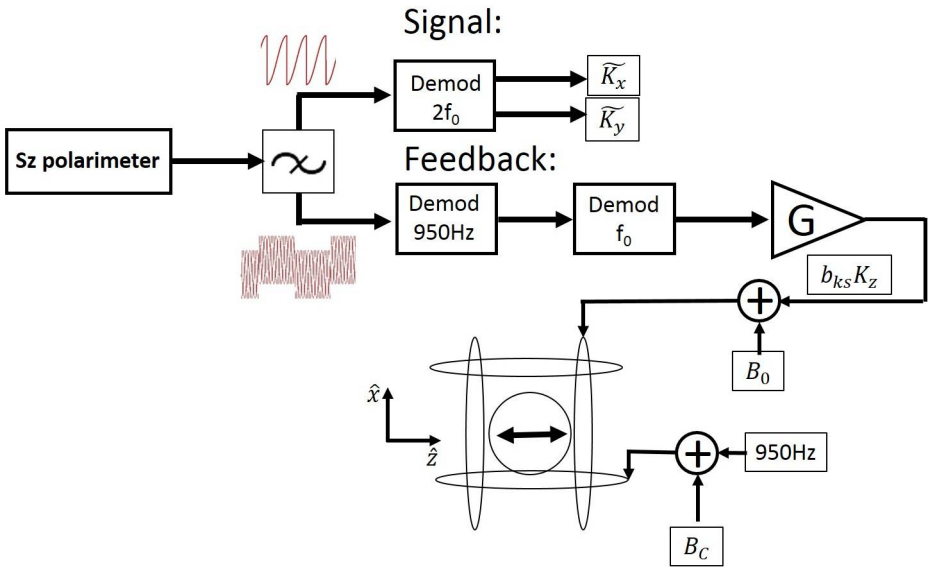

Figure B.1: A schematic showing the feedback network. The S_z polarimeter signal is filtered such that we can separate the Xe signal at $2f_0$ where f_0 is the pump modulation frequency and the 950Hz B_x modulation signal that measures B_z. The Xe signal is demodulated to give $\tilde{K_x}$ and $\tilde{K_y}$. The other signal is demodulated given some gain and then fedback to keep $B_z = 0$.

then

$$\widetilde{K_y} = \frac{\Delta_0 + \gamma\delta B_z}{\frac{\Gamma_{\text{eff}}^2}{K_{\max}\Gamma_2} + \gamma b_{SK}\tan(\alpha)} \tag{B.4}$$

From this we can define the slope of the quadrature to be

$$A = \frac{1}{\frac{\Gamma_{\text{eff}}^2}{K_{\max}\Gamma_2} + \gamma b_{SK}\tan(\alpha)} \tag{B.5}$$

which approaches infinity as the compensation field is adjusted so that $\tan(\alpha) \rightarrow -\frac{\Gamma_{\text{eff}}^2}{K_{\max}\Gamma_2}\frac{1}{\gamma b_{SK}}$. Without feedback, the slope of the quadrature component is limited to $K_{\max}/\Gamma_2$. The noise of the resonance frequency is then $\delta\Delta_0 = \frac{\delta\widetilde{K_y}}{A} - \gamma\delta B_z$. With $\delta B_y = b_{SK}\delta\widetilde{K_y}$

$$\delta\Delta_0 = \frac{\delta B_y}{b_{SK}A} + \gamma\delta B_z \tag{B.6}$$

We see that as A increases towards infinity, the $\hat{y}$ contribution to the noise is eliminated. The $\hat{z}$ contribution remains, but with dual species operation, we hope to eliminate its contribution as well. This would be a spectacular result if we can accomplish it. So far we have not been able to get low enough δB_z to see the suppression of the $\hat{y}$ noise, but we plan to work on this in the near future.

What we have demonstrated is a successful narrowing of the Xe linewidth and demonstration of a greatly enhanced quadrature slope, which can be seen in Fig B.2. The quadrature slope is enhanced a factor of $\times 500$ above the uncompensated slope and a factor of $\times 14$ above the compensated, no feedback case.

The narrowing of the linewidth by application of feedback along $\hat{z}$ has several interesting features. First of all, in the full solution to the Xe linewidth behavior as a function of $\tan(\alpha)$, there are three separate solutions regions for three $\tan(\alpha)$ regions:

$$\tan(\alpha) = -\frac{\Gamma_{\text{eff}}^2}{K_{\max}\Gamma_2}\frac{1}{\gamma b_{SK}} \tag{B.7}$$

$$\tan(\alpha) < -\frac{\Gamma_{\text{eff}}^2}{K_{\max}\Gamma_2}\frac{1}{\gamma b_{SK}} \tag{B.8}$$

$$\tan(\alpha) > -\frac{\Gamma_{\text{eff}}^2}{K_{\max}\Gamma_2}\frac{1}{\gamma b_{SK}} \tag{B.9}$$

Equation B.7 is the point of infinite slope while Eqns B.8 and B.9 describe the regions where there is hysteresis and broadening for ^{131}Xe. The full solution for the behavior of K_x and K_y where

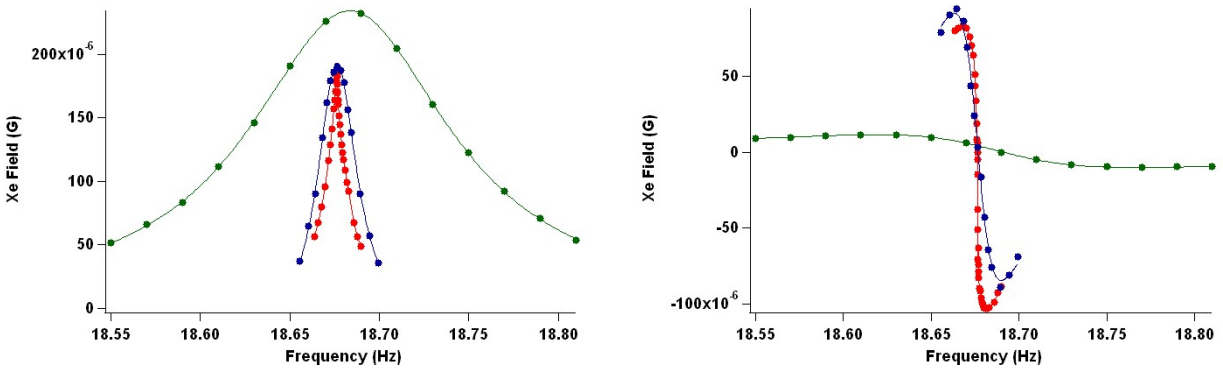

(a) In phase signals

(b) Quadrature signals

Figure B.2: These figures depict the in phase (a) and the quadrature signal (b) for uncompensated (green), compensated (blue), and compensated with B_z feedback (red). The improvement in slope from the compensated to the compensated with feedback is $\times 14$ and the overall improvement from the uncompensated to the compensated with feedback is $\times 500$. If you look closely, there is still small, < 0.1mHz, bit of hysteresis.

$\Delta \neq 0$ is very complicated and results in three solutions for each of the $\tan(\alpha)$ regions, which leads to hysteretic behavior that is seen in Figs B.3a and B.3b. These figures show the theory overlaid on the data since the fitting equation is quite complex. In a different $\tan(\alpha)$ region, there is broadening instead of hysteresis: Figs B.3c and B.3d. Finally, by tuning the compensation field very finely, we obtain the third $\tan(\alpha)$ "region" with near infinite slope: Fig B.4. The hysteresis is still present, but it is < 0.1mHz. An interesting question to ask in the process of adding feedback and tuning the compensation field to obtain very narrow widths is whether or not the characteristic relaxation rate is also changing. This relaxation rate typically defines the width of the Xe resonance. By doing a field growth measurement, we can extract what the characteristic rate actually is with and without feedback; it does not change.

The shape of the curves in the three regions changes with isotope since the gyromagnetic ratio changes sign. For ^{129}Xe we obtain the curves in FigB.5 which also mimic the theory rather well.

Another feature of the feedback is the sensitivity of the NMR resonance frequency on the phase of the compensation field. If the phase is adjusted slightly, then the resoanance frequency jumps significantly, as is seen in Fig B.6.

In addition to the question as to whether or not this feedback narrowing result will be useful, there is also the question as to whether or not this feature of feedback is unique to our system of synchronously pumped noble gas, which it isn't; it is a feature of any system where the feedback is operated near a point of instability, i.e. where the denomenator goes to zero. The hysteretic behavior can also be demonstrated by appropriate application of feedback to K_y. The procedure for this feedback is slightly different. Using the K_y signal, feedback to B_z with only proportional gain; to get the full spectrum (broadening, narrowing, hysteresis), the phase of the K_y lock-in must be adjusted by 180°. With this procedure, we see the same behavior. Strangely though, the ^{131}Xe signal looks like the ^{129} signal with our other form of feedback. Since this was simply a proof of principle experiment, we did not explore this effect further.

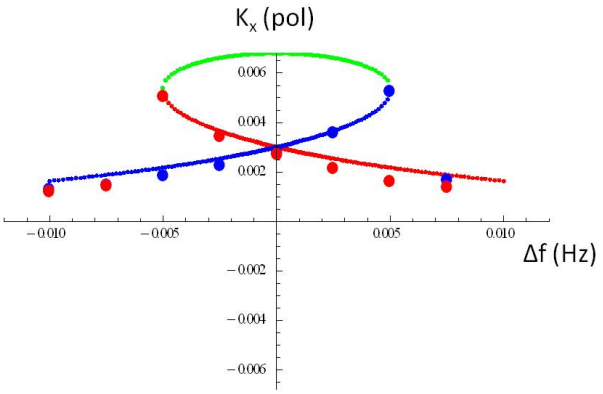

(a) In phase hysteresis

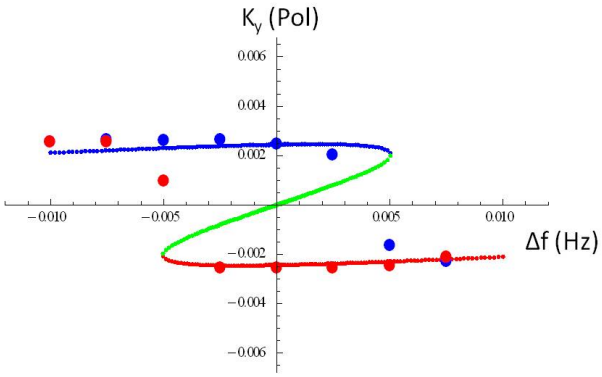

(b) Quadrature hysteresis

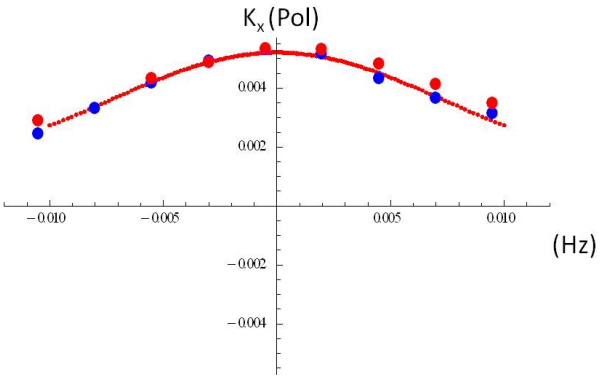

(c) In phase broadening

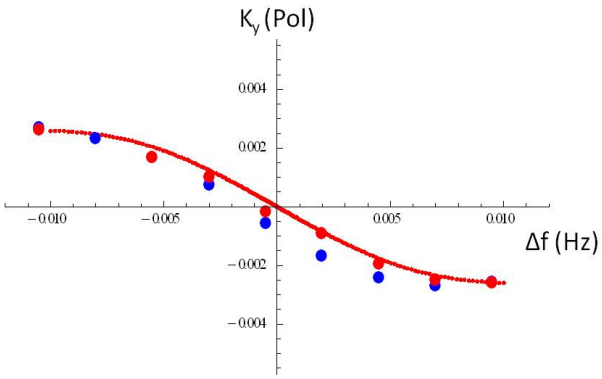

(d) Quadrature broadening

Figure B.3: The different characteristic curves for ^{131}Xe for different $\tan(\alpha)$ values. The fits are not fits to the data, bu the theoretical model overlaid on the data with adjusted parameters.

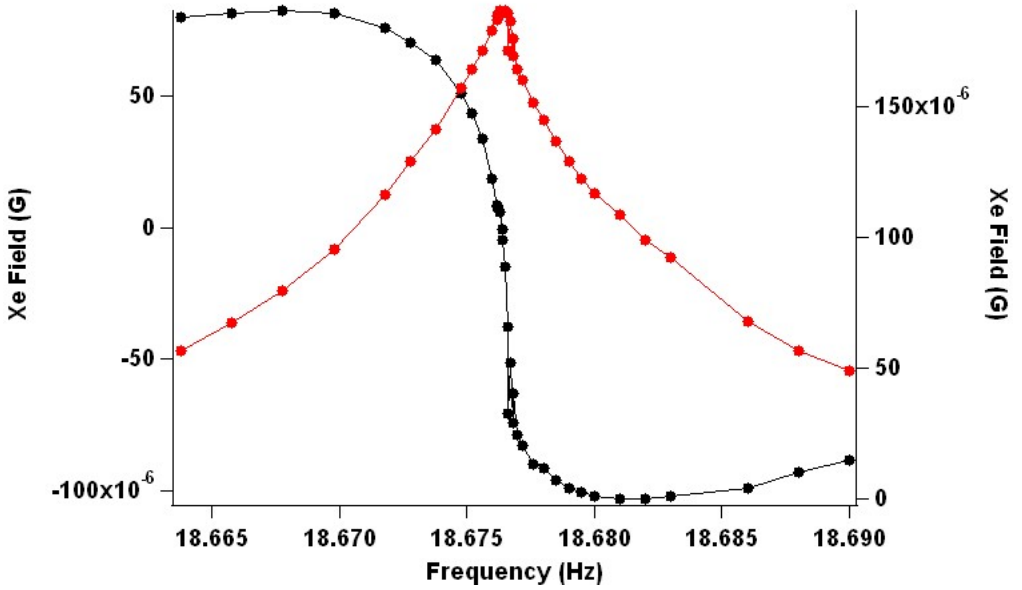

Figure B.4: The fully compensated with feedback data. There is still a < 0.1mHz amount of hysteresis.

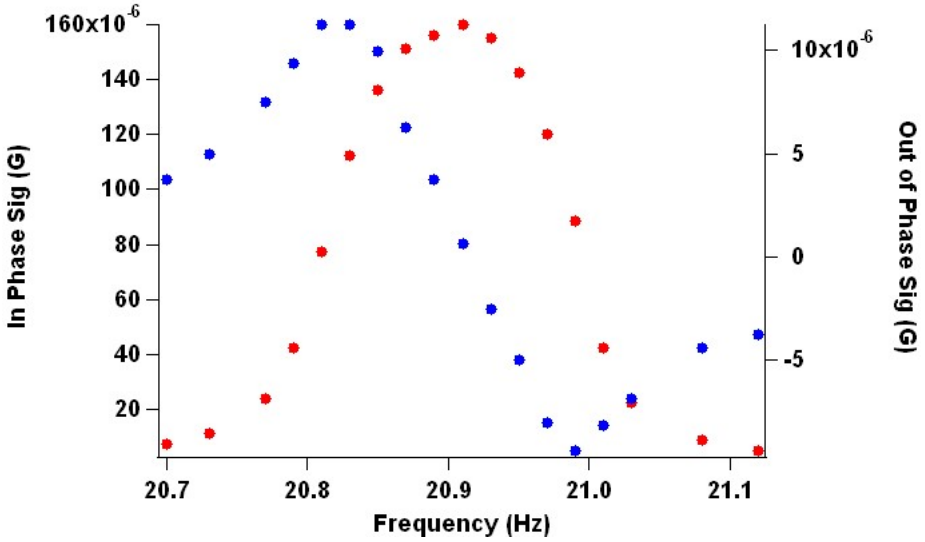

Figure B.5: The characteristic curve for ^{129}Xe. Where ^{131}Xe gives hysteresis, ^{129}Xe gives a ”mushroom” shape.

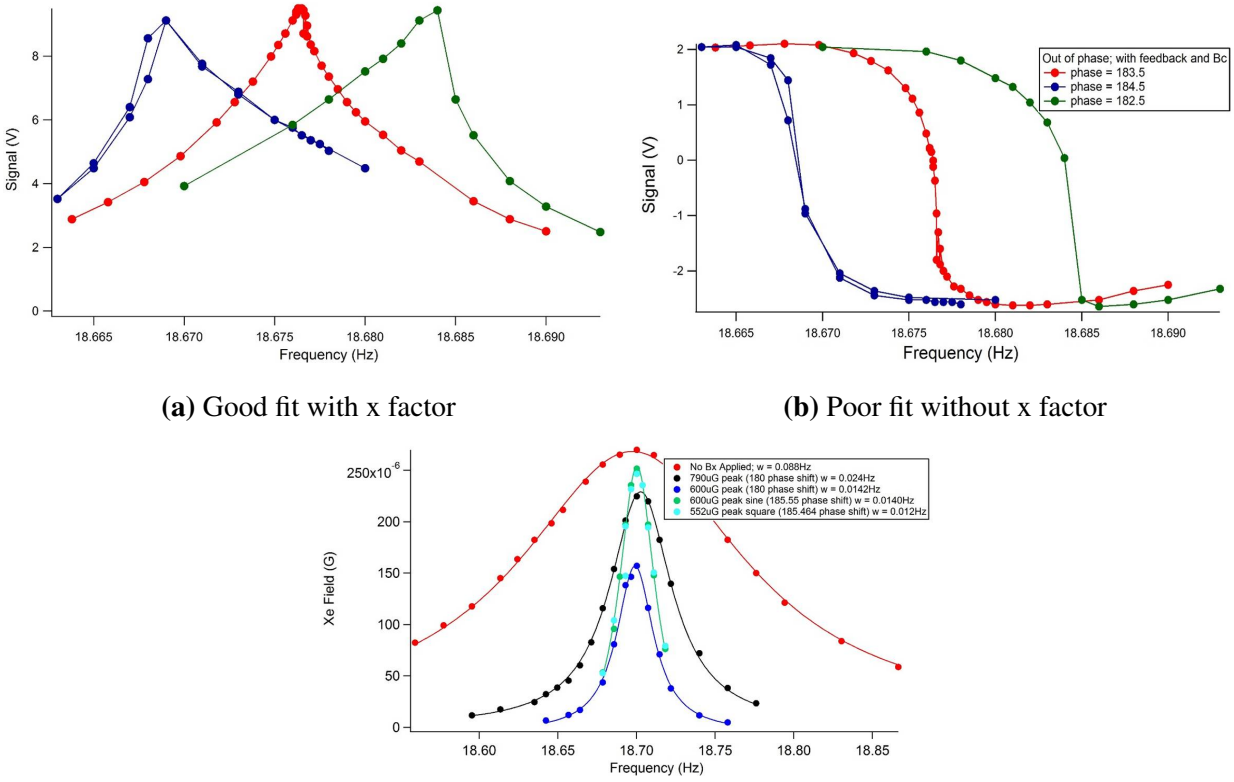

(a) Good fit with x factor

(b) Poor fit without x factor

(c) Poor fit without x factor

Figure B.6: This series of figures shows the compensation phase dependence of the in phase and quadrature (a) and (b) components with and without feedback (c). With feedback there is a strong phase dependence to the shape of the curves and the resonance frequency appears to shift. Without feedback, there is no observable frequency shift; the only adverse affect of an incorrect phase is a reduction in amplitude.

B.1 Noise Measurements with Xe and Feedback

In order to determine the merit of feedback, we close the loop and measure $\delta\widetilde{K_y}$ to see if the noise is suppressed by tuning the feedback to its optimal position. Taking noise measurements with the Xe signal takes a long time since its bandwidth is so small and we are truly interested in the very low frequency noise. For this, we developed a program that chirps the pump modulation at very low frequency. The function itself is: $\mathrm{chirp} = \sin\left(2\pi\exp[t/T_2] - t/T_2\right)$. We monitor the quadrature signal as the Xe moves through resonance then take the FFT of the signal as the chirp is applied and divide by the FFT of the chirp itself to obtain the Xe response. We then proceed with the noise measurement in the usual manner.

We want to do this measurement with feedback to see if there is a dependence of the noise on the compensation field as $\tan\left(\alpha\right)$ is scanned. We ran into issues with this measurement due the time it takes to get good resolution at the low frequencies where the slope enhancement is a maximum. Figure B.7 shows the response change as feedback is turned on and optimized. The actual noise measurements may have shown a suppression in noise, but were inconclusive. This warrants a much more detailed study.

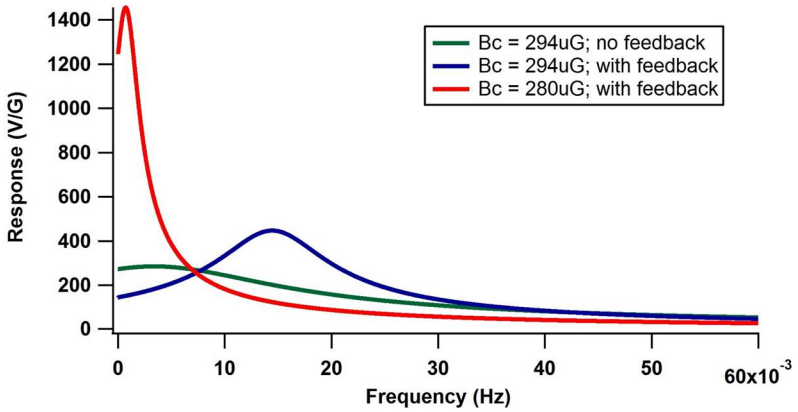

Figure B.7: The change in response when feedback is added. The green trace is the response without feedback, then when feedback is added and the $\hat{x}$ compensation field is not changed, the response increases, but is not centered on zero. Adjusting the compensation field dramatically increases the response and moves the center closer to zero. The response increases a factor of 7.

Appendix C: Igor Fourier Transform

When a Fourier transform is done in Igor, it must be scaled in order to result in a power spectrum. We start by deriving the power spectral density of a continuous noisy signal $n(t)$. The standard deviation is

$$\sigma^2 = \frac{1}{T}\int_{-T/2}^{T/2} n(t)^2 dt \tag{C.1}$$

If we then Fourier transform $n(t)$ we get

$$\sigma^2 = \frac{1}{T}\int_{-T/2}^{T/2} dt \int df \tilde{n}(f) e^{-2\pi i f t} \int df_1 \tilde{n}(f_1) e^{-2\pi i f_1 t} \tag{C.2}$$

$$= \int df \tilde{n}(f) \int df_1 \tilde{n}(f_1) \mathrm{sinc}[\pi T(f_1 - f)] \tag{C.3}$$

which reduces to

$$\sigma^2 = \int_{-\infty}^{\infty} df \frac{|\tilde{n}(f)|^2}{T} \tag{C.4}$$

if we assume $f_1 = f$ where the sinc function is peaked. We can then define the power sprectral density as

$$\sigma^2 = \frac{1}{2}\int_0^{\infty} df P_n(f) \tag{C.5}$$

$$P_n(f) = \frac{2|\tilde{n}(f)|^2}{T} \tag{C.6}$$

and the power spectrum is the squareroot of $P_n(f)$.

Moving to the Igor FFT, which is discrete. The data that is Fourier transformed in Igor is a set of data $n(t_p)$ with N points separated in time by δt so that $T = N\delta t$. The function $\tilde{n}(f_q)$ can be written as:

$$\tilde{n}(f_q) = \delta t \sum_{-N/2}^{N/2} n(t_i) e^{2\pi i (q t_p/T)} \tag{C.7}$$

where

$$\mathcal{N}_q = \sum_{-N/2}^{N/2} n(t_i) e^{2\pi i (q t_p/T)} \tag{C.8}$$

is the typical discrete Fourier transform that Igor gives. We can then relate this to $\tilde{n}(f_q)$

$$\tilde{n}(f_q) = \frac{T}{N}\mathcal{N}_q \tag{C.9}$$

Now using the definition for the power spectral density from above

$$P_n(f) = \frac{2|\tilde{n}(f_q)|^2}{T} = \frac{2T}{N^2}|\mathcal{N}_q|^2 \tag{C.10}$$

and the resulting power spectrum is

$$\delta n(f) = \sqrt{P_n(f)} = \frac{\sqrt{2T}}{N}|\mathcal{N}_q| \tag{C.11}$$

This means that the magnitude FFT that Igor gives must be scaled by $\frac{\sqrt{2T}}{N}$.

Appendix D: Circuit Components

D.1 Circuit 1

Components in the Circuit Diagram:

- M1: IRF840
- D1: 1N5369B (50V zener)
- D2: 1N4448 (fast rectifier)
- R1 $= 195\Omega$
- L1 $= 29\mu$H
- C1 $= 33\mu$F

Components not in circuit diagram:

- MOSFET driver: MIC4420
- Buffer before and after MOSFET driver: BUF634

All ICs are wired with their suggested filter capacitors.

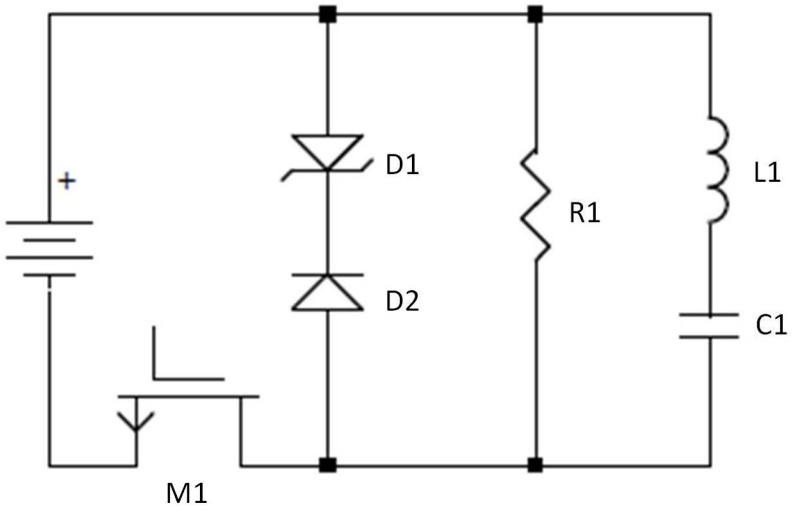
+
D1
D2
R1
L1
C1
M1

D.2 Circuit 2

Components in the Circuit Diagram:

- M1: F9530N
- M2: IRF840
- M3: IRF840
- D1: 1N5347B (10V zener)
- D2: 1N4448 (fast rectifier)
- C1 $= 100$nF (for a 2 μs pulse)
- R1 $= 1000\Omega$
- R2 $= 1000\Omega$
- R3 $= 10\Omega$
- R4 $= 200\Omega$
- L1 $= 29\mu$H

Components not in circuit diagram:

- MOSFET driver for n-type: MIC4420

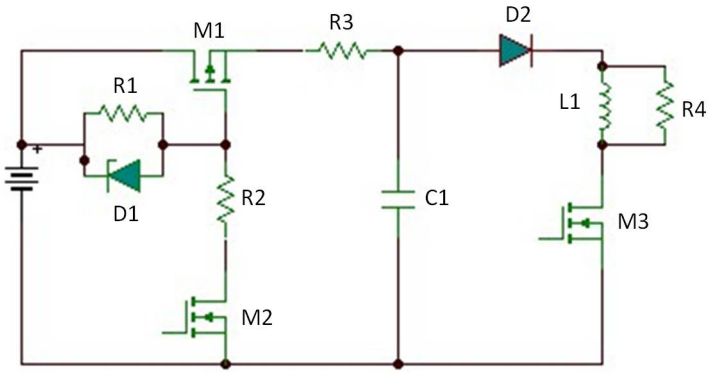

D.3 High Voltage Circuit

Because this circuit is no longer in use and we have no plans to use it in the future, there is not a complete list of parts. The one important part being the high power op-amp which is PA107DP from APEX.

Bibliography

Abragam, A. (1990). *Principles of magnetic resonance*. New York: Springer-Verlag.

Allmendinger, F., Heil, W., Karpuk, S., Kilian, W., Scharth, A., Schmidt, U., ... Tullney, K. (2014). *Phys. Rev. Lett. 112*, 110801. doi:10.1103/PhysRevLett.112.110801

Allred, J., Lyman, R., Kornack, T., & Romalis, M. (2002). *Phys. Rev. Lett. 89*, 130801. doi:10.1103/PhysRevLett.89.130801

Anderson, L., Pipkin, F., & Baird, J. (1960). *Physical Review*, *1200(4)*, 1279.

Babcock, E., Chann, B., Walker, T., Chen, W., & Gentile, T. (2006). *Phys. Rev. Lett. 96*, 083003. doi:10.1103/PhysRevLett.96.083003

Bhaskar, N. D., Happer, W., & McClelland, T. (1982). *Phys. Rev. Lett*, *49*, 25. doi:10.1103/PhysRevLett.49.25

Bhaskar, N. D., Happer, W., Larsson, M., & Zeng, X. (1983). *Phys. Rev. Lett*, *50*, 105. doi:10.1103/PhysRevLett.50.105

Brinkmann, D. (1963). *Helv. Phys. Acta*, *36*, 413.

Budker, D., & Kimball, D. (2013). *Optical magnetometry*. New York: Cambridge University Press.

Bulatowicz, M., Griffith, R., Larsen, M., Mirijanian, J., Fu, C., Smit, E., ... Walker, T. (2013). *Phys. Rev. Lett. 111*, 102001. doi:10.1103/PhysRevLett.111.102001

Chow, W., Gea-Banachioche, J., Pedrottie, V., L.M. andSanders, Schleich, W., & Scully, M. (1984). *Rev. Mod. Phys. 57*, 61–104. doi:10.1103/RevModPhys.57.61

Chu, P.-H., Dennis, A., Fu, C. B., Gao, H., Khatiwada, R., Laskaris, G., ... Zheng, W. (2013). *Phys. Rev. D*, *87*, 011105. doi:10.1103/PhysRevD.87.011105

Cohen-Tannoudji, C. (1963). *J. Phys. 24*, 653.

Durfee, D., Shaham, Y., & Kasevich, M. (2006). *Phys. Rev. Lett. 97*, 240801. doi:10.1103/PhysRevLett.97.240801

Glenday, A., Cramer, C., Phillips, D., & Walsworth, R. (2008). *Phys. Rev. Lett. 101*, 261801. doi:10.1103/PhysRevLett.101.261801

Groves, P. (2008). *Inertial and multisensor integrated navigation systems*. Norewood, MA: Artech House.

Happer, W. (1972). *Rev. Mod. Phys. 44*, 169. doi:10.1103/RevModPhys.44.169

Happer, W., & Tam, A. (1977). *Phys. Rev. A*, *16*, 1877. doi:10.1103/PhysRevA.16.1877

Happer, W., Jau, Y., & Walker, T. (2009). *Optically pumped atoms*. New York: Wiley.

Jau, Y., Kuzma, N., & Happer, W. (2002). *Phys. Rev. A*, *66*, 052710. doi:10.1103/PhysRevA.66.052710

Jimenes-Martinez, R., Kennedy, D., Rosenbluh, M., Donley, E., Knappe, S., Seltzer, S., ... Kitching, J. (2014). *Nature Communications*, *5*, 3908. doi:10.1038/ncomms4908

Kasevich, M., Riis, E., Chu, S., & Devoe, R. (1989). *Phys. Rev. Lett. 63*, 612. doi:10.1103/PhysRevLett.63.612

Kirschvink, J. (1992). *Bioelectromagnetics*, *13*, 401.

Kitching, J., Knappe, S., & Donley, E. A. (2011). *IEEE Sensors Journal*, *11*, 1749.

Kornack, T., Ghosh, R., & Romalis, M. (2005). *Phys. Rev. Lett. 95*, 230801. doi:10.1103/PhysRevLett.95.230801

Korver, A., Wyllie, R., Lancor, B., & Walker, T. G. (2013). *Phys. Rev. Lett. 111*, 043002. doi:10.1103/PhysRevLett.111.043002

Korver, A., Wyllie, R., Lancor, B., & Walker, T. G. (2015). doi:http://arxiv.org/abs/1506.08797

Kwon, T., Mark, J., & Volk, C. (1981). *Phys. Rev. A*, *24*, 1894. doi:10.1103/PhysRevA.24.1894

Lancor, B., Babcock, E., Wyllie, R., & Walker, T. (2010). *Phys. Rev. A*, *82*, 043435. doi:10.1103/PhysRevA.82.043435

Ledbetter, M., Savukov, I., Aosta, V., Budker, D., & Romalis, M. (2008). *Phys. Rev. A*, *77*, 33408. doi:10.1103/PhysRevA.77.033408

Mhaskar, R., Knappe, S., & Kitching, J. (2012). *Applied Physics Letters*, *101*, 241105–1.

Nelson, I., & Walker, T. (2001). *Phys. Rev. A*, *65*, 012712. doi:10.1103/PhysRevA.65.012712

Petukhov, A., Pignol, G., Jullien, D., & Andersen, K. (2010). *Phys. Rev. Lett. 105*, 170401. doi:10.1103/PhysRevLett.105.170401

Romalis, M., Miron, E., & Cates, G. (1997). *Phys. Rev. A*, *56*, 4569. doi:10.1103/PhysRevA.56.4569

Rosenberry, M., & Chupp, T. (2001). *Phys. Rev. Lett. 86*, 22–25. doi:10.1103/PhysRevLett.86.22

Smiciklas, M., Brown, J., Cheuk, L., Smullin, S., & Romalis, M. (2011). *Phys. Rev. Lett. 107*, 171604. doi:10.1103/PhysRevLett.107.171604

Smullin, S., Savukov, I., Vasilakis, G., Ghosh, R., & Romalis, M. (2009). *Phys. Rev. A*, *80*, 033420. doi:10.1103/PhysRevA.80.033420

Tullney, K., Allmendinger, F., Burghoff, M., Heil, W., Karpuk, S., Kilian, W., ... Trahms, L. (2013). *Phys. Rev. Lett. 111*, 100801. doi:10.1103/PhysRevLett.111.100801

Vold, T., Raab, F., Heckel, B., & Fortson, E. (1984). *Phys. Rev. Lett. 52*, 2229–2232. doi:10.1103/PhysRevLett.52.2229

Walker, T., & Happer, W. (1997). *Rev. Mod. Phys. 69*, 629. doi:10.1103/RevModPhys.69.629

Youdin, A., Krause, D., Jagannathan, K., Hunter, L., & Lamoreaux, S. (1996). *Phys. Rev. Lett. 77*, 2170. doi:10.1103/PhysRevLett.77.2170